Universidad de Concepción

Facultad de Ciencias Físicas y Matemáticas

ETHER-FP: EXPLORING THE FUNDAMENTAL PLANE OF BLACK HOLE ACTIVITY AND RADIO EMISSION MECHANISMS IN ACTIVE GALACTIC NUCLEI

ETHER-FP: EXPLORANDO EL PLANO FUNDAMENTAL DE LA ACTIVIDAD DE AGUJEROS NEGROS Y LOS MECANISMOS DE EMISIÓN DE RADIO EN NÚCLEOS GALÁCTICOS ACTIVOS

Por: Vicente Alfonso Arratia Carrasco

Profesor Guía: Neil Mark Nagar

Tesis presentada a la Facultad de Ciencias Físicas y Matemáticas de la Universidad de Concepción para optar al grado académico de Magíster en Astronomía

Junio 2024

Concepción, Chile

Dedicado a los que me impulsaron a seguir adelante.

AGRADECIMIENTOS

Surreal. Ése sería el concepto que define este momento. Después de 3 años y medio, escribir estas palabras es algo que muchas veces pensé jamás concretaría. Aún me cuesta creer que este proceso esté llegando a su fin, y verlo convertido en una realidad me hace estar completamente agradecido por todas las personas que me impulsaron a seguir adelante éste último tiempo, pues sin ellas no hubiese sido posible.

Gracias a mi profesor guía Neil, por aguantarme todo éste tiempo, sus consejos, conocimiento y apoyo. A la profesora Amy, por siempre preocuparse por cómo estaba y aconsejarme cuando me veía las veces que iba a la Universidad. Y a todos quienes directamente colaboraron de una u otra forma en esta tesis.

Gracias a mis amigos: Mato, por ser siempre de finales, y regalarme una amistad que ha sabido afrontar el paso del tiempo. Daniel, por acompañarme en ésta lucha de la tesis y en muchas aventuras a lo largo de nuestras vidas. Sánchez y Javier, por todos los buenos momentos juntos y considerarme siempre. A los chicos del Ritorno, con los que siempre estaré agradecido por su enorme cariño y recibimiento. A la Paula, por su compañía y confianza. A Fernando, por ayudarme a atravesar el túnel. Y a mis compañeros de carrera, con quienes compartí mi vida Universitaria, que ya llega a su fin.

Gracias a mi familia: A mi hermano, por siempre apoyarme con lo que necesitara, y ser alguien con quien compartir las cosas que me gustan. A mi gata la Canela, por alegrarme todos los días con su presencia. Y a mis padres, por permitirme estar con ellos a pesar de las dificultades, sé y agradezco lo mucho que se esfuerzan día a día.

Muchas gracias a mi Amorcito <3: Bárbara, llegaste a mi vida de la forma más inesperada, y sin darme cuenta te convertiste en aquello que más necesitaba. Te agradezco inmensamente por todo el amor, confianza y cariño que me has dado, por siempre acompañarme, estar ahí cuando más lo necesitaba, motivarme a seguir adelante, alegrarte cuando veías que avanzaba, y enseñarme que puedo ser mejor. Es en gran parte gracias a ti que ahora puedo escribir esto, has sido el apoyo mas importante para mí en éste proceso y me encantaría que así también fuera en el camino de la vida. Te amo con todo mi corazón, nunca lo dudes.

Por último, por todo lo que afronté, me gustaría agradecerme a mí también: Vicente, gracias por haber seguido adelante a pesar de las adversidades, y por siempre intentar ser mejor, sigue así. Lo lograste.

Resumen

Las recientes mejoras en la resolución y sensibilidad de la interferometría de línea de base muy larga (VLBI) milimétrica (mm) han permitido obtener imágenes de las regiones internas de los agujeros negros supermasivos (SMBH), marcando una nueva era en la investigación teórica y observacional de los núcleos galácticos activos (AGN). Debido a esto se consolidó la muestra Event Horizon and Environs (ETHER), convirtiendose en el catálogo más grande de AGN. Si bien muchas fuentes de ETHER aún no se han explorado lo suficiente, las técnicas de ajuste de modelos de distribución de energía espectral (SED) y las relaciones empíricas pueden ayudar a proporcionar la información necesaria para limitar las perspectivas de observabilidad con el Event Horizon Telescope (EHT) y el Global mm-VLBI Array (GMVA). En este contexto, nuestro objetivo es mejorar ETHER incorporando nuevos datos de la literatura y aprovechar sus grandes estadísticas para revisar el Plano Fundamental (FP) de la actividad de los agujeros negros en múltiples frecuencias de radio y submuestras. Este esfuerzo busca profundizar nuestra comprensión de los mecanismos físicos que gobiernan la emisión de ondas de radio en diversos escenarios y guiar el uso de modelos de flujo de acreción dominado por advección (ADAF) o en combinación con chorros para predicciones de flujo en longitudes de onda de centímetros a sub-mm. Enriquecemos ETHER con datos de fotometría de rayos X duros y radio multifrecuencia obtenidos de los catálogos CSC, eRASS1, VLASS y FIRST, complementados con información adicional obtenida a través de consultas automatizadas a SDSS, SIMBAD y NED. Utilizando modelos de regresión lineal de mínimos cuadrados ordinarios y técnicas numéricas de minimización de la funcion mérito, calculamos coeficientes de correlación de mejor ajuste y derivamos nuevas correlaciones de radio/rayos X y FP en varias frecuencias de radio, tipos de AGN, desplazamientos al rojo, morfologías de galaxias, proporciones de Eddington y valores de sonoridad de radio. Adicionalmente, desarrollamos y empleamos un algoritmo de ajuste de SED que involucra modelos fenomenológicos de chorro y/o emisiones ADAF térmicas semianalíticas. Nuestro análisis nos permitió confirmar la existencia del FP en todas las frecuencias de radio probadas, validar aún más su uso como estimador de masa a distancias mayores, fomentar su uso por sobre la correlación de radio/rayos X debido a la dispersión reducida, entender por qué sesgos en la muestra conducen a diversos FP, y encontrar evidencia de evolución a través del corrimiento al rojo y la longitud de onda del mecanismo de emisión de radio dominante. Los ajuste de SED generalmente favorecieron el uso de modelos combinados de chorro y acreción en lugar de simulaciones solo con ADAF para estimaciones de flujo. En última instancia, los hallazgos y sistemas desarrollados en esta tesis han mejorado y mejorarán significativamente nuestra comprensión de la evolución de SMBH en todo el universo y definirán la muestra ETHER "Oro" para estudios con el EHT y GMVA.

Keywords – galaxies: active – black hole physics – X-rays: galaxies – radio continuum: galaxies

Abstract

Recent improvements in millimeter (mm) very-long-baseline interferometry (VLBI) resolution and sensitivity have enabled the imaging of the innermost regions of supermassive black holes (SMBH), marking a new era in theoretical and observational research of active galactic nuclei (AGN). Motivated by these advancements, the Event Horizon and Environs (ETHER) sample has been created, and has grown into the largest catalog of SMBH to date. While many ETHER sources remain insufficiently explored, spectral energy distribution (SED) model fitting techniques, and empirical relations, can help provide necessary information to constrain observability prospects with the Event Horizon Telescope (EHT) and the Global mm-VLBI Array (GMVA).

In this context, we aim to enhance ETHER by incorporating new data from the literature and databases, and leverage its large statistics to revisit the Fundamental Plane (FP) of black hole activity in multiple radio frequencies and subsamples. This effort seeks to deepen our understanding of the physical mechanisms governing radio-wave and hard X-ray emission from SMBH in various scenarios, and guide the usage of advection-dominated accretion flow (ADAF) or combined accretion-jet SED models for flux predictions at centimeter to sub-mm wavelengths.

We enrich ETHER with multi-frequency radio and hard X-ray photometry sourced from large catalogs (e.g., CSC, eRASS1, VLASS, and FIRST catalogues), supplemented with information obtained through automated queries to SDSS, SIMBAD, and NED. Using ordinary least squares linear regression models and numerical merit function minimization techniques, we calculate best-fit correlation coefficients and derive new radio/X-ray correlations and FPs across radio frequencies, AGN types, redshifts, galaxy morphologies, Eddington ratios, and radio-loudness values. Additionally, we develop and employ an SED fitting algorithm involving phenomenological jet and/or semianalytical thermal ADAF emission models.

Our analysis enabled us to confirm the existence of the FP across all radio frequencies tested, further validate its use as mass estimator at larger distances, encourage its use over the radio/X-ray correlation due to reduced scatter, understand why sample bias leads to diverse FPs, and find evidence of evolution across redshift and radio wavelength of the dominant radio emission mechanism. SED model fitting results generally favored the use of combined accretion-jet models over ADAF-only models for flux estimations. Ultimately, the findings and systems developed in this thesis have, and will, significantly improve our understanding of SMBH evolution across the universe, and define the “Gold” ETHER sample for EHT and GMVA studies.

Keywords – galaxies: active – black hole physics – X-rays: galaxies – radio continuum: galaxies

Contents

List of Tables

List of Figures

Chapter 1

Introduction

1.1 Active Galactic Nuclei

1.1.1 Black holes

Black holes (BHs) can be defined as spherical regions of spacetime within a maximum radius or "shadow" called the event horizon, where the escape velocity from a gravitational field is larger than the speed of light (Finkelstein, 1958; Celotti et al., 1999). Their masses range from a few to a few billion times the mass of the Sun. Originating from the gravitational collapse of massive stars or giant gas clouds, and potentially emerging as a result of mergers between massive gas-rich galaxies (Loeb and Rasio, 1994; Volonteri, 2010; Mayer and Bonoli, 2018), they manifest in galactic cores, binary systems with a companion star, and drive the mechanisms that power distant quasars (Mahadevan, 1997). The shadow size is dictated by the mass ($M_{\rm BH}$) of the BH, which together with spin and charge, constitute the only intrinsic properties of these objects. Since the former parameter can span several orders of magnitude, BHs are classified into three main categories: stellar mass BHs in the lower end ($M_{\rm BH}/M_{\odot} \leq 10^2$; Hughes, 2005), intermediate mass BHs (IMBHs) within the range of $10^2 < M_{\rm BH}/M_{\odot} < 10^6$ (Gültekin et al., 2022), and supermassive ones (SMBH; $M_{\rm BH}/M_{\odot} > 10^6$). Note, however, that the exact dividing lines depend on individual authors. Indigenous to galaxy cores, SMBHs can transition into an active state characterized by high luminosities driven by abundant accretion of surrounding material. These active galactic nuclei (AGN) output large amounts of energy across the whole electromagnetic spectrum via outflow and inflow processes (Narayan, 1996; Yuan and Narayan, 2014; Netzer, 2015; Almeida and Ricci, 2017; Hickox and Alexander, 2018).

The amount of infalling matter within a certain timescale is quantified in terms of the mass accretion rate

($\dot{M}$), typically measured in units of solar masses per year ($M_\odot$ yr^{-1}). To maintain its virial equilibrium (i.e., balance between radiative pressure and gravitational potential), the maximum luminosity at which an AGN can accrete material is known as the Eddington luminosity or limit ($L_{\rm Edd}$), a quantity directly dependent on the mass of the BH. This relationship is expressed as $L_{\rm Edd} = 1.3 \times 10^{38}\, M_{\rm BH}/M_\odot$ (Begelman, 1979; Watarai et al., 2000; Wang et al., 2006; Ho, 2008; Boccardi et al., 2021; Bariuan et al., 2022), and allows quantification of the accretion driven radiative output in terms of the fraction between the bolometric ($L_{\rm bol}$) and Eddington luminosities, known as the Eddington ratio ($l_{\rm Edd} = L_{\rm bol}/L_{\rm Edd}$; Nagar et al., 2005; Padovani et al., 2017; Hickox and Alexander, 2018; Ruffa et al., 2024).

1.1.2 Taxonomy

Variability of both the internal (e.g., mass, spin) and the "external" or environmental parameters (e.g., accretion rate and geometry) hides fundamental differences in AGN composition and their radiative/mechanical behaviour, that can profoundly shape the morphology of the core region and influence galaxy evolution (Davé et al., 2011; Page et al., 2012; Raouf et al., 2019). At the lower end, SMBHs accreting at extremely low rates relative to Eddington ($\log l_{\rm Edd} < -7$) are considered inactive and challenging to isolate from galactic emission (Rosas-Guevara et al., 2016). Locally (at redshifts $z < 0.05$), the observed population is abundantly within the $-7 \leq \log l_{\rm Edd} \leq -2$ range, exhibiting relatively weak but detectable luminosities of $\sim 10^{40}$ erg s^{-1}, often measured in the optical Hα line, the hard X-ray, or via compact radio cores. These are commonly referred to as low-luminosity AGN (LLAGN; Ho et al., 1997; Nagar et al., 2005; Maoz, 2007). At larger distances, the most powerful AGN ($L_{\rm H\alpha} >> 10^{40}$ erg s^{-1}) are fueled by accretion inflows near the Eddington limit ($\log l_{\rm Edd} \sim 0$), making them capable of matching, or even outshining, their host galaxy luminosity (Lusso et al., 2011).

Given this diversity, AGN have been extensively classified based mainly on emission line luminosities, profiles and ratios, their structure, and their orientation to the line of sight (LOS) given potential beaming effects (Netzer, 2015; Almeida and Ricci, 2017). At a general level, these objects are categorized in different types (Maiolino and Rieke, 1995; Ho, 2008; Gültekin et al., 2009; Netzer, 2015; Almeida and Ricci, 2017; Hickox and Alexander, 2018) grounded on the presence and strength of broad (Full-width at half-maximum FWHM > 2000 km s^{-1}) emission lines in their spectral energy distribution (SED), which probes nuclear obscuration:

- **Type I:** Bright at optical/X-ray. Dominated by broad emission lines associated to a zone within $0.01 - 1$ parsecs (pc) from the SMBH, that is composed of highly ionized, high velocity and dust-free dense gas clouds, known as the broad-line region (BLR). Essentially meaning an unobscured view of the nucleus.

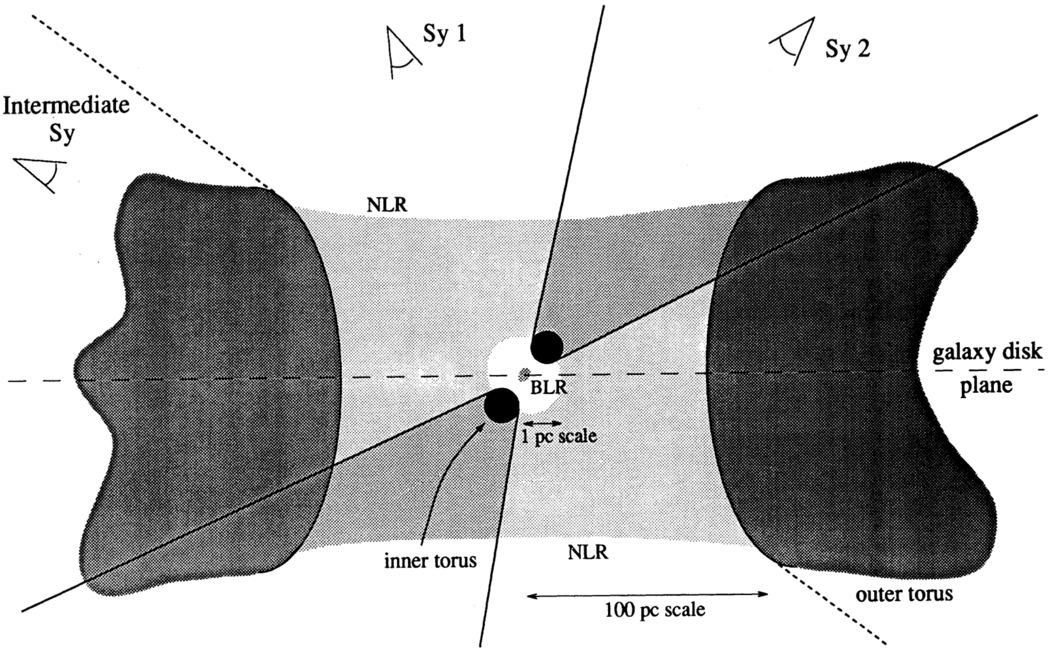

Figure 1.1.1: Schematic view of the cross section of a Seyfert type AGN nuclei. Figure from Maiolino and Rieke (1995).

- **Type II:** Bright at Infrared (IR). Dominated by ubiquitous low velocity width (FWHM $< 1\,000$ km s^{-1}) emission lines arising from an area extending from $\sim$ 10 pc to $\sim$ 1 kpc from the SMBH, composed of dense and ionized gas clouds, known as the narrow-line region (NLR). The BLR in these AGN are obscured to the line of sight by a sub-pc accretion disk, or dusty torus, spanning scales of 0.1 pc to 10 pc from the galactic center.
- **Type 1.X:** Ranging from 1 to 9, lower X values mean the contribution from broad emission lines is larger (unobscured), while higher values of X mean that narrow lines dominate (obscured).

At high redshifts ($z > 0.1$), radio-bright quasi-stellar objects (QSOs; Burbidge, 1967), commonly known as quasars, exhibit intense and variable nuclear radiation that eclipses the energy from the host galaxy. In contrast, Seyferts are nearby LLAGNs, characterized by a core similar to that of a QSO, but whose overall galactic luminosity can be distinguished separately from the nucleus. For a schematic view of the central structure of Seyferts, refer to Figure 1.1.1.

Another common type of AGN are Low Ionization Nuclear Emission-line Regions (LINERs; Heckman, 1980), which encompass nuclei presenting low luminosity and weakly ionized emission lines, the nature of which can be linked to AGN activity or nearby star formation regions (Terlevich and Melnick, 1985; Shields, 1992). In other cases, SMBHs emission is dominated by an outflow of material in the form of a highly luminous and variable beamed (i.e., Doppler boosted by alignment with the LOS) jet, that extends greatly from the galactic core (Urry and Padovani, 1995). These AGN receive the name of blazars. One specific class of blazar are called BL Lacertae (BL Lacs), highlighted by their high radio-loudness (ratio between radio and X-ray luminosity $R = L_{\mathrm{R}}/L_{\mathrm{X}}$; **?**Wilson and Colbert, 1994; Heinz and Sunyaev, 2003; Merloni et al., 2003; Panessa et al., 2007; Nemmen et al., 2014; Fischer et al., 2021; Bariuan et al., 2022) and brightness variability. Additional classifications of radio galaxies, those with kpc-scale jets, based on the relation between the dominant radio luminosity of the nucleus and that of its environment receive the name of Fanaroff-Riley (FR; Fanaroff and Riley, 1974), describing a jet luminosity decrease with increasing distance from the base up to the lobe (FR-I), and vice versa (FR-II). AGN taxonomy can branch further when considering different states and modes of accretion driven by the radiative efficiency of the system, such as the low/hard (L/H) and high/soft (H/S) states. The former is identified by a geometrically thick and optically thin flow of material being accreted at low rates, whereas the latter is characterized by a geometrically thin and optically thick inflow that accretes closer to the Eddington limit. In the H/S state, jets become less prominent compared to the L/H counterpart (Yuan et al., 2005; Körding et al., 2006; Blandford et al., 2019).

1.2 Spectral energy distribution of AGN

1.2.1 Radiative processes

Recently, the existence of two SMBHs was empirically proven through 230 GHz imaging of the accretion inflow of M87* in the giant elliptical galaxy M87, and Sagittarius A*(SgrA*) in the center of the Milky Way. Ring-like structures and shadows were resolved in both cases thanks to unprecedented resolutions ($\sim 20\,\mu$as) achievable with Very Long Baseline Interferometry (VLBI), a technique used with the Event Horizon Telescope (EHT) that marked the beginning of a new era in BH research and imaging (Event Horizon Telescope Collaboration et al., 2019; Collaboration et al., 2019; Event Horizon Telescope Collaboration et al., 2022).

Although SMBHs do not emit light themselves, they were still able to be "observed" thanks to distinct thermal and non-thermal radiative processes (Rybicki and Lightman, 1991; Kawamuro et al., 2022) occurring in their surroundings that contribute to the detected SED of the AGN. Centimeter (cm) and millimeter (mm) wave spectra from the inflow of LLAGN, and jet bases, is generally dominated by synchrotron radiation (SR) due to the acceleration of charged particles along magnetic field lines (Bordovitsyn et al., 1999). Optical and short-wavelength (UV/X-ray) photons from bremsstrahlung (or free-free) accretion driven emission arise when charged particles are decelerated by an electric field, transforming kinetic energy into radiation of frequency equal to the difference between the initial and final states. Additionally, from mm to gamma rays, inverse Compton scattering occurs when energy from light waves is increased from lower frequencies due to interactions with charged particles (Blumenthal

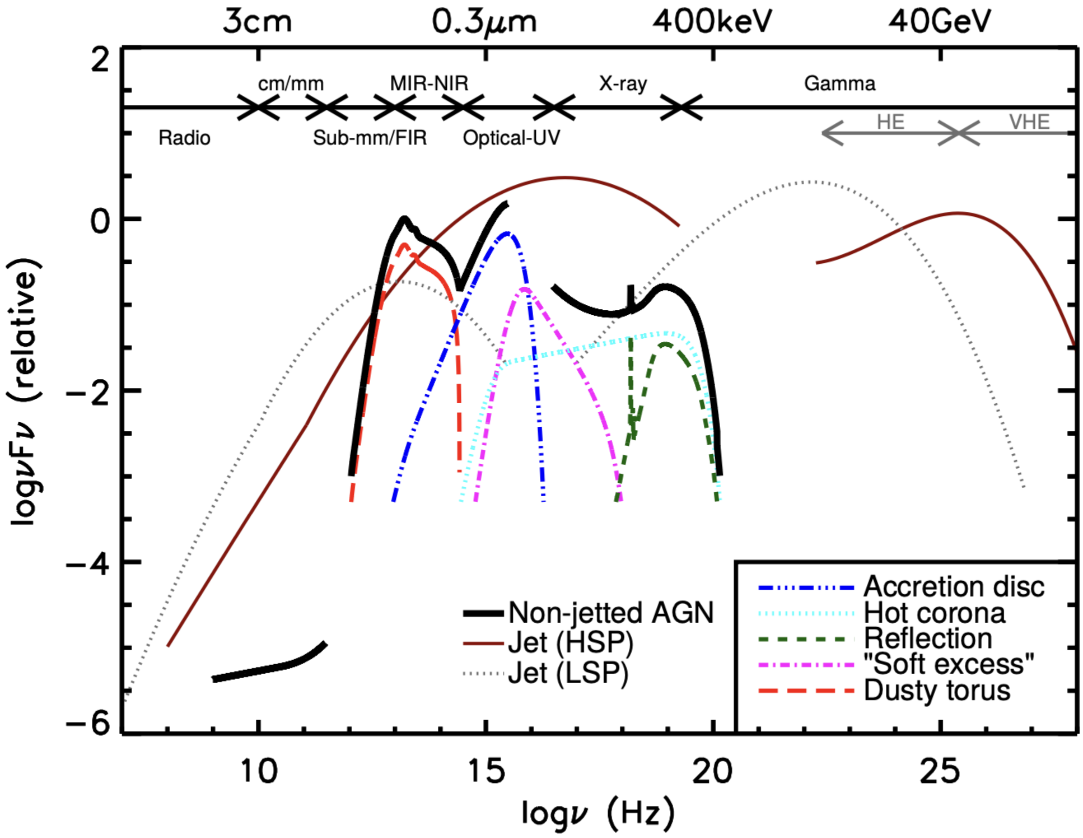

Figure 1.2.1: AGN SED representation based on observations from non-jetted quasars. Colored lines denote emission from different components as described in the legend. The total SED flux is depicted by a black solid line, while contributions from jet radiation are illustrated by solid brown and dotted gray curves, corresponding to high and low synchrotron peaked blazars, respectively. Figure from Padovani et al. (2017).

and Gould, 1970), as in the case of radio photons from the disk that get scattered to X-rays by relativistic electrons in the corona.

Empirical linear correlations between AGN luminosity at specific frequencies and BH properties have been found (Yi and Boughn, 1998; Merloni et al., 2003), motivating the need to understand the distinct contributions to the overall observed spectrum from various components within the nuclear region. However, existing correlations have predominantly relied on datasets characterized by limitations such as sample size constraints, reliance on single radio frequencies, or focus on specific AGN types. Such constraints may obscure the true behavior across the SMBH population, warranting a comprehensive reevaluation.

1.2.2 Accretion inflows

The measured SED of AGN vary depending on the present structures that govern the galactic core dynamics (see Figure 1.2.1 for an illustrative overview of a complete AGN spectrum; Padovani et al., 2017). Infalling material into a SMBH forms a flow of rotating gas and dust into a thin disk (Shakura and Sunyaev, 1973), where the energy generated per unit-mass accreted plays a crucial role in understanding its inner workings (Noble et al., 2011). In the case of an inefficient radiative output, one common solution to the hydrodynamic equations that aims to describe this phenomenon is the Advection Dominated Accretion Flow (ADAF; Ichimaru, 1977; Abramowicz et al., 1988; Narayan and Yi, 1994; Yuan and Narayan, 2014), which are posited to exist at sub-Eddington accretion rates (i.e., lower than the maximum at which it can accrete while maintaining virial equilibrium). The basic idea here is that the ions and electrons are not Coulomb-coupled. The primary heating goes into the protons which are “advected” into the event horizon. The electrons, which dominate emission, thus have lower temperatures, and the radiative power is thus a very small fraction of the accretion material. Figure 1.2.2 depicts an ADAF SED alongside the distinct contributions from various radiative processes as derived from semianalytical simulations.

Transport of matter through advection towards the center of the SMBH drives viscous heating, trapping thermal energy in the gas and making it cool inefficiently, by consequence, the bulk of the radiated photons predominantly follow a power-law spectrum via a combination of electron scattering, braking and SR processes, from radio to hard X-rays (Narayan and Yi, 1994; Mahadevan, 1997; Merloni et al., 2003; Gu et al., 2009; Yuan and Narayan, 2014). In order to determine if the thermally and viscously stable solution of hot radiatively inefficient accretion inflows (RIAFs) were an important factor in the observed emission profile of these astrophysical objects, Narayan and Yi (1995) first described the ADAF luminosity profile at low accretion rates (relative to Eddington) through means of semianalytical models characterizing heating and cooling processes of a two-temperature plasma of infalling material into a

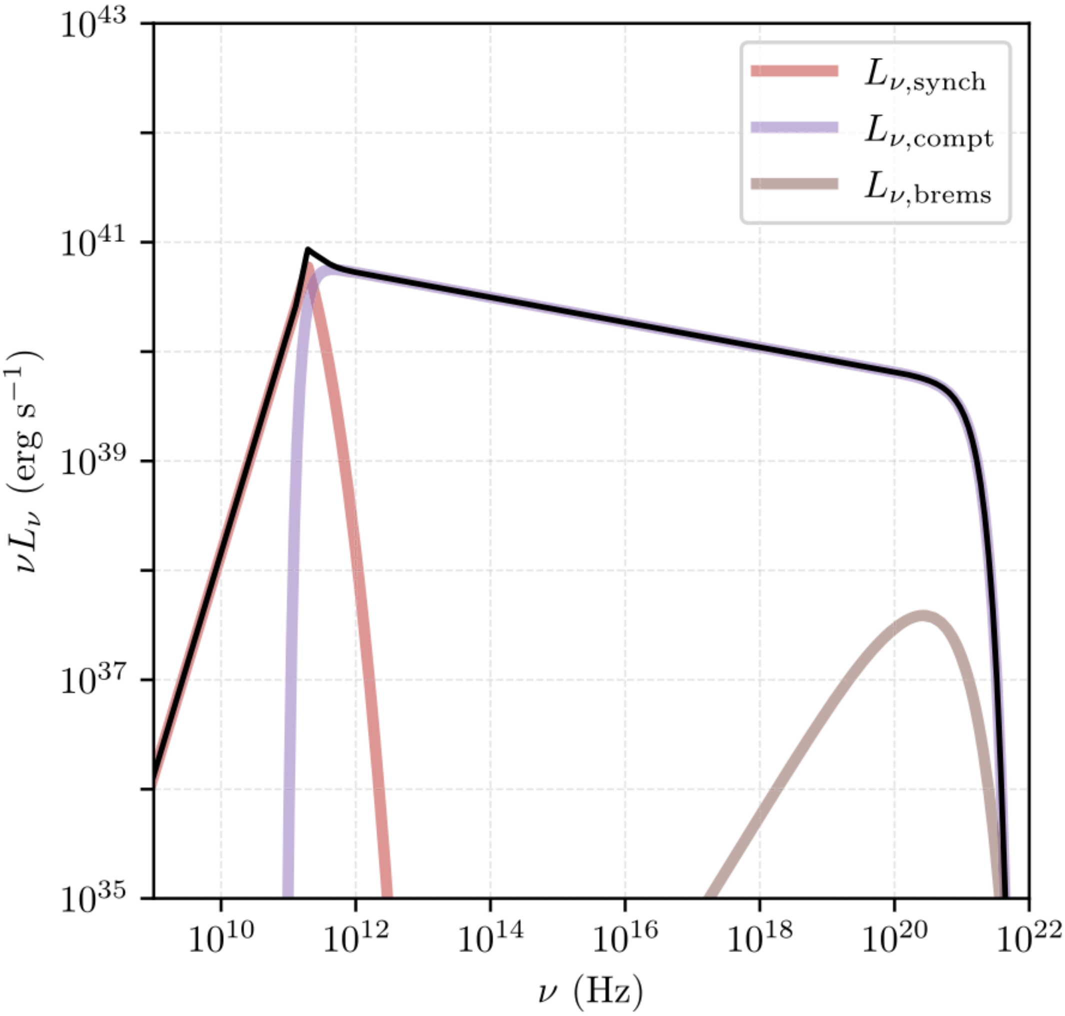

Figure 1.2.2: Predicted thermal ADAF SED of an M87-like SMBH from the semianalytical model developed by Pesce et al. (2021). Superposition of components is symbolized as a black curve, while red, purple and brown lines represent the contributions from thermal synchrotron, inverse Compton and bremsstrahlung radiative processes, respectively. Figure from Pesce et al. (2021).

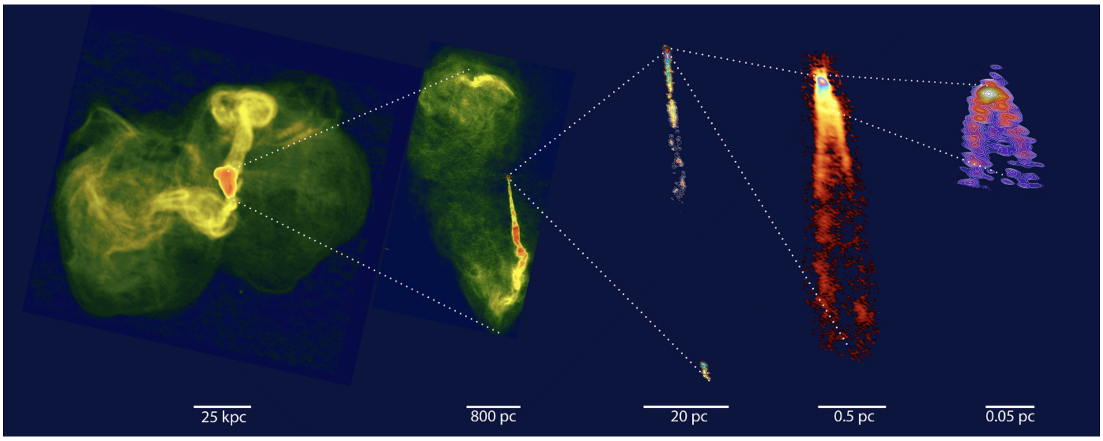

Figure 1.2.3: Views of the M87 jet at different observing scales, from the outer lobes (*left*) to the launching regions near its SMBH (*right*), where different structures are traced at each resolution. Figure from Blandford et al. (2019).

BH. Later, Mahadevan (1997) proposed that the spectra of LLAGNs could be reproduced using simple scaling laws to describe scale invariant ADAFs considering thermal radiative processes, showing that the resulting SEDs were dominated by particle magnetic acceleration (mostly radio) at low accretion rates while Comptonization governed the high end (largely hard X-ray), validating their predictions thanks to good agreement with observations. Recently, Pesce et al. (2021, hereafter P21) built upon and improved the groundwork laid by Mahadevan, developing a relatively straightforward and user-friendly ADAF SED model, as shown in Figure 1.2.2. It hinges on two primary free parameters: the BH mass ($M_{\rm BH}$) and the Eddington ratio ($l_{\rm Edd}$), while other physical properties of the system are preset to mimic characteristics akin to the observed accretion inflow of M87. The P21 ADAF model is used in this thesis.

1.2.3 Outflows

Another crucial aspect to consider regarding SMBH emission is the impact from galactic feedback mechanisms driven by material outflow arising within the inner regions of the nucleus. Observed across a wide range of scales in numerous AGN (Liu and Zhang, 2002; van Velzen et al., 2012; Blandford et al., 2019), Figure 1.2.3 shows one example of this phenomena found within the FR-I galaxy M87. These relativistic jets exhibit high energy, and emit radiation across the complete electromagnetic spectrum (Johnson et al., 2023), displaying significant heterogeneity in terms of morphology (one-sided, two-sided), scale (from astronomical units to Mpc), particle acceleration and other physical properties (Blandford and Payne, 1982; Blandford et al., 2019).

Theories about relativistic plasma exhaust mechanisms in AGN were originally proposed by Blandford and Rees (1974), who discussed a magnetohydrodynamical (MHD) model, suggesting that axisymmetric, and anti-parallel, jets are launched as consequence of rotational kinetic energy and angular momentum release from a heavily magnetized accretion disk with a magnetosphere surrounding the BH, where the outflowing material gets collimated perpendicular to the inflow due to toroidal magnetic stresses (Blandford and Payne, 1982; Sauty et al., 2002; Meier, 2003; Blandford et al., 2019). Although there exist ongoing debates surrounding the precise mechanisms governing jet launching and collimation (Boccardi et al., 2021), when present, their energetic output significantly influences the continuum and dynamics of the AGN, and in some cases, dominate the SED even at high frequencies (Spada et al., 2001; Falcke et al., 2004).

While not all types of AGN manifest jets, almost all radio galaxies with an LLAGN are radio-loud (RL), making them an essential consideration for an accurate portrayal of the total energy distribution in several systems (Bandyopadhyay et al., 2019). Spada et al. (2001) introduced a phenomenological model aimed at elucidating self-similar jets, grounded on the principles of internal shocks as a consequence of an intermittent launching mechanism, resulting in collisions of plasma at different velocities. These numerical simulations have been extensively employed both independently and in tandem with accretion models, proving to faithfully replicate observations in these scenarios (Spada et al., 2001; Yuan et al., 2005; Nemmen et al., 2014; Bandyopadhyay et al., 2019). This jet model is used in this thesis.

1.2.4 Other components and galaxy contamination

As exemplified in Figure 1.2.1, radiative cooling cradles are varied in nature. Thin accretion disk, dusty torus and/or a hot corona of gas can exert additional and substantial influence on AGN spectra across various frequencies (Ulrich et al., 1997), revealing an intricate interplay among the diverse elements shaping the SED. This underscores the importance of meticulous observing band selection when tracing specific components. Moreover, employing sensitive, high angular resolution instruments becomes imperative to mitigate obscuration and potential contamination from unrelated galactic phenomena, such as dust absorption of mm radiation, cm-wave radio emission from star forming H_{II} regions or supernova remnants, and high frequency photons from X-ray binaries (XRBs; Caswell and Haynes, 1987; Dubner and Giacani, 2015; Netzer, 2015; Almeida and Ricci, 2017; Hickox and Alexander, 2018).

1.3 Empirical correlations

1.3.1 Radio/X-ray correlation

Since the hard X-ray emission in the $2-10$ KeV band is less susceptible than its soft counterpart to contamination effects and extinction by metals in the torus and the BLR, or a hydrogen column density at larger scales, it developed into an essential tool to isolate ionizing radiation arising from the accretion

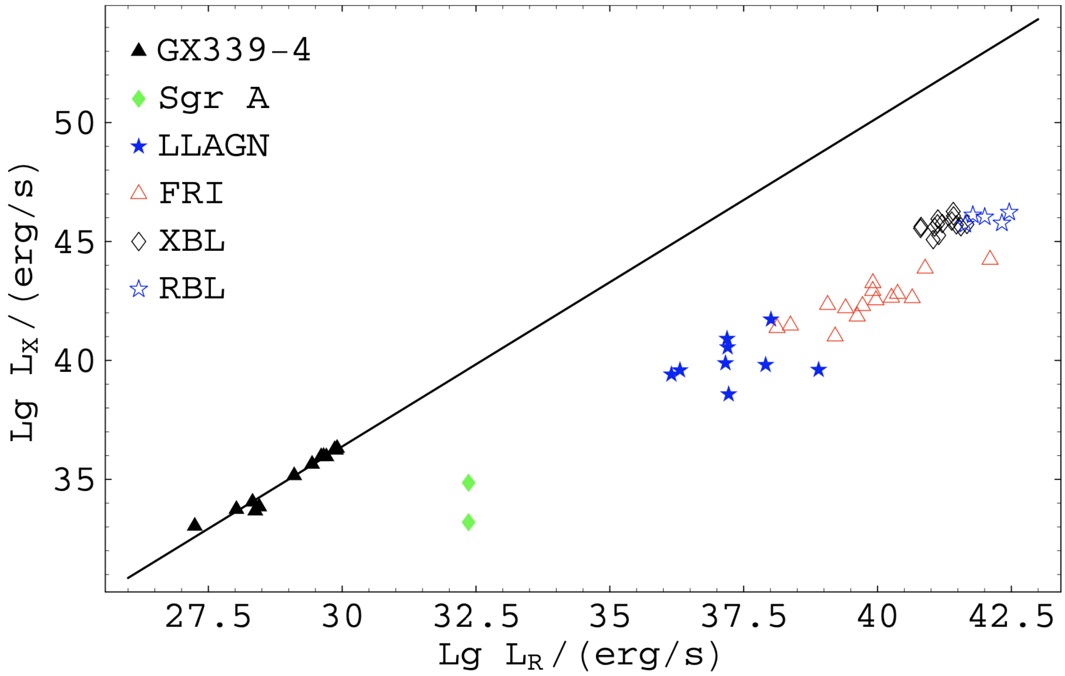

Figure 1.3.1: Observed 5 GHz radio luminosity to $2-10$ KeV hard X-ray luminosity correlation for XRB observations and different types of AGN (LLAGN, FR-I, X-ray and radio selected BL Lacs). Black line denotes the best-fit to the multiple epoch XRB measurements. Figure from Falcke et al. (2004).

inflow (Netzer, 2015; Almeida and Ricci, 2017; Hickox and Alexander, 2018). Several studies have theoretically predicted and empirically shown that the measured log scale luminosity in this band linearly correlates with radio emission at various cm-wave frequencies across diverse systems. Despite the absence of a unified explanation for this phenomenon across the accreting BH population, it is expected to arise from the activity of individual or combined components, such as ADAFs, jets, or coupling between inflow and outflow mechanisms (Narayan and Yi, 1994; Yi and Boughn, 1998; Hannikainen et al., 1998; Corbel et al., 2003; Gallo et al., 2003; Falcke et al., 2004; Yuan et al., 2005; Panessa et al., 2007; Vattakunnel et al., 2012; Fischer et al., 2021; Kawamuro et al., 2022; Ricci et al., 2023). Figure 1.3.1 illustrates the relation between the radio luminosity at 5 GHz and the $2-10$ KeV hard X-ray luminosity, for a sample of various AGN types and XRBs.

1.3.2 The fundamental plane of black hole activity

The empirical radio/X-ray correlation in galactic black holes (GBHs) and XRBs, without corrections applied to the high frequency measurements (i.e., by Doppler boosting, mass factor, or constant offset; Falcke et al., 2004), does not properly reproduce the trend followed by the SMBH sub sample. In this context, an observed non-linear dependence of scale invariant accretion powered jet flux at a given frequency (F_ν) on $M_{\rm BH}$ and $\dot{M}$, proven to be untied to a specific model and sensitive only to observable

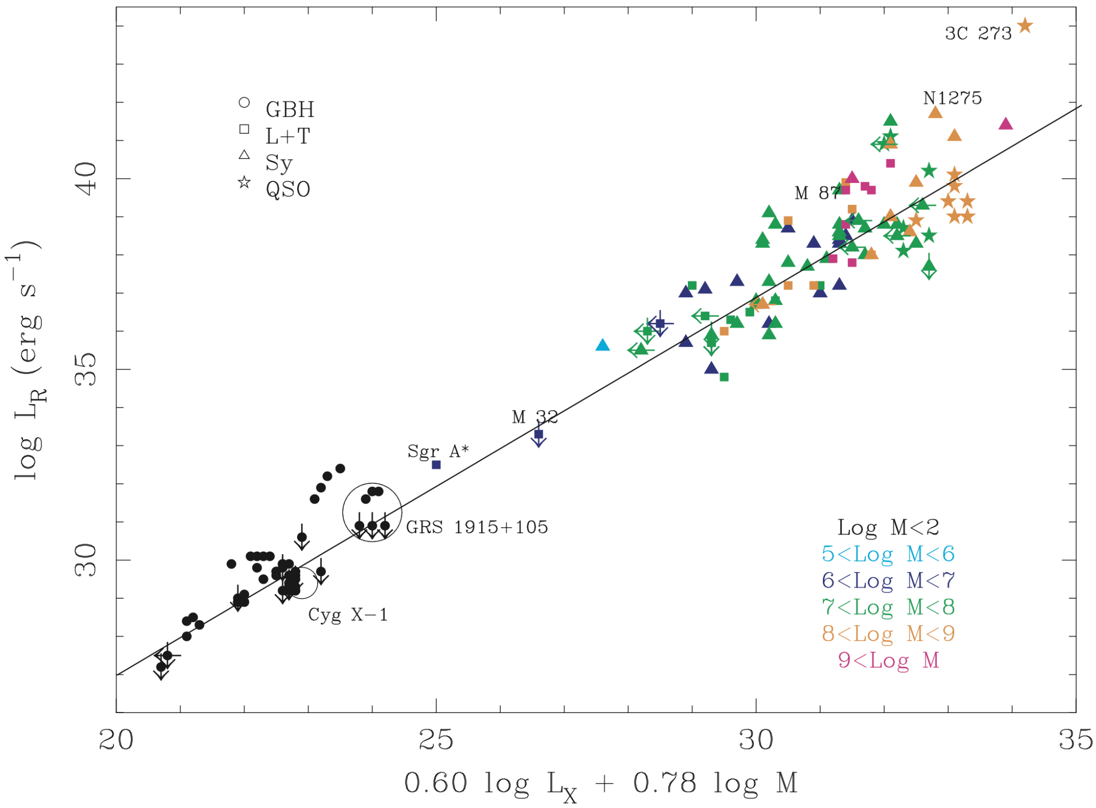

Figure 1.3.2: Two-dimensional view of the best-fit (black line) "Fundamental Plane" of BH activity for a sample of ~ 50 distinct observations of GBHs and ~ 100 nearby LLAGN. Figure from Merloni et al. (2003).

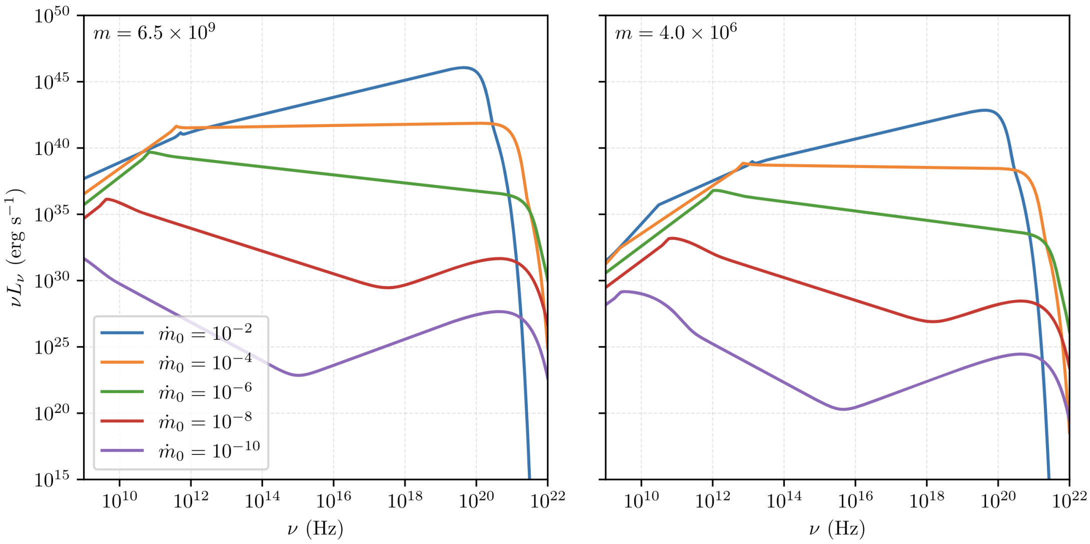

Figure 1.3.3: Semianalytic thermal ADAF SED model predictions for different values of $M_{\rm BH}$ (m) and $l_{\rm Edd}$ ($\dot{m}_0$). Both panels illustrate the expected scalings and variations in spectral shape with changes in the Eddington ratio for SMBHs with masses of 6.5×10^9 (*left panel*) and 4×10^6 (*right panel*). Figure from Pesce et al. (2021).

parameters (spectral slope and accretion mode; Heinz and Sunyaev, 2003), motivated the work of Merloni et al. (2003), who sought to unify the radio/X-ray correlation across the universe of detected BHs by taking into account the contributions to the cm-wave radio emission from both the mass of the central compact object, and the high energy luminosity (as an $\dot{M}$ proxy), following the linear function:

$$\log L_{\rm R} = \xi_{\rm RX} \log L_{\rm X} + \xi_{\rm RM} \log M_{\rm BH} + b_{\rm R}, \tag{1.3.1}$$

where $\xi_{\rm RX}$ and $\xi_{\rm RM}$ are the best-fit correlation coefficients of the log scale X-ray luminosity and BH mass, respectively, while $b_{\rm R}$ represents the y-axis intercept. Figure 1.3.2 shows the 2D correlation obtained after deriving the parameter set that best fitted a 5 GHz luminosity dataset of GBH and AGN, managing to consolidate the original relation within a 3D plane, which they called the "Fundamental Plane" (FP) of BH activity. The FP represents a powerful tool to constrain the underlying physical mechanisms that govern the distinct BH radiation processes across the complete spectrum. To this end, the ADAF solution turned to be of particular interest since it manifest similar scaling relations with both $M_{\rm BH}$ and $l_{\rm Edd}$ (see Figure 1.3.3; Merloni et al., 2003; Pesce et al., 2021). Consequently, direct comparison of observationally derived and theoretically predicted FP correlation coefficients (illustrated in Figure 1.3.4) revealed that RIAFs, jets, standard thin disk, and accretion-jet models were capable of describing the FP observations based on the chosen sample selection criteria.

By relying on just two relatively easy to obtain measurements (radio and X-ray luminosities), the FP relation can be reorganized as to provide a convenient, indirect method to obtain initial estimates of BH

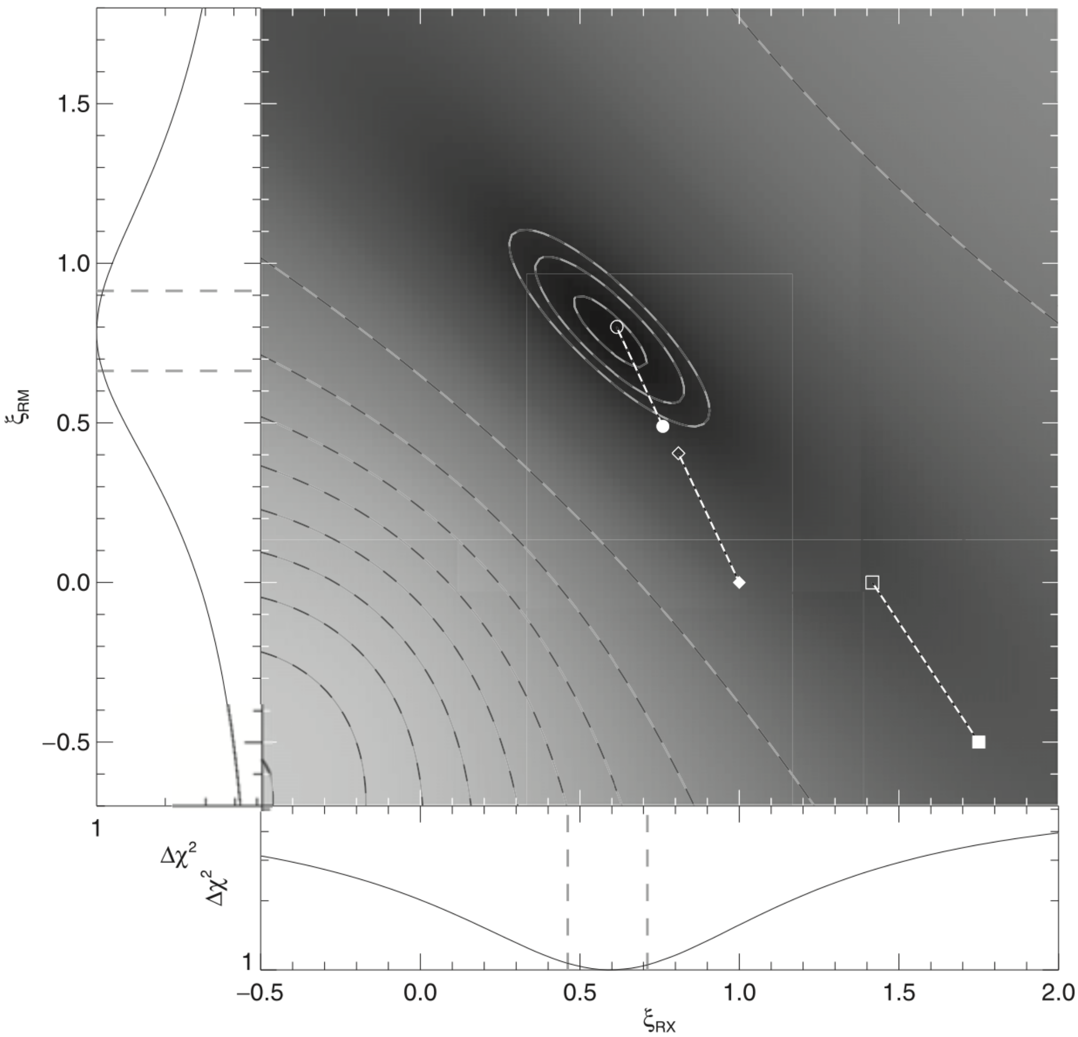

Figure 1.3.4: Theoretically expected FP correlation coefficient tracks (white dashed line) for flat (unfilled, $\alpha_R = 0$) to steep (filled, $\alpha_R = 0.5$) spectrum ADAF (circles), jet (diamonds) and standard thin disk (squares) scenarios. Shadowed region follows the obtained merit function ($\hat{\chi}^2$) distribution for the entire sample. Figure adapted from Merloni et al. (2003).

masses, specially in the absence of direct measurements, or lack of data that could enable the use of more precise methods (Merloni et al., 2003; Gültekin et al., 2009, 2014, 2019, 2022; Bariuan et al., 2022; Ruffa et al., 2024). The resulting equation for this end follows:

$$\log M_{\rm BH} = \xi_{\rm MX} \log L_{\rm X} + \xi_{\rm MR} \log L_{\rm R} + b_{\rm M}. \tag{1.3.2}$$

Subsequent FP studies have relied primarily on statistically refining the derivation of the plane coefficients and testing its validity across various radio frequencies and different samples of BH types. Saikia et al. (2018) used 1.4 GHz photometry from the Faint Images of the Radio Sky at Twenty-Centimeters (FIRST; White et al., 1997) survey (performed with the VLA in B-configuration) to verify its capability of tracing the nuclear jet activity by analyzing their position within the FP, finding that sources lie systematically above the plane due to fluxes being heavily contaminated by extended radio emission and other galactic processes, warranting careful consideration when including them into new derivations. In 2022, Gültekin et al. placed a sample of 5 GHz VLA data from 8 IMBHs into four distinct FP derivations from the same frequency, finding that composite AGN/starforming sources consistently followed the relation across the board, while pure star-forming and AGN classifications were inconsistent, therefore suggesting thorough examination of spectral indexes, radiative efficiency and accretion states when using the FP as a $M_{\rm BH}$ estimator. That same year, Bariuan et al. confirmed the initial hypothesis proposed by Merloni et al. (2003) that there could be a bifurcation, or discontinuity, in the plane between powerful RL and radio-quiet (RQ) quasars as a consequence of accretion mode changes, for a total of 225 RL and 128 RQ QSOs across a broad redshift range ($0 < z < 5$), while also evidencing a potential redshift evolution of the X-ray luminosity dependence for the RL sample. More recently, Ruffa et al. (2024) reported the discovery of a FP at 1 mm from a sample of 48 nearby LLAGN, showing that the relation could potentially arise from ADAF or jet emission, but highlighting that current comprehension of the underlying physics of this processes are not well constrained, thus introducing significant uncertainty to the results.

1.4 ETHER sample

Within this framework, the Event Horizon and Environs (ETHER) sample of SMBHs (Ramakrishnan et al., 2023; Hernández-Yévenes et al., 2024), represents a unique opportunity to test the existence of the FP across the radio regime from cm to sub-mm wave frequencies, evidence a potential evolution with redshift, compare the differences between the derived coefficients of separate AGN type sub-samples (distinguishing specific emission mechanisms), derive tailored $M_{\rm BH}$ estimation relations, analyze the effects of contamination thanks to multi resolution measurements, and more, by leveraging the large and heterogeneous nature of the dataset, that will allow for better overall statistics, and bypass some of the constrains faced by previous FP studies.

The physical implications, and both flux and mass estimates from FP relations derived out of qualifying sub sets of ETHER would help consolidate a more robust sample, assisting in its efforts to become the definitive catalogue of sources for which to perform SMBH observations with current and future generation VLBI instruments such as the EHT, who currently has a resolution of $\sim 22\ \mu$as at 230 GHz. The next-generation EHT (ng-EHT; Blackburn et al., 2019; Raymond et al., 2021; Johnson et al., 2023) at 86/345 GHz will increase its resolving power and flux sensitivity to $\sim 14\ \mu$as at $\sim$ 10s mJy, by nearly doubling the number of antennas in its array. Furthermore, long term efforts such as the space ng-EHT, will aim to push baselines to geostationary orbit (enabling for $3/5\ \mu$as observations at $230/345$ GHz) and the Lagrange 2 (L2; $0.18/0.11\ \mu$as at $230/345$ GHz) point, both of which, owing to an expanded Fourier plane coverage, higher frequency observing band, and the possibility of separate sub-array configurations, will achieve unprecedented angular resolutions and sensitivities, allowing for a substantial increase in the number of images of both high and low luminosity sources. The ng-EHT is already in the works, while the space ng-EHT is still in very early stages of development.

In Figure 1.4.1 the "Gold" ETHER sample (Ramakrishnan et al., 2023) is shown, each vertical line denotes SMBH shadow resolving limits for current and future EHT configurations, with high priority targets distributing towards the right side of the plot. In general, characteristics such as high flux, large size, and proximity are highly desirable for EHT proposals, although many objects currently present uncertain or low resolution measurements, and those with very weak flux detections are intrinsically hard to detect. Specific parameters such as galaxy inclination, together with nuclear structure and obscuration, should also be considered in observations. Figure 1.4.2 denotes how current semianalytic pure ADAF SED model predictions of the 230 GHz flux evolution through cosmic time are, in most cases, incapable of replicating the measured emission, specifically for farther away and jetted sources. In this scenario, the FP will also provide useful information for accurate SED reconstruction.

1.5 This work

The goals of the thesis presented here are manifold, though in the end they all work towards a more thorough study of the FP across multiple radio frequencies.

The first goal is to enhance the ETHER sample by incorporating additional data from existing radio and X-rays surveys, as well as crossmatches via automated queries to large databases (SDSS, SIMBAD and NED) to obtain information about galaxy morphology, AGN type, redshift, and multi-wavelength photometry.

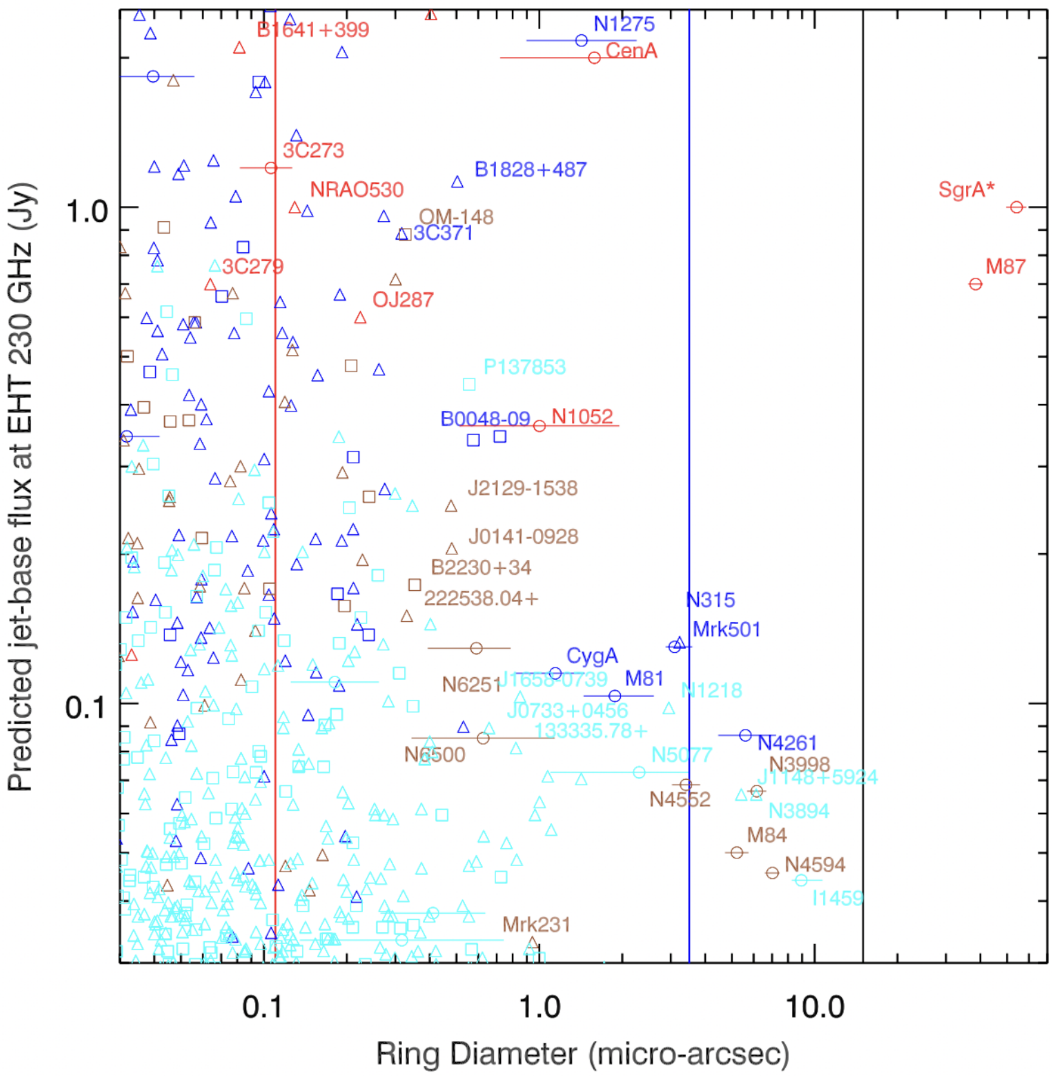

Figure 1.4.1: Jet-base flux prospects with EHT at 230 GHz as a function of micro-arcsec scale ring diameter for powerful VLBI sources in the ETHER sample. Colored lines denote maximum resolving power of ground-based EHT (black), geostationary baseline EHT (blue), and space ng-EHT at L2 point (red). Figure from Ramakrishnan et al. (2023).

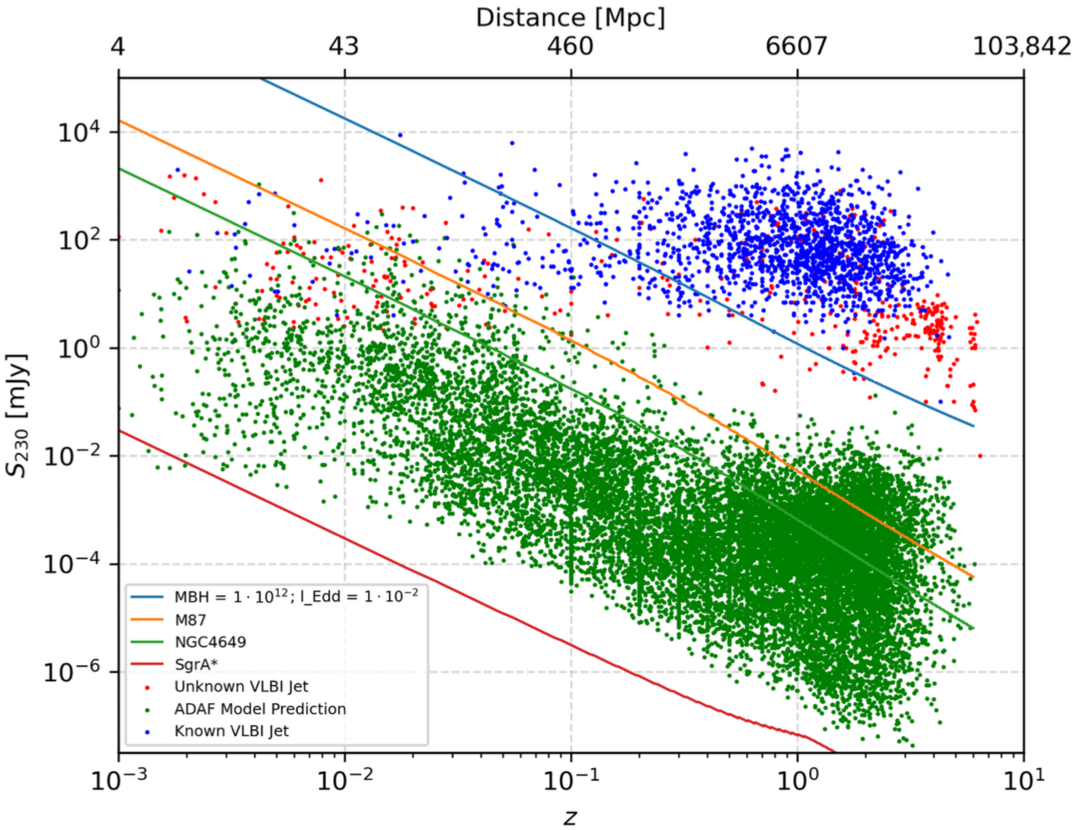

Figure 1.4.2: Measured (unknown and known VLBI jets as red and blue points, respectively) and predicted (dark green dots from P21 ADAF SED model) 230 GHz flux as a function of redshift (*bottom*) and distance (*top*) for ETHER sources. Colored lines denote expected flux evolution across cosmic time from the ADAF SED model for M87 (yellow), NGC4649 (green), SgrA* (red), and a hypothetical high mass, high Eddington ratio source (blue). Figure from Ramakrishnan et al. (2023).

Second, we will make use of ADAF, jet, and ADAF-Jet SED model fits to evaluate the relative contributions of ADAFs and jets to all SMBHs (with relevant data) in ETHER. This allows prediction of EHT-observed 230 GHz fluxes, and thus the selection of jet or accretion inflow dominated subsamples for observations with the EHT. Additionally, these ADAF and jet models will enable us to explore a full parameter space of allowed FPs and thus a contrast with observed FPs in the sample.

Thirdly, with an updated and uncensored (i.e., without upper limits) subsample from ETHER, all with a SMBH mass, radio luminosity, and hard X-ray luminosity, we can apply a least-squares fitting algorithm to investigate the relationship between low and high-frequency radio measurements in our samples with the hard X-ray luminosity. These can then be further refined via the inclusion of the BH mass, when determining the best-fit correlation coefficients between $M_{\rm BH}$, $L_{\rm R}$ and $L_{\rm X}$. To do this we use both an Ordinary Least Squares (OLS) multivariate linear regression with Monte Carlo (MC) sampling, and a minimization of a modified chi-square statistic (i.e., the merit function; Fasano and Vio, 1988; Merloni et al., 2003; Gültekin et al., 2009).

Together, these approaches enable us to derive predictor functions for radio luminosity and BH mass, and test the existence of the radio/X-ray correlation, and the FP of BH activity at 10 different radio frequencies (many of which have not been tested before) from cm to sub-mm wavelengths (i.e., 1.4, 2.2, 4.8, 8.6, 15, 23, 43, 86, 230 and 345 GHz), allowing for a comprehensive study of the discrepancies in dominant emission mechanisms between distinct AGN types, Eddington ratios and radio-loudness values, while determining if and how the FP evolves across cosmic time.

Overall, this thesis and the relations derived from it will greatly improve the completeness of the ETHER sample, and help constrain the SMBH observability prospects with current and future VLBI instruments, while providing a better understanding of the underlying physical mechanisms that give rise to the FP across the radio regime, supported by statistically significant correlations product of a much larger and diverse sample than those used in previous studies.

This thesis is organized as follows: Section 2 introduces the parent ETHER sample and details our work to expand it via automated queries to online databases, and crossmatches to additional radio and X-ray photometry catalogues. Section 3 presents the ETHER-FP sample and the methods used to derive the radio/X-ray correlations and FPs, as well as the obtained best-fit correlation coefficients and model statistics. Section 4 discusses the capabilities of current ADAF and jet SED models to explain the FP, and the differences observed in derived best-fit FP correlation coefficient across subsamples. We provide a summary and our overarching conclusions in Section 5, and include an appendix detailing the processing pipeline of SDSS data (Appendix A).

A flat ΛCDM cosmology, with $H_0 = 67.66\,{\rm km\,s^{-1}\,Mpc^{-1}}$, $\Omega_{\rm m} = 0.31$ and $\Omega_\Lambda = 0.69$ (Aghanim et al., 2020), is assumed, and errors are presented within 1σ confidence level unless stated otherwise.

Chapter 2

Data and software

2.1 ETHER sample

The ETHER sample (Ramakrishnan et al., 2023; Hernández-Yévenes et al., 2024) aims to be the definitive compilation of target SMBHs - across the universe - for current and future observations with VLBI instruments such as the EHT, the ng-EHT, the Global mm-VLBI Array (GMVA; Bandyopadhyay et al., 2019), and future efforts to expand EHT baselines to space, including low earth orbits, geostationary orbits and the L2 point (Event Horizon Telescope Collaboration et al., 2019; Pesce et al., 2021; Ramakrishnan et al., 2023). All of these will achieve unprecedented angular resolutions and sensitivities, allowing wide-ranging studies, e.g., the demographics of the innermost structures around SMBH, and binary SMBH in their gravitational wave emitting phase.

ETHER is a compilation of data from multiple existing catalogues, surveys, databases and the literature, with extensive ongoing efforts from the development team to supplement new critical data via high frequency VLBI observations of hundreds of SMBH, and 230 GHz surveys of thousands of SMBH. The sample is unique in that it represents one of the largest, if not the largest, compilations of SMBHs available to date, with over 3 863 709 different galaxies of all types spanning a broad redshift range. Due to its heterogeneous nature, the available fluxes in the radio and hard X-ray bands come from non-simultaneous observations taken with different instruments that have varying resolutions and sensitivities. Additionally, BH mass estimates are primarily derived through multiple indirect methods, such as reverberation mapping, "single-epoch" reverberation mapping extrapolations, stellar velocity dispersion estimates ($M_{\rm BH}-\sigma$; Saglia et al., 2016), and galaxy bulge luminosity estimations ($M_{\rm BH}-L_{\rm bulge}$). Only about 250 direct SMBH mass measurements are included.

Most of the sources in the sample have both an object name and/or positions, $\sim 93\%$ have a $M_{\rm BH}$ estimate or measurement, $\sim 99\%$ a redshift value, $\sim 24\%$ a morphological T-type value (T; Conselice, 2006), $\sim 6\%$ have a radio flux measurement at any of the 10 frequencies contemplated in ETHER, and $\sim 35\,000$ sources were detected in the $2-10$ KeV hard X-ray band.

More details on the sample statistics and an example of how ETHER was used to develop a more accessible method of indirectly estimating SMBH masses at low redshift through the use of Wide-field Infrared Survey Explorer (WISE; Wright et al., 2010) magnitudes and colors can be found in Ramakrishnan et al. (2023) and Hernández-Yévenes et al. (2024), respectively.

2.2 Automated database queries and supplementary catalogues

In order to expand the amount of data available for each source in the ETHER sample, especially the number of X-ray and cm/sub-mm radio fluxes (which will allow us to compile a more robust sample to study the FP at multiple frequencies), in this thesis we use automated queries to multiple online databases such as the Sloan Digital Sky Survey IV data release 17[1] (SDSS-IV; Blanton et al., 2017; Abdurro'uf et al., 2022), the Set of Identifications, Measurements and Bibliography for Astronomical Data[2] (SIMBAD; Wenger et al., 2000) and the NASA/IPAC Extragalactic Database[3] (NED), through the Python web-querying `astroquery`[4] (Ginsburg et al., 2019) coordinated package of `astropy` (Astropy Collaboration et al., 2013, 2018, 2022). We performed individual coordinate and/or name based queries to all of these databases for almost 1.2 million sources in ETHER. Given the size of the sample, and the specific automated query guidelines and limits of each service, this process was and is very time consuming.

In order to minimize the file size of the products from the `astropy` queries, we do not store query cache data but instead only save the match with the smallest separation from the input coordinates. This match may also satisfy other conditions depending on the information provided by the database, such as the presence of redshift and/or stellar velocity dispersion (σ) values in the case of SDSS (see Appendix A for details and constraints on how we use SDSS σ values to derive BH masses). To avoid repetitions of already performed queries, a record of all queries is maintained, so that these objects can be skipped in posterior query runs.

Due to the large number of objects in ETHER, and the automated nature of this process, it is important that the output tables are post-processed with care. For each database we establish constrains when

[1] https://www.sdss4.org/dr17

[2] https://simbad.unistra.fr/simbad/

[3] The NASA/IPAC Extragalactic Database (NED) is funded by the National Aeronautics and Space Administration and operated by the California Institute of Technology. https://ned.ipac.caltech.edu

[4] https://astroquery.readthedocs.io/en/latest/index.html

post-processing the results, in the particular situation of SDSS we first make sure that the source is not classified as a star within the database as well as checking that it follows the aforementioned restrictions. In the cases of SIMBAD and NED we limit the search to only sources whose listed object type aligns with either a galaxy or AGN type, while retaining only the match with the least separation and higher number of references available. NED in particular is very unique since it is the only one of the three queried databases that allows us to extract multi-frequency photometry tables through name based queries, thus representing our only source of radio and X-ray fluxes through astroqueries. When a table is obtained we rule out any emission line and negative fluxes and extract the highest resolution, nuclear flux density measurements and errors available in the $2-10$ KeV hard X-ray band and at the key radio frequencies stored in the ETHER database.

Our automated queries managed to significantly increase the availability of galaxy name, precise coordinates, morphology, AGN type, redshift, stellar velocity dispersion and distance, together with hard X-ray and multi-frequency radio photometry data. Specifically, from SDSS we obtained 980 328 matches, all of which had a listed galaxy class and redshift value, 570 759 a sub class and 355 253 a σ value. From SIMBAD 409 382 sources matched to ETHER, all of them had available coordinates, object type and distance data, 11 890 a morphological type and 407 656 a redshift value. As for the NED main table, 1 176 319 matches were found, all of them containing information on coordinates, object name and type, and 950 959 redshift values, while in terms of photometry, we retrieved: 90 765 fluxes at 1.4 GHz, 4 038 at 2.2 GHz, 22 704 at 5 GHz, 11 211 at 8.6 GHz, 2 494 at 15 GHz, 2 616 at 23 GHz, 1 409 at 43 GHz, 748 at 86 GHz, 1 037 at 230 GHz and 875 at 345 GHz, and 18 888 $2-10$ KeV hard X-ray flux measurements.

Additionally, cross matches to obtain high resolution nuclear $2-10$ KeV hard X-ray fluxes from the extended ROentgen Survey with an Imaging Telescope Array (eROSITA; Predehl et al., 2021) All Sky Survey (eRASS1; Merloni et al., 2024) hard catalogue ($\sim 5\,500$ sources), the Chandra Source Catalogue (CSC; Evans et al., 2010) through the CSCView application ($\sim 35\,000$ galaxies), 4.8 GHz radio photometry from the National Radio Astronomy Observatory Very Large Array Sky Survey (NRAO VLASS, $\sim 194\,000$ objects) and the Faint Images of the Radio Sky at Twenty centimeters (FIRST; White et al., 1997, $\sim 117\,000$ sources) 1.4 GHz survey were performed and the matched data incorporated into the sample. Data at a given frequency from different catalogs or databases are consolidated in ETHER, so the sum of the numbers obtained from individual surveys stated above does not necessarily add up to the final statistics, i.e., individual data points are overwritten by those coming from telescopes with better resolution, methods, or overall reliability. It is important to note that hard X-ray fluxes ingested from NED, CSC and eRASS1 (Hard) catalogues are not corrected for absorption, and that we ingest their values as specific X-ray fluxes (erg s^{-1} cm^{-2}) at the mid-frequency of the specified band, which could induce a slight offset between observed and predicted values even in the best case scenarios, such as

M87.

Lastly, it is relevant to mention that ETHER is constantly being updated and expected to grow significantly with future data releases.

Chapter 3

Fundamental plane at multiple wavelengths

3.1 ETHER-FP sample

In order to study if, and how, the FP of BH activity holds across multiple radio frequencies from cm to sub-mm wavelengths, and to test for noticeable changes or trends with increasing frequency, we select a subset of sources from the main ETHER sample, which we refer to as the ETHER Fundamental Plane sample (hereafter ETHER-FP). This subset consists of only those objects with a value for $M_{\rm BH}$ (either directly measured or estimated through indirect methods; see Section 2.1), a flux detection in any of the radio frequencies contemplated in ETHER, a flux detection in the hard X-ray band ($2-5$ KeV or higher), and a redshift and/or distance, required to convert from observed-frame flux to specific rest-frame luminosity following:

$$\nu L_\nu = \nu S_\nu 4\pi \left(d(1+z)^2\right)^2, \tag{3.1.1}$$

where S_ν is the observed radiation at a frequency $\nu_{\rm obs}$, d is the angular diameter distance to the source, and z its redshift (Scoville, 2012; Gültekin et al., 2019; Ruffa et al., 2024). This leaves us with a total of 3 411 sources of the ~ 3.8 million in ETHER, a significant reduction in size but more than an order of magnitude larger than previous FP studies (e.g., Merloni et al., 2003; Falcke et al., 2004; Gültekin et al., 2019; Bariuan et al., 2022; Ruffa et al., 2024, and others.), although not all galaxies have flux data in all of the radio bands, so individual radio-frequency sub samples vary in size.

We identify 244 known powerful jetted sources at cm-wavelengths within our sample by coordinate matching with the low luminosity radio galaxy catalogue of van Velzen et al. (2012) and by IAU/Object name matching to the Liu and Zhang (2002) list of extra-galactic radio jets, most of which are highly luminous sources. Of these, 175 come from van Velzen's catalog, while the remaining 69 are in Liu & Zang's catalog.

Of the ETHER-FP sample, 1 311 sources have a listed AGN type in SIMBAD, encompassing a variety of Seyferts, BL Lacs, Blazars, LINERs and QSOs. A galaxy morphological T-type is available for 1 403 galaxies, with values ranging from -5 to 8, corresponding to early-type to late-type galaxies respectively. These T-type values were obtained via crossmatches to NED or SIMBAD via astroqueries, and from the literature.

Figure 3.1.1 shows the distribution of redshift, M_{BH}, specific radio and X-ray luminosities, radio-loudness, and Eddington ratio, for the ETHER-FP sample with 5 GHz fluxes. We note that these distributions are different at each radio frequency in ETHER. For more details on the sample sizes, and the minimum/maximum values of the aforementioned parameters at the multiple radio frequencies considered in the ETHER-FP sample we refer to Table 3.1.1.

ETHER-FP, as well as its parent sample, is a highly heterogeneous compilation of objects, owing to the diverse origins of the literature compilations from which it is built (multiple epochs and instruments), with the presence of both low and high redshifts and luminosities, IMBHs and SMBHs of different AGN type, diverse host galaxy morphology (early and late-types), different radio-loudness values (mostly radio quiet and a few RL; Bariuan et al., 2022), a range of Eddington ratios, and varying levels of jet presence/dominance.

Another limitation of our analysis with ETHER-FP is that we assume a locally flat spectrum for K-corrections. Further, the non-simultaneous nature of the flux measurements of both radio and X-ray fluxes can create a significant source of scatter due to the known variability in luminosity of specific AGNs types, as noted in Section 1.1.2, while low resolution flux measurements could be contaminated by other galactic processes or extended radio emission which we have not corrected for, and thus not correctly trace nuclear activity.

3.2 Radio/X-ray luminosity correlation at multiple wavelengths

As briefly outlined in Section 1.3.1, over the years there has been extensive theoretical work (Narayan and Yi, 1994) and observational evidence (Hannikainen et al., 1998) that suggest a strong correlation between the radio emission at various cm-wave frequencies and 2-10 KeV hard X-ray radiation within the vicinity of central SMBHs. Early studies about the potential contribution of ADAFs to the cosmic X-ray background showed a proportionality between the radio luminosity at 4 different wavelengths (1.4, 5, 15

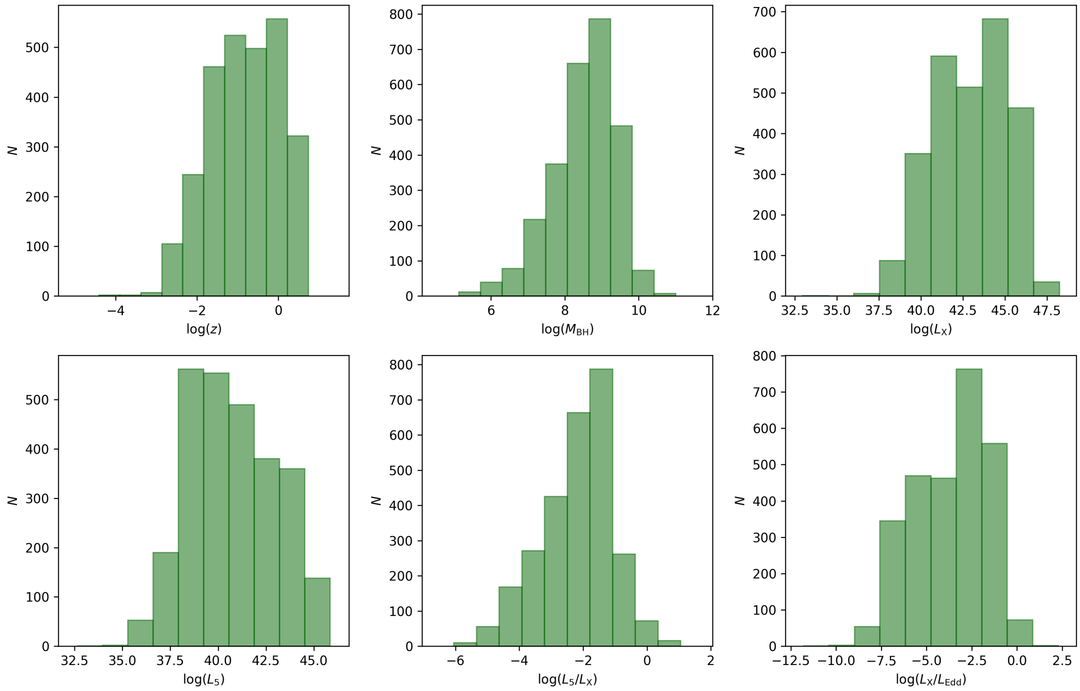

Figure 3.1.1: Distribution of ETHER-FP properties (in log scale) at 5 GHz. *Top left panel*: Redshift. *Top middle panel*: BH mass in solar masses. *Top right panel*: Specific 2-10 KeV hard X-ray luminosity in erg s^{-1}. *Bottom left panel*: Specific 5 GHz luminosity in erg s^{-1}. *Bottom middle panel*: Radio loudness. *Bottom right panel*: Eddington ratio.

Table 3.1.1: ETHER-FP sample statistics at different radio frequencies.

ν_{obs} (1)	N (2)	z (3)	$\log(M_{BH}/M_\odot)$ (4)	$\log(L_X/\text{erg s}^{-1})$ (5)	$\log(L_R/\text{erg s}^{-1})$ (6)	$\log(L_R/L_X)$ (7)	$\log(L_X/L_{Edd})$ (8)
1.4	2502	[-0.001, 5.80]	[5.01, 11.00]	[36.06, 47.88]	[32.73, 45.37]	[-6.42, 1.71]	[-9.83, 2.28]
2.2	738	[-0.001, 5.47]	[5.01, 10.30]	[37.26, 48.23]	[35.83, 45.44]	[-5.43, 1.21]	[-9.76, 2.28]
4.8	2730	[-0.001, 5.47]	[5.13, 11.00]	[32.94, 48.23]	[32.65, 45.84]	[-6.05, 1.05]	[-11.79, 2.28]
8.6	1021	[-0.001, 5.47]	[5.22, 10.60]	[32.94, 48.23]	[31.76, 45.84]	[-5.94, 1.81]	[-11.79, 2.28]
15	512	[-0.001, 5.47]	[6.34, 10.30]	[32.94, 48.23]	[33.08, 46.76]	[-5.10, 1.41]	[-11.79, 0.64]
23	485	[-0.001, 4.31]	[5.77, 10.60]	[32.94, 48.23]	[32.51, 46.85]	[-5.17, 1.53]	[-11.79, 0.64]
43	399	[-0.001, 5.47]	[5.66, 10.13]	[32.94, 48.23]	[33.58, 46.94]	[-3.90, 2.50]	[-11.79, 0.64]
86	411	[-0.001, 4.62]	[6.13, 10.25]	[37.26, 48.23]	[37.99, 47.18]	[-2.94, 2.07]	[-8.73, 2.28]
230	492	[-0.001, 4.62]	[5.13, 11.00]	[32.94, 48.23]	[34.26, 47.33]	[-4.55, 2.87]	[-11.79, 2.28]
345	393	[-0.001, 5.06]	[5.72, 10.08]	[32.94, 48.23]	[35.10, 47.37]	[-4.34, 3.63]	[-11.79, 1.00]

Notes. Col. (1): Observed radio frequency in GHz; Col. (2): Number of sources; Cols. (3)-(8): Minimum and maximum values for redshift, BH mass, hard X-ray luminosity, radio luminosity, radio-loudness and Eddington ratio.

and 20 GHz) and the X-ray luminosity in the 0.5-2 and 2-10 KeV bands, evidenced within both ADAF SED simulations and measurements from a small sample of nearby LINER and Seyfert type galaxies (Yi and Boughn, 1998). Corbel et al. (2003) also found strong evidence for a physical coupling between the aforementioned quantities within the BH candidate GX 339-4, noting that a significant fraction of the high energy emission was consistent with optically thin synchrotron emission from a jet, effectively meaning that the relation can be explained through different emission mechanisms. Additionally, both Gallo et al. (2003) and Panessa et al. (2007), managed to arrive to the same conclusions for a sample of 10 nearby L/H state BH candidates (BHCs) and a sample of Seyfert and low luminosity radio galaxies across many orders of magnitude, respectively, with Falcke et al. (2004) providing evidence for a unification of this phenomena across a wide variety of AGN types. According to Vattakunnel et al. (2012), this unification also applies to both star forming galaxies and AGNs, without signs of redshift evolution up to $z \sim 1.5$. Most recently, Fischer et al. (2021) suggested that the relation could be due to extended radio emission, since higher resolution core radio flux measurements lie below predictions. Additionally, Kawamuro et al. (2022) used high resolution data of 98 nearby ($z < 0.05$) AGNs to study the correlation between $2-10$ KeV X-ray luminosity and radio emission at 1.3 mm (230 GHz), following observational results that suggested the presence of radio emission on scales of a hot X-ray corona around the SMBH. Since mm-wave radiation could originate within or around the same region thanks to self-absorbed synchrotron radiation, it opened the possibility that both quantities could be linked. In this context, the authors managed to derive a tight correlation between both quantities that served as supporting evidence for the hypothesis.

The existence of this radio/X-ray correlation, especially in the context of the ETHER sample, could provide a useful and simple method of predicting missing cm/sub-mm flux data from X-ray measurements in the absence of any BH mass estimates, evaluate potential radio emission mechanisms, and constrain the observability prospects of individual SMBHs with current and future VLBI efforts.

To this end, we test how these two quantities relate to each other for the many radio frequencies within our sample, by employing a simple bi-variate least squares linear regression method between radio and hard X-ray luminosities, derived from flux detections in both features after Eq. ((3.1.1)), using the `linregress` function of the `scipy.stats` Python library (Virtanen et al., 2020), following a linear model of the form:

$$\log L_{\rm R} = \xi_{\rm X} \log L_{\rm X} + \beta_0, \tag{3.2.1}$$

where $\xi_{\rm X}$, and β_0, represent the slope and the y-axis intercept term, respectively.

Table 3.2.1 summarizes the results of this exercise for the complete ETHER-FP sample. In it, we report the derived best-fit slopes and intercept terms (with their estimated standard errors) from the regression

Table 3.2.1: Radio/X-ray luminosity linear least-squares regression parameters and statistics for the complete ETHER-FP sample, at multiple radio frequencies.

X	Y	N	ξ_X	β_0	σ_{int}	R^2_{adj}	ρ	p
(1)	(2)	(3)	(4)	(5)	(6)	(7)	(8)	(9)
$\log L_{X,2-10}$	$\log L_{1.4}$	2502	0.834±0.012	4.41±0.497	1.271	0.673	0.818	0.0
$\log L_{X,2-10}$	$\log L_{2.2}$	738	0.931±0.012	0.736±0.511	1.889	0.895	0.945	0.0
$\log L_{X,2-10}$	$\log L_{4.8}$	2730	0.900±0.010	2.099±0.410	1.093	0.766	0.879	0.0
$\log L_{X,2-10}$	$\log L_{8.6}$	1021	0.976±0.013	-0.879±0.579	1.031	0.842	0.928	0.0
$\log L_{X,2-10}$	$\log L_{15}$	512	1.089±0.021	-5.295±0.916	1.036	0.845	0.916	2.65×10^{-204}
$\log L_{X,2-10}$	$\log L_{23}$	485	1.084±0.025	-4.876±1.098	1.155	0.798	0.925	6.42×10^{-205}
$\log L_{X,2-10}$	$\log L_{43}$	399	0.935±0.018	2.239±0.797	0.717	0.874	0.910	4.04×10^{-154}
$\log L_{X,2-10}$	$\log L_{86}$	411	0.984±0.018	0.175±0.812	0.723	0.877	0.907	4.14×10^{-156}
$\log L_{X,2-10}$	$\log L_{230}$	492	1.031±0.025	-2.169±1.079	1.327	0.781	0.889	9.16×10^{-169}
$\log L_{X,2-10}$	$\log L_{345}$	393	0.815±0.018	8.086±0.784	0.933	0.841	0.927	3.78×10^{-168}

Notes. Cols. (1), (2): Independent (X) and dependent (Y) variables; Col. (3): Sample size; Cols. (4)-(9): Best-fit linear regression slope (ξ_X), y-axis intercept (β_0), intrinsic scatter (σ_{int}), adjusted coefficient of determination (R^2_{adj}), Spearman rank-order correlation coefficient (ρ) and associated p-value.

at each radio frequency, the number of objects, an intrinsic scatter or root mean square error (RMSE) of the form:

$$\sigma_{int} = \sqrt{\sum_{i=1}^{N} \frac{(\hat{y}_i - y_i)^2}{N}}, \tag{3.2.2}$$

which measures the deviation of the real data from the fitted function, where $\hat{y}_i$ and y_i are the predicted and observed radio luminosity values, respectively. An adjusted coefficient of determination, that quantifies how much of the variation in the response variable (L_R) is predicted by the statistical model, while taking into account the number of degrees of freedom, is estimated following:

$$R^2_{adj} = 1 - \frac{(1-R^2)(N-1)}{N-p-1}, \tag{3.2.3}$$

where p is the number of independent variables, and R^2 the coefficient of determination, which is described as

$$R^2 = 1 - \frac{\sum_{i=1}^{N} (y_i - \hat{y}_i)^2}{\sum_{i=1}^{N} (y_i - \bar{y}_i)^2}, \tag{3.2.4}$$

with $\bar{y}_i$ corresponding to the arithmetic mean of the measurements. Additionally, Spearman rank order correlation coefficient (ρ), and the associated p-value (p), are retrieved from the `statistic` and `pvalue` methods of the `scipy.stats.spearmanr` function, respectively. The former allows to measure the strength and direction of the correlation, while the latter defines the probability of it happening assuming that the null hypothesis (i.e., the observed behaviour does not exist) is correct.

The results shown in Table 3.2.1, and illustrated in Figure 3.2.1, clearly demonstrate that the two quantities are indeed strongly positively correlated within our samples, with no evident trends with changing radio frequency. This fact is supported by a correlation coefficient value of $\rho > 0.8$ at all frequencies, and

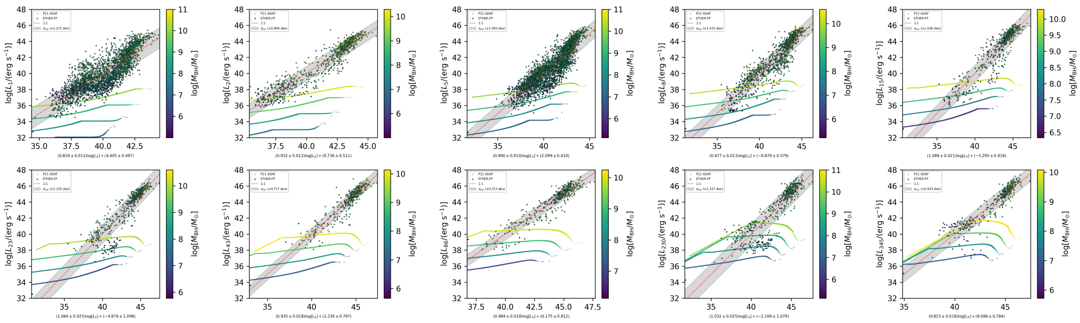

Figure 3.2.1: Radio/X-ray luminosity correlation for all ETHER-FP sources at multiple cm/sub-mm frequencies. *Top row*: From left to right the radio frequencies are 1.4, 2.2, 4.8, 8.6 and 15 GHz; *Bottom row*: From left to right the radio frequencies are 23, 43, 86, 230 and 345 GHz. Detections are presented as circles with black edges, while colored curves denote expected P21 ADAF SED model values for fixed BH masses of $\log[M_{\rm BH}/M_{\odot}] = 7$, 8, 9 and 10 (in ascending order) with Eddington ratio changing from $\log[L_{\rm X}/L_{\rm Edd}] = -7$ to -1.8, as it goes left to right. Marker color corresponds to the mass of the central compact object, mapped following the bar at the side of each subplot. The red dashed line represents the best linear fit to the data, while the grey region highlights the range of intrinsic scatter within $\pm 1\sigma$.

statistically significant p-values much lower than 0.05, meaning that its highly unlikely that the observed relations occurred by mere chance. On the other hand, we note that the percentage of the variability that is not explained by the fit, as well as the intrinsic scatter, can be considerable ($R^2_{\rm adj} < 0.7$ and $\sigma_{\rm int} > 1$ dex) at specific frequencies, while in others (mainly at shorter wavelengths) the correlation seems tighter.

Differences in the best-fit model parameters and the large scatters obtained may result from sample selection biases due to the heterogeneity in AGN types among the subsamples (Plotkin et al., 2012). This is evident in Figure 3.2.2, where it becomes clear that at certain frequencies, the samples are mostly dominated by QSOs at high redshifts. Additionally, since a clear correlation between radio and hard X-ray flux is not observed for objects within 1 000 Mpc, the observed behavior in luminosity space may instead be due to a proportional relationship between distances. It could also suggest the presence of an additional component or an unaccounted factor that significantly influences the energy output at these wavelengths, especially at those frequencies that exhibit large intrinsic scatter relative to others.

3.3 Fundamental plane parameter derivation at multiple wavelengths

3.3.1 Radio luminosity predictor functions

Based on the premise that in AGN, the accretion powered jet flux at a given frequency is proportional to the mass of the central compact object, as it has been shown in previous works (see Section 1.3.2), the inclusion of SMBH mass as a third parameter can help tighten and unify the radio/X-ray correlation

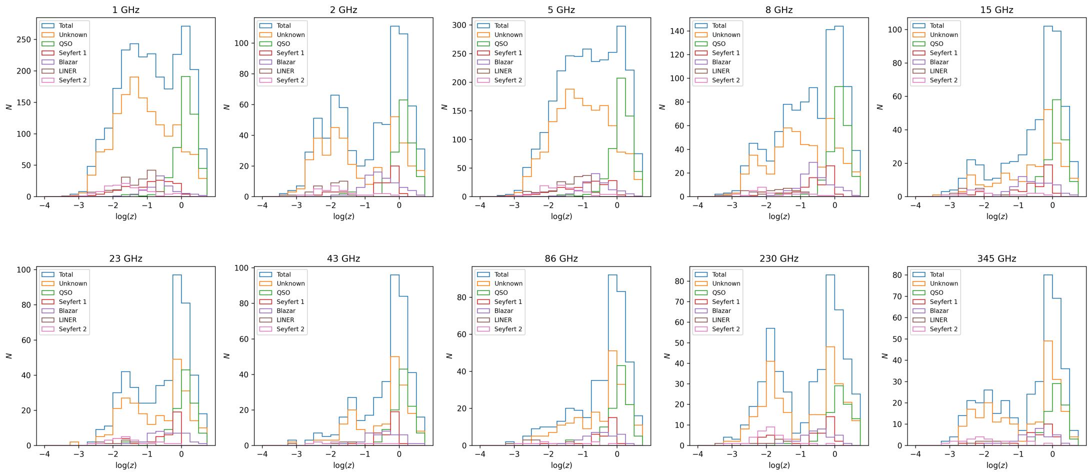

Figure 3.2.2: Redshift distribution of distinct AGN types in the ETHER-FP sample, separated by radio frequency.

across a wide range of BHs, forming what is known as the FP of BH activity.

Motivated by this and the large scatters seen at some frequencies within our radio/X-ray correlation results, we search to weigh the relative contribution to the radio luminosity of both BH mass and X-ray emission, by deriving new FP relations in the ETHER-FP sample. To this end, we employ the formalism first presented in Merloni et al. (2003), which has also been used in many subsequent FP studies (e.g., Falcke et al., 2004; Gültekin et al., 2009; Plotkin et al., 2012; Bariuan et al., 2022; Ruffa et al., 2024), where they defined the underlying relation as:

$$\log L_{\rm R} = \xi_{\rm X} \log L_{\rm X} + \xi_{\rm M} \log M_{\rm BH} + \beta_0, \quad (3.3.1)$$

where $L_{\rm X}$ is the specific $2-10$ KeV hard X-ray luminosity, $L_{\rm R}$ is the specific radio luminosity, $M_{\rm BH}$ is the mass of the BH, while $\xi_{\rm X}$, $\xi_{\rm M}$ and β_0 are the correlation coefficients of the accompanying independent variables and the constant offset, respectively.

We emphasize that for this work we have assumed a locally flat spectrum at each radio and X-ray frequency, and we have not corrected fluxes for absorption, nor for Doppler boosting of synchrotron radiation in the case of blazars (Gallo et al., 2003). Further, we have not subtracted out possible contamination of extended radio emission from other galactic processes. All of the above factors could introduce significant scatter to any statistical model.

To find the best-fit correlation coefficients for our samples, we make use of two distinct methods: an OLS multivariate linear regression, and a numerical merit function minimization technique, both of which

Table 3.3.1: Best-fit FP model parameters and statistics from multivariate OLS linear regression for the complete ETHER-FP sample, at multiple frequencies.

X	Y	Z	N	ξ_X	ξ_M	β_0	σ_{int}	R^2_{adj}	ρ	p
(1)	(2)	(3)	(4)	(5)	(6)	(7)	(8)	(9)	(10)	(11)
L_X	M_{BH}	$L_{1.4}$	2502	0.76 ± 0.01	0.39 ± 0.03	4.22 ± 0.49	1.23	0.69	0.83	0.0
L_X	M_{BH}	$L_{2.2}$	738	0.89 ± 0.01	0.13 ± 0.04	1.20 ± 0.54	0.91	0.89	0.94	0.0
L_X	M_{BH}	$L_{4.8}$	2730	0.84 ± 0.01	0.31 ± 0.02	1.96 ± 0.41	1.08	0.77	0.88	0.0
L_X	M_{BH}	$L_{8.6}$	1021	0.93 ± 0.01	0.23 ± 0.04	-1.02 ± 0.59	1.03	0.84	0.92	0.0
L_X	M_{BH}	L_{15}	512	1.06 ± 0.02	0.16 ± 0.06	-5.24 ± 0.95	1.07	0.84	0.89	4.4×10^{-180}
L_X	M_{BH}	L_{23}	485	1.01 ± 0.03	0.44 ± 0.06	-5.54 ± 1.09	1.14	0.81	0.91	1.47×10^{-181}
L_X	M_{BH}	L_{43}	399	0.93 ± 0.02	-0.05 ± 0.05	2.93 ± 0.87	0.75	0.86	0.89	1.63×10^{-133}
L_X	M_{BH}	L_{86}	411	0.98 ± 0.02	-0.003 ± 0.05	0.54 ± 0.90	0.77	0.87	0.89	1.89×10^{-137}
L_X	M_{BH}	L_{230}	492	0.98 ± 0.03	0.26 ± 0.06	-2.05 ± 1.10	1.34	0.78	0.88	2.12×10^{-153}
L_X	M_{BH}	L_{345}	393	0.81 ± 0.01	0.03 ± 0.06	8.26 ± 0.82	0.97	0.83	0.92	9.40×10^{-152}

Notes. Cols. (1)-(3): Independent (X, Y) and dependent (Z) variables, in log scale; Col. (4): Sample size; Cols. (5)-(11): Best-fit linear regression $2-10$ KeV hard X-ray luminosity coefficient (ξ_X), BH mass coefficient (ξ_M), y-axis intercept (β_0), intrinsic scatter (σ_{int}), adjusted coefficient of determination (R^2_{adj}), Spearman rank-order correlation coefficient (ρ) and associated p-value.

have been employed in previous FP studies (Merloni et al., 2003; Körding et al., 2006; Gültekin et al., 2009; Wong et al., 2016). This approach will help validate our conclusions, if both methods are consistent in their derivations.

As a sanity check, we first test our FP derivation methods with the data presented in Gültekin et al. (2009) and Ruffa et al. (2024). Both our methods give results which agree within the reported 1σ errors of the FP coefficients of these publications.

For our OLS regression method, we make use of the `OLS` function of the `statsmodel.api` Python library and perform MC sampling of the three quantities, which allow us to consider their measurement errors. Since the errors on SMBH mass and X-ray fluxes are often not symmetric, for each data point we use Gaussian prior distributions, whose mean is the measured or estimated value, and whose he upper/lower standard deviations are the asymmetric upper/lower limit errors. The prior for a given data point is thus obtained by stitching together two halves of two random normal distributions with the above characteristics. In each MC iteration, instead of using the measured values of mass, and radio and x-ray fluxes of each source, we randomly generate these values from the corresponding bi-Gaussian priors. Then, the OLS regression coefficients and model statistics are computed for the new vectors using the aforementioned Python function.

The above process was repeated 10 000 times so as to determine the median values and their errors of the fitted FP coefficients. As an example illustration, a corner plot of the resultant values for the 1 GHz sample are shown in Figure 3.3.1. The median values of the FP coefficients over these 10 000 runs are listed in Table 3.3.1 for all radio frequencies considered.

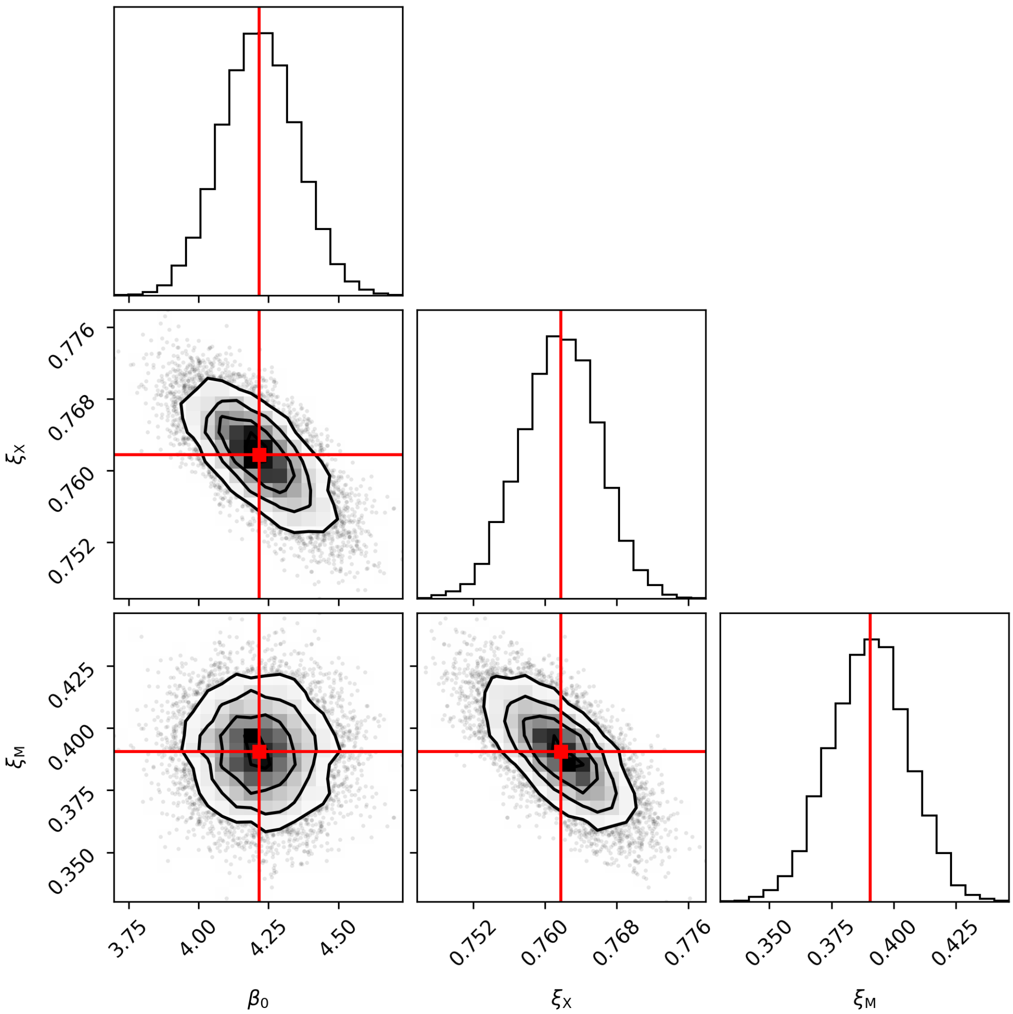

Figure 3.3.1: Corner plot of the distribution of best-fit parameters derived from an OLS multivariate linear regression between M_{BH}, L_R at 1 GHz, and L_X, with MC sampling, after 10 000 iterations. ξ_X and ξ_M, denote the weight of radio luminosity dependence on X-ray luminosity and BH mass, respectively, while β_0 represents the y-axis intercept value of the obtained L_R predictor function. Red squares highlight the median value of the distribution. Black contours contain 11.8%, 39.3%, 67.5% and 86.4% of the samples.

For the second method, we seek to derive the model coefficients that best fit the data by numerically minimizing a modified chi-squared statistic that directly considers coordinate errors into the derivation. This is known as the merit function (Fasano and Vio, 1988), and is of the form:

$$\tilde{\chi}^2 = \sum_i^N \frac{(R_i - R_0 - \xi_M \mu_i - \xi_X X_i)^2}{\sigma_{R,i}^2 + \xi_M^2 \sigma_{M,i}^2 + \xi_X^2 \sigma_{X,i}^2}, \tag{3.3.2}$$

where R_i, μ_i and X_i represent the log scale specific radio luminosity, BH mass, and specific $2-10$ KeV hard X-ray luminosity vectors, respectively, after being normalized to their median values (this will help decrease the error in the intercept term). The y-axis intercept is denoted as R_0, ξ_M and ξ_X depict the independent variable coefficients, with $\sigma_{R,i}$, $\sigma_{M,i}$, and $\sigma_{X,i}$ being the, assumed symmetric, measured errors of the three SMBH characteristics. In the case of the response variable (L_R), since the measured errors are the smallest we expect the variability in this direction to be dominated by the intrinsic scatter, therefore we assume a Gaussian error centered at 1 dex with a standard deviation of 0.2 dex, similar to the intrinsic scatter found along this axis by Gültekin et al. (2009).

The R_0 term, for which $\tilde{\chi}^2$ is the lowest, can be determined a priori as (Merloni et al., 2003):

$$R_{\min}(\xi) = \frac{\sum_i^N \left[(R_i - \xi_X X_i - \xi_M \mu_i) / \sigma_{R,i}^2 + (\xi_X \sigma_{X,i})^2 + (\xi_M \sigma_{M,i})^2 \right]}{\sum_i^N \left[\sigma_{R,i}^2 + (\xi_X \sigma_{X,i})^2 + (\xi_M \sigma_{M,i})^2 \right]^{-1}}. \tag{3.3.3}$$

Later, we calculate the corresponding $\tilde{\chi}^2$ value for a million different combinations between a thousand values of ξ_X and ξ_M, ranging from -0.5 to 2, and -0.7 to 1.8, respectively. Then, we estimate the intercept term for the non normalized relation as:

$$\beta_0 = R_0 + \log(\tilde{L}_R) - \xi_X \log(\tilde{L}_X) - \xi_M \log(\tilde{M}_{BH}), \tag{3.3.4}$$

where $\tilde{L}_R$, $\tilde{L}_X$, and $\tilde{M}_{BH}$ are the corresponding median values of each quantity. Lastly, we select the parameter set that minimizes Eq. (3.3.2), and estimate the associated 1σ errors as the standard deviation of the sample of coefficients with a $\tilde{\chi}^2$ difference above minimum of $\Delta\tilde{\chi}^2 <= 2.3$. This threshold corresponds to the critical value for a right-tailed chi-squared probability distribution with two degrees of freedom, which provides the 1σ (68.27%) confidence level. This is illustrated in Figure 3.3.2 for the 230 GHz sample, where the region of agreement within 3σ is accentuated.

The parameters obtained using this methodology, together with model statistics, are listed in Table 3.3.2, an edge-on view of the FP at the different frequencies is shown in Figure 3.3.3, and a 3D visualization of the relation for the 230 GHz sample, that highlights the distribution of sources with radio upper limits within the FP, is provided in Figure 3.3.4. We note that the fits were much better when assuming a normal

Table 3.3.2: Best-fit FP model parameters and statistics from merit function minimization for the complete ETHER-FP sample, at multiple frequencies.

X	Y	Z	N	ξ_X	ξ_M	β_0	σ_{int}	R^2_{adj}	ρ	p
(1)	(2)	(3)	(4)	(5)	(6)	(7)	(8)	(9)	(10)	(11)
L_X	M_{BH}	$L_{1.4}$	2502	0.76 ± 0.01	0.58 ± 0.02	2.89 ± 0.001	1.20	0.71	0.85	0.0
L_X	M_{BH}	$L_{2.2}$	738	0.90 ± 0.01	0.16 ± 0.03	0.59 ± 0.01	0.88	0.90	0.95	0.0
L_X	M_{BH}	$L_{4.8}$	2730	0.83 ± 0.01	0.43 ± 0.02	1.33 ± 0.002	1.05	0.79	0.89	0.0
L_X	M_{BH}	$L_{8.6}$	1021	0.95 ± 0.01	0.27 ± 0.03	-1.98 ± 0.008	1.01	0.85	0.93	0.0
L_X	M_{BH}	L_{15}	512	1.08 ± 0.02	0.28 ± 0.05	-7.41 ± 0.01	1.03	0.85	0.91	8.40×10^{-196}
L_X	M_{BH}	L_{23}	485	1.00 ± 0.02	0.54 ± 0.05	-5.81 ± 0.01	1.07	0.82	0.92	6.96×10^{-203}
L_X	M_{BH}	L_{43}	399	0.95 ± 0.02	-0.07 ± 0.06	2.05 ± 0.01	0.72	0.87	0.91	1.29×10^{-152}
L_X	M_{BH}	L_{86}	411	0.99 ± 0.02	0.06 ± 0.05	-0.65 ± 0.01	0.73	0.88	0.91	7.59×10^{-155}
L_X	M_{BH}	L_{230}	492	0.98 ± 0.02	0.32 ± 0.04	-2.59 ± 0.01	1.30	0.79	0.88	5.64×10^{-163}
L_X	M_{BH}	L_{345}	393	0.82 ± 0.02	0.07 ± 0.05	7.10 ± 0.02	0.94	0.84	0.92	4.23×10^{-166}

Notes. Cols. (1)-(3): Independent (X, Y) and dependent (Z) variables, in log scale; Col. (4): Sample size; Cols. (5)-(11): Best-fit linear regression $2-10$ KeV hard X-ray luminosity coefficient (ξ_X), BH mass coefficient (ξ_M), y-axis intercept (β_0), intrinsic scatter (σ_{int}), adjusted coefficient of determination (R^2_{adj}), Spearman rank-order correlation coefficient (ρ) and associated p-value.

error distribution for the dependent variable, instead of using the actual measured values.

Lastly, it is important to note that the FP parameters obtained from both methodologies generally exhibit agreement within a 1σ confidence level in most cases and, although there can be larger discrepancies observed along the BH mass coordinate, the differences in ξ_X remain minimal. Therefore, based on the expected theoretical values for the different components defined by Merloni et al. (2003), we consider that these variations are not substantial enough to significantly affect the overall interpretation of the results.

3.3.2 Mass predictor functions

Several studies have shown that the FP can also be used as a valid tool to estimate BH masses, specially in the absence of specific measurements required to employ more robust methods (Merloni et al., 2003; Gültekin et al., 2019; Bariuan et al., 2022). Encouraged by this, we rearranged Eq. (1.3.1) in order to obtain a mass predictor function of the form:

$$\log M_{BH} = \xi_{MX} \log L_X + \xi_{MR} \log L_R + \beta_M. \tag{3.3.5}$$

Following this, we make use of the multivariate OLS linear regression with MC sampling method, employed in the previous section, to obtain the best-fit coefficients for the BH mass predictor functions at multiple radio frequencies, using the total ETHER-FP sample. The best-fit parameters and model statistics derived from this analysis are listed on Table 3.3.3, where large scatters across the board and low adjusted coefficients of determination are observed. Additionally, 2D edge-on views of the different

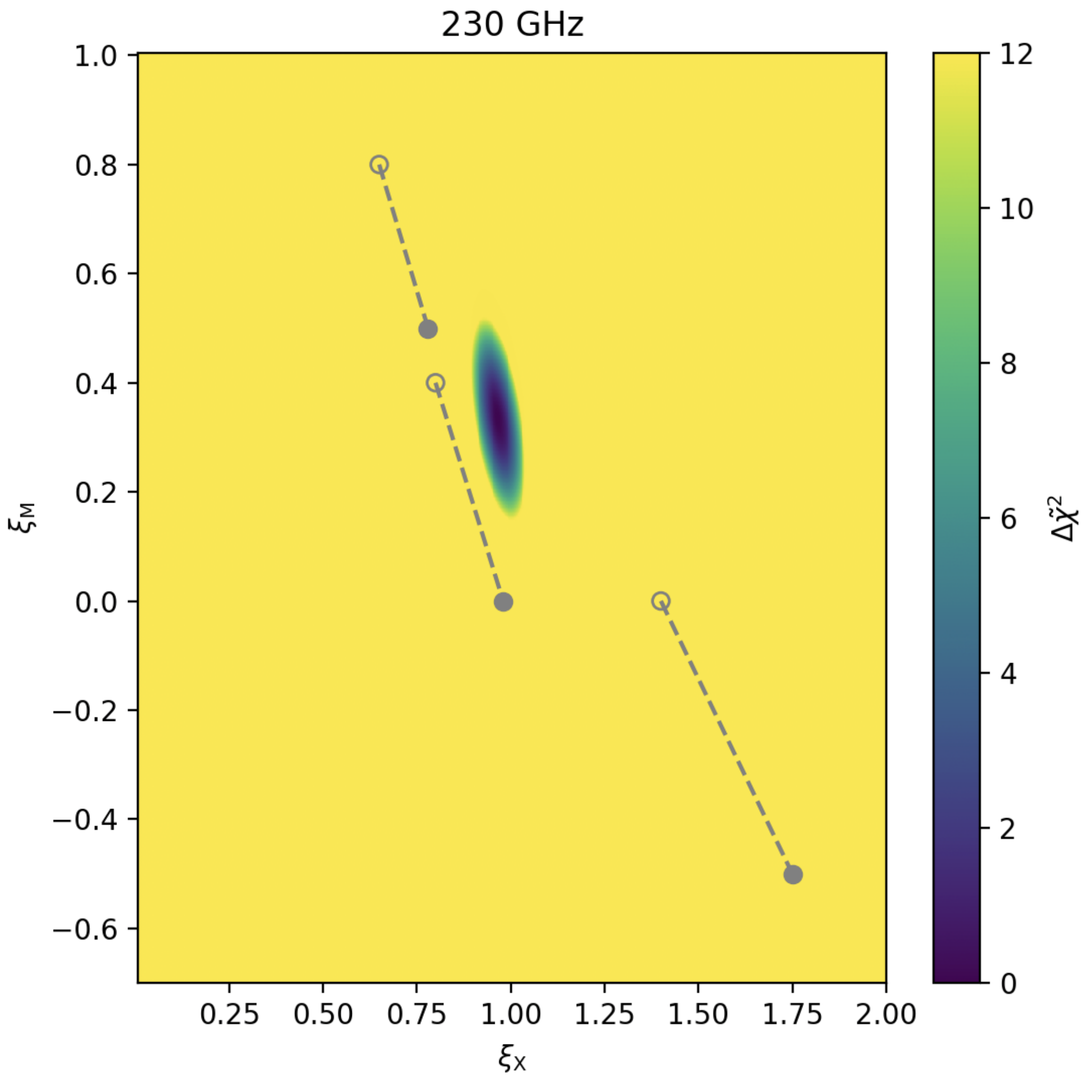

Figure 3.3.2: Merit function correlation coefficient distribution for the 230 GHz ETHER-FP sample. Dashed lines follow the theoretical predictions of Merloni et al. (2003) for ADAF (*top*), jet (*middle*) and disk (*bottom*) models, with tracks going from flat ($\alpha_R = 0$; Open circle) to steep ($\alpha_R = 0.5$; Filled circle) spectrum. Colored region denotes the distribution of modified chi-square differences above minimum. Regions of 1, 2, and 3σ confidence levels correspond to $\Delta\tilde{\chi}^2$ values less than their respective critical values within a χ^2 right-tail probability for two degrees of freedom (i.e., $\Delta\tilde{\chi}^2 \leq 2.3$, 6.18, and 11.83, respectively).

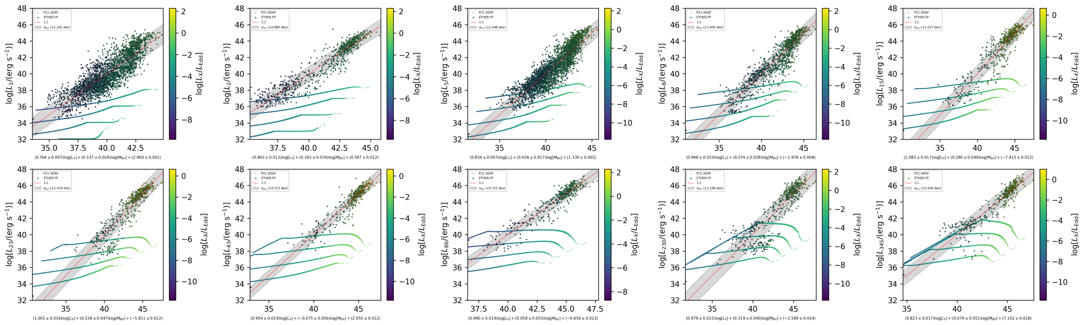

Figure 3.3.3: FP of BH activity derived from merit function minimization for the full ETHER-FP sample at multiple cm/sub-mm frequencies. *Top row*: From left to right the radio frequencies are 1.4, 2.2, 4.8, 8.6 and 15 GHz; *Bottom row*: From left to right the radio frequencies are 23, 43, 86, 230 and 345 GHz. Detections are presented as circles with black edges, while colored curves denote P21 ADAF SED model values for fixed BH masses of $\log[M_{\rm BH}/M_{\odot}] = 7$, 8, 9 and 10 (in ascending order) with Eddington ratio changing from $\log[L_{\rm X}/L_{\rm Edd}] = -7$ to -1.8 as it goes left to right. Marker color corresponds to the Eddington ratio, mapped following the bar at the side of each subplot. The red dashed line represents the best linear fit to the data, while the grey region highlights the range of intrinsic scatter within $\pm 1\sigma$.

FPs are illustrated in Figure 3.3.5, evidencing a potential bimodality driven apparently by differences in accretion state, which could explain the poor statistics obtained by fitting the model to the complete sample.

Discrepancies between FP correlation coefficients and model statistics derived from different subsamples (constrained by redshift, Eddington ratio, radio-loudness, AGN type, and galaxy morphology) for both the radio luminosity and mass predictor functions are discussed in more detail in Section 4.2.

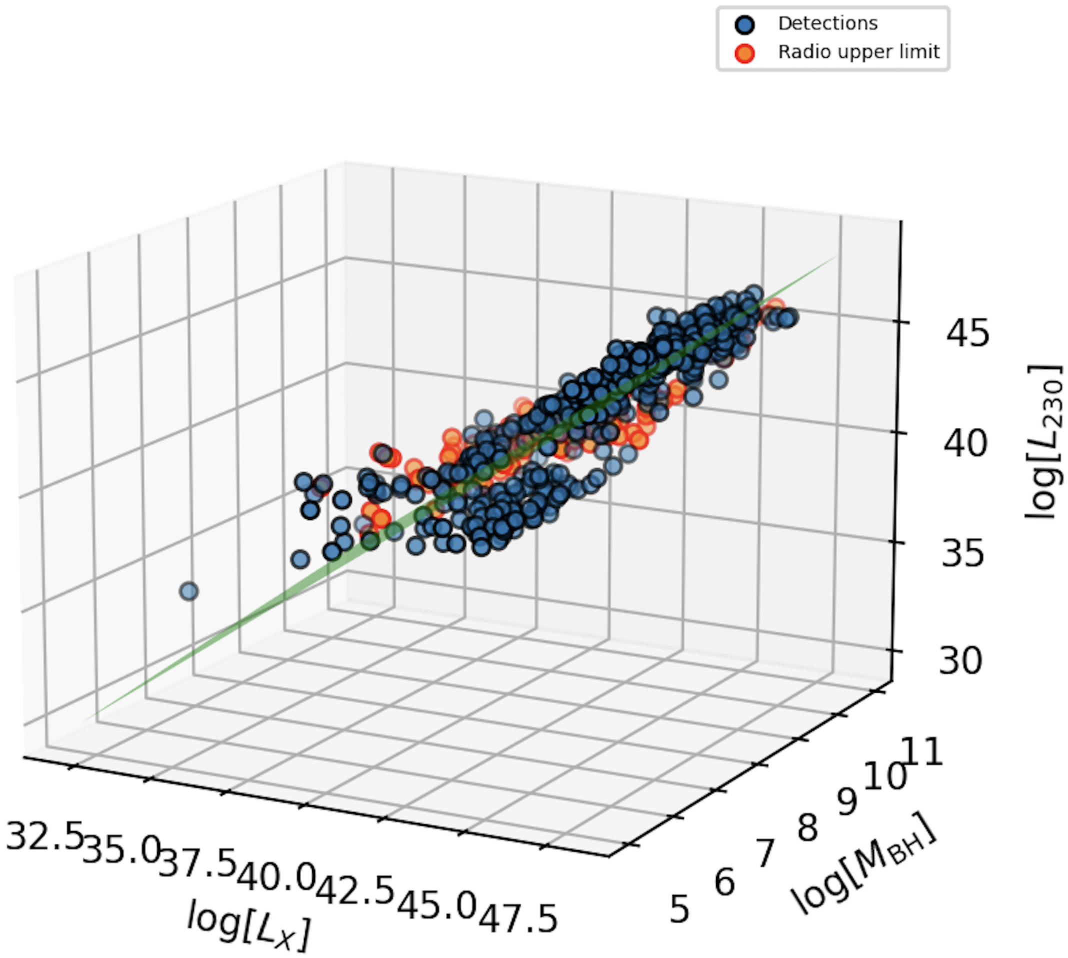

Figure 3.3.4: Three-dimensional view of the best-fit FP derived from merit function minimization at 230 GHz. The plane is shown in green, objects with detections in all three features are represented by blue circles, and sources with a radio upper limit (which were not considered in the FP derivation) are highlighted in red.

Table 3.3.3: SMBH mass predictor function coefficients and statistics from FP analysis of the complete ETHER-FP sample using multivariate OLS linear regression, at multiple frequencies.

X	Y	Z	N	ξ_{MX}	ξ_{MR}	β_M	σ_{int}	R^2_{adj}	ρ	p
(1)	(2)	(3)	(4)	(5)	(6)	(7)	(8)	(9)	(10)	(11)
L_X	$L_{1.4}$	M_{BH}	2502	-0.02 ± 0.01	0.21 ± 0.01	0.62 ± 0.36	0.91	0.19	0.47	1.42×10^{-133}
L_X	$L_{2.2}$	M_{BH}	738	0.06 ± 0.04	0.14 ± 0.04	-0.06 ± 0.55	0.93	0.26	0.50	8.70×10^{-46}
L_X	$L_{4.8}$	M_{BH}	2730	-0.03 ± 0.02	0.21 ± 0.02	1.21 ± 0.34	0.90	0.18	0.42	2.62×10^{-115}
L_X	$L_{8.6}$	M_{BH}	1021	-0.02 ± 0.03	0.17 ± 0.03	2.57 ± 0.50	0.88	0.16	0.33	3.37×10^{-26}
L_X	L_{15}	M_{BH}	512	0.05 ± 0.04	0.10 ± 0.03	2.23 ± 0.76	0.83	0.16	0.39	5.62×10^{-20}
L_X	L_{23}	M_{BH}	485	-0.10 ± 0.04	0.23 ± 0.03	3.34 ± 0.80	0.82	0.20	0.38	3.92×10^{-17}
L_X	L_{43}	M_{BH}	399	0.15 ± 0.05	-0.06 ± 0.05	4.85 ± 0.91	0.80	0.05	0.22	1.65×10^{-5}
L_X	L_{86}	M_{BH}	411	0.08 ± 0.06	-0.004 ± 0.06	5.33 ± 0.96	0.85	0.03	0.22	9.64×10^{-6}
L_X	L_{230}	M_{BH}	492	0.05 ± 0.04	0.13 ± 0.03	0.58 ± 0.78	0.95	0.21	0.45	3.37×10^{-25}
L_X	L_{345}	M_{BH}	393	0.18 ± 0.04	0.02 ± 0.04	-0.27 ± 0.80	0.84	0.27	0.50	1.13×10^{-25}

Notes. Cols. (1)-(3): Independent (X, Y) and dependent (Z) variables, in log scale; Col. (4): Sample size; Cols. (5)-(11): Best-fit linear regression $2-10$ KeV hard X-ray luminosity coefficient (ξ_{MX}), radio luminosity coefficient (ξ_{MR}), y-axis intercept (β_M), intrinsic scatter (σ_{int}), adjusted coefficient of determination (R^2_{adj}), Spearman rank-order correlation coefficient (ρ) and associated p-value.

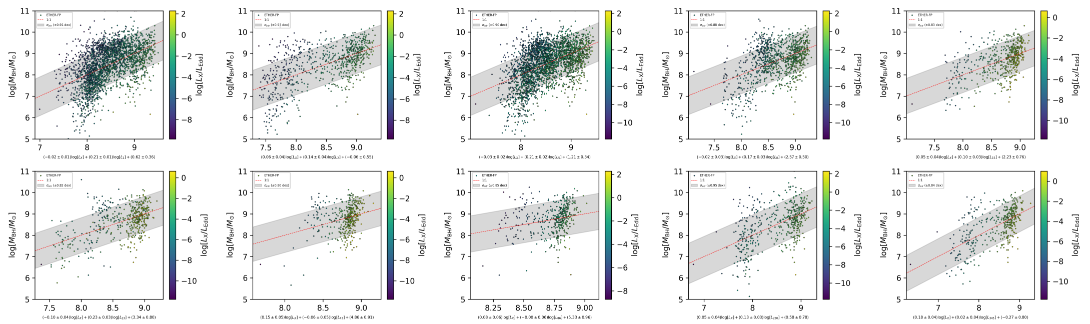

Figure 3.3.5: FP of BH activity derived from OLS linear regression to the full ETHER-FP sample, with $M_{\rm BH}$ as the response variable, at multiple frequencies. Data is presented as circles with black edges. Marker color corresponds to Eddington ratio, mapped following the bar at the side of each subplot. The red dashed line represents the best linear fit to the data, while the grey region highlights the range of intrinsic scatter within $\pm 1\sigma$. *Top row*: From left to right the radio frequencies are 1.4, 2.2, 4.8, 8.6 and 15 GHz; *Bottom row*: From left to right the radio frequencies are 23, 43, 86, 230 and 345 GHz.

Chapter 4

Discussion

4.1 Physical interpretation of the fundamental plane

4.1.1 ADAF SED modelling

P21 developed a physics updated, modified version of the formalism presented in Mahadevan (1997) regarding a semianalytical model of an ADAF around a SMBH. Here the main processes reproduced are flow equations of the accreting material, plasma heating and cooling, electron advection, and synchrotron, inverse Compton, and Bremsstrahlung radiation. Many of the model parameter values, like gas to magnetic pressure, viscous heating, size of the advection region, etc., are set to default values which accurately reproduce the emission profile of an M87-like ADAF, while the two most relevant parameters, BH mass and Eddington ratio, are left as free parameters for the user to choose. This allows us to easily tailor the model to the specific characteristics of each galaxy in ETHER and therefore test if our radio/X-ray correlation and FP results can be explained primarily by an ADAF component. This of course with certain caveats, since many of the model default parameters might not necessarily apply universally to all SMBHs. Additionally, due to issues with heating and cooling equilibrium above a critical accretion rate, the ADAF model can only be applied to Eddington ratios of $\log{(l_{\rm Edd})} \leq -2$. Above this Eddington ratio the system is no longer expected to be advection dominated (Mahadevan, 1997).

Since the P21 model is new and relatively untested on real data, we first discuss the results of this analytic model for a sub sample of objects for which more detailed ADAF numerical simulation fits were obtained by Bandyopadhyay et al. (2019, hereafter B19), based on the work of Yuan et al. (2005) and Spada et al. (2001). The latter method requires custom-fit 1D integrations of the ADAF, and thus are not feasible for samples of 100s to 1000s of targets. We find that the P21 model fits are in very good agreement, as can

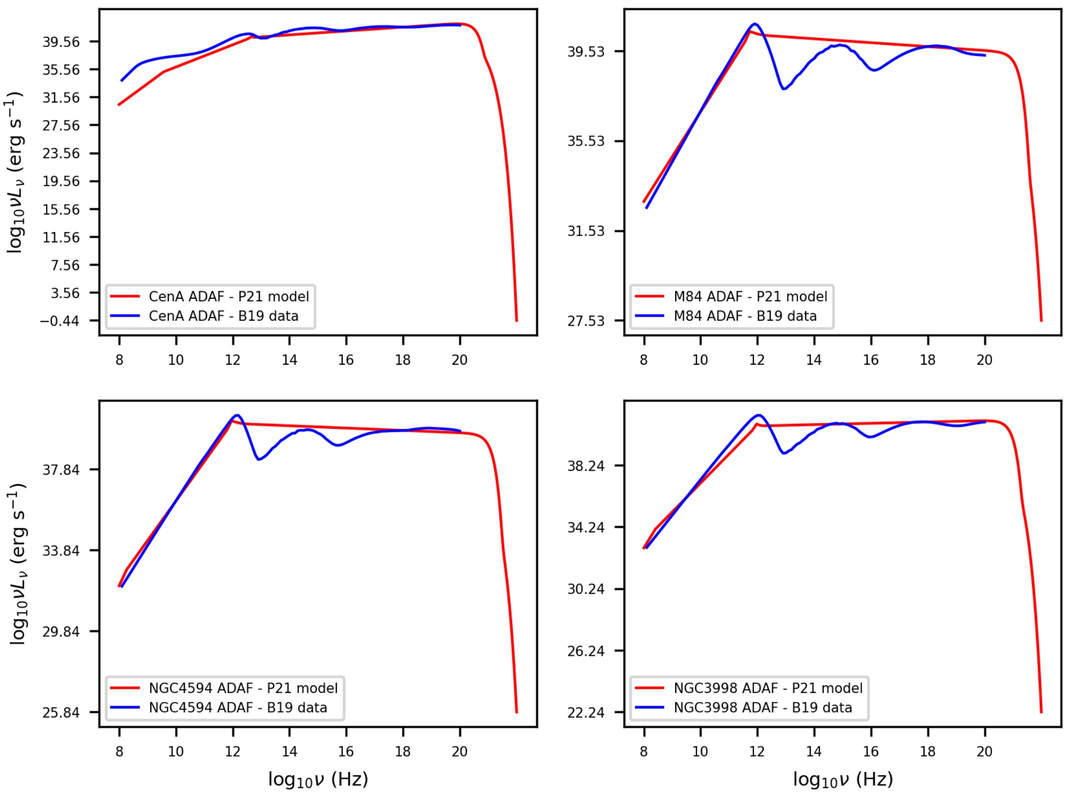

Figure 4.1.1: ADAF SED comparison between P21's semianalytic simulations (red curves) and B19's model data from thermal electrons (blue curves). All panels contemplate only thermal electron radiation, except in the case of CenA where contribution from non-thermal electrons is also considered in the case of B19's model. *Top left panel*: CenA. *Top right panel*: M84. *Bottom left panel*: NGC 4594. *Bottom right panel*: NGC 3998.

be noted in Figure 4.1.1. It can be seen that P21's ADAF SEDs do not reproduce the effect of multiple Compton scattering processes that lead to the oscillating behaviour at the far IR (FIR), optical, and UV regimes noticed in the more complex approach. Also, a significant difference in predicted luminosity arises in the low frequency regime, e.g., in the case of CenA, due to the contribution of synchrotron radiation from non-thermal electrons in the accretion inflow, that is considered in B19's approach. Still, these comparisons prove that the new analytical ADAF model is a robust tool for comparing mm/sub-mm wave radiation predictions to those at the hard X-ray, at least for sources in the tested subsample.

With this in mind, and assuming that most of the high energy radiation comes from an ADAF (Merloni et al., 2003; Yuan et al., 2005; Yuan and Cui, 2005; Yuan et al., 2009; Nemmen et al., 2014), for any source with a BH mass estimate, or measurement, and a $2-10$ KeV (hard) X-ray flux detection, we can use P21's model to derive the Eddington ratio value that best fits the hard X-ray flux detection. We achieve this by means of a recursive bisection fitting algorithm that iterates over a user specified Eddington ratio range starting from an initial guess taken as the mean between both limits, with a maximum allowed error of 1% between the model-predicted and observed X-ray luminosities. The Eddington ratio that leads to the best fit is then used as input, in conjunction with our BH mass, to derive the complete ADAF SED profile, and extract expected flux values at all relevant ETHER frequencies, converted following Eq. ((3.1.1)) from their respective rest-frame luminosities. One downside of this approach is that it can be very time consuming, especially for sources with high accretion rates: here, independent of the initial guess, the ADAF model SED will never reach the high observed X-ray luminosity and thus will not fulfill the accuracy constraint of agreement within 1% of the measurement. In this case, after iterating over the maximum number of allowed iterations (set to 30), the target is declared unfittable, and the algorithm passes to the next object.

Since ETHER is a very large sample, optimizing the SED fitting algorithm was key to both deriving the best fit Eddington ratio, and to estimating its errors (given the errors of the input quantities: SMBH mass and hard X-ray flux). To this end, we calculated SED templates for a million possible combinations of BH mass and Eddington ratio, with $\log(M_{\rm BH})$ ranging from 6 to 11, and $\log(l_{\rm Edd})$ from -7 to -1.8, with the remaining parameters kept as their default values. In a similar way to the OLS linear regression done to derive FP correlation coefficients described in Section 3.3, and in order to get an estimate of the variation in the predicted SED, for each source we first create a distribution of 1 000 different BH mass and X-ray luminosities with MC sampling from the distributions of the SMBH mass and hard X-ray luminosity (i.e., considering the errors in these values). These distributions interleave the lower and upper halves of two Gaussian priors centered on the measured value, each with one end of the asymmetric errors as its standard deviation.

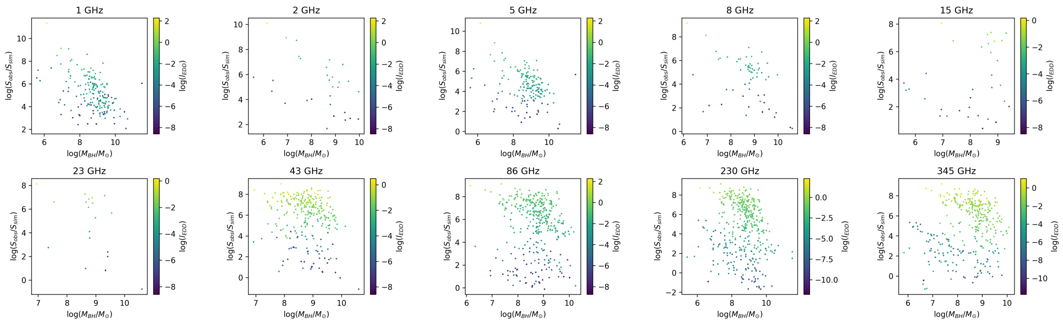

Figure 4.1.2: Flux ratio between observed and ADAF SED model prediction vs. BH mass for ETHER-FP, at multiple frequencies. Color bars denote Eddington ratio in log scale. *Top row*: From left to right each panel represents 1.4, 2.2, 4.8, 5.6 and 15 GHz radio emission, respectively; *Bottom row*: From left to right each panel represents 23, 43, 86, 230 and 345 GHz radio emission, respectively.

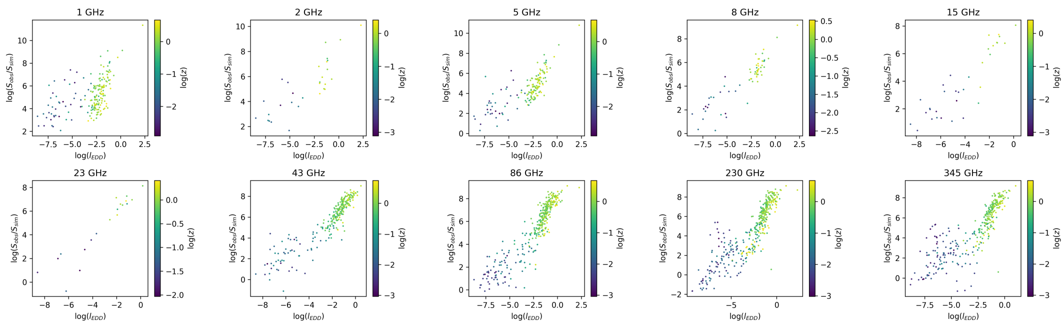

Figure 4.1.3: As in Figure 4.1.2, but now the x-axis and color bar follow Eddington ratio and redshift, respectively.

Then, to obtain the final predicted radio flux at any observed radio frequency ν, and the corresponding Eddington ratio for each pair of input parameter values, we select the template closest to the input (MC) BH mass and X-ray value. We then convert rest-frame luminosity at $\nu_{\rm obs}(1+z)$ to observed-frame flux using Eq. (3.1.1). The median value of 1 000 values in the resulting distribution is used as the flux prediction, with lower and upper errors calculated as the RMSE of the first and second halves of the sorted array, respectively.

The ratio of ADAF-predicted to observed radio flux reveals systematic trends (see Figures 4.1.2 and 4.1.3). Effectively, the observed to predicted flux ratio is close to 1 for M87-like galaxies at mm-wave frequencies, but it can be noted that as the BH mass decreases, and the Eddington ratio increases, the fraction between observed and predicted flux increases significantly (up to $\sim$ 8 dex for high redshift sources and $\sim$ 6 dex for nearby ones), possibly suggesting that the observed fluxes of the lower mass and/or higher Eddington ratio systems are from mechanisms other than an ADAF, e.g., emission from jets, corona, dust in the host galaxy, etc. (Merloni et al., 2003; Gallo et al., 2003; Falcke et al., 2004; Körding et al., 2006; Gültekin et al., 2009; Yuan et al., 2009; Nemmen et al., 2014; Wong et al., 2016; Bandyopadhyay et al., 2019; Ramakrishnan et al., 2023; Ruffa et al., 2024). This scenario is supported

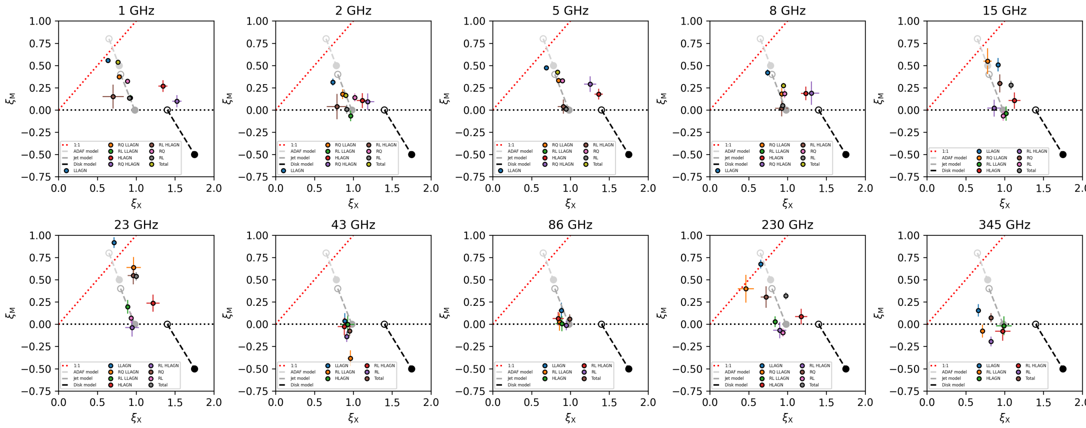

Figure 4.1.4: Comparison of X-ray luminosity (ξ_X) and M_{BH} (ξ_M) best-fit correlation coefficients for the FP at multiple radio frequencies, derived from Merit function minimization, for the total sample and different combinations of radio-loudness (between $\log R_X \leq -2$ for RQ and $\log R_X > -2$ for RL) and Eddington ratio (between $\log l_{Edd} \leq -2$ for LLAGN and $\log l_{Edd} > -2$ for HLAGN) subsamples. Solid red and black lines represent equal weight between both variables, and no mass contribution to radio luminosity, respectively. Dashed lines represent theoretical predictions from Merloni et al. (2003) at 5 GHz, with open circles indicating a flat spectral index ($\alpha_R = 0$, and solid circles a steep slope of $\alpha_R = 0.5$). Coefficients derived from samples with less than 30 objects have been omitted due to high uncertainty. Errors are presented within 1σ confidence level.

by the observed distribution of our own FP coefficients, as shown in Figure 4.1.4 and 4.1.5, where the parameters of the LLAGN and low redshift (i.e., $z \leq 0.05$) subsamples are more in line with the expected theoretical values from steep spectrum ADAFs, jets, or possibly a combination of the two.

The systematic offset in the observed to predicted flux ratio could also be a consequence of issues within the model itself such as, for instance, an erroneous scaling of thermal synchrotron emission as BH and Eddington ratio are varied. Certainly, the bimodality (between low and high redshift sources) and the systematic linear patterns observed in the comparisons, might be correctable if the default value

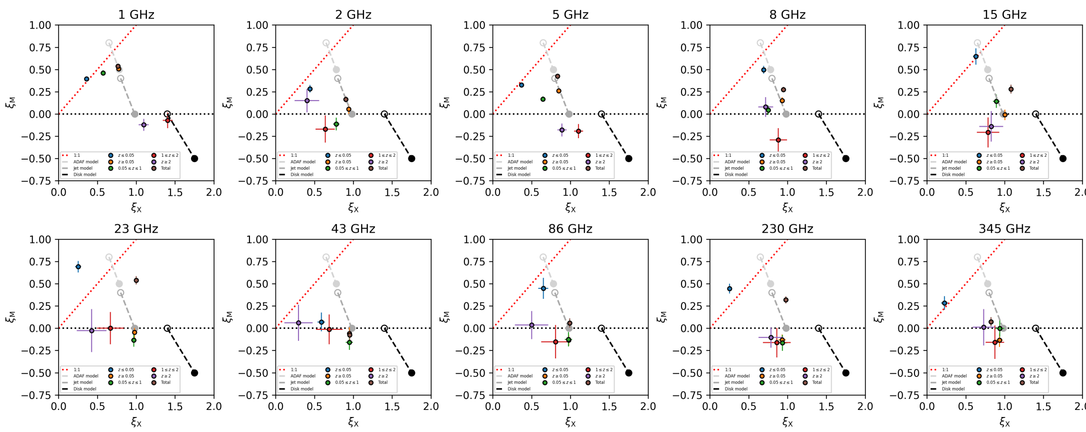

Figure 4.1.5: As in Figure 4.1.4, but separated by redshift range for the total sample.

parameters of the P21 model were to be adjusted to compensate for the lack of non-thermal synchrotron radiation, or scaling factors were applied. However, the resulting changes require to be significantly large to cover the complete spectrum of luminosities observed, if one wishes to describe all types of SMBHs with just an ADAF. In this context, one must be cautious when altering the model parameters to avoid facing unphysical scenarios. A comprehensive study of the effects and evaluation of the theoretical validity of altering P21's ADAF SED model parameters on the predicted radio emission from thermal electrons is out of the scope of this thesis. However, a quick exploration of the parameters (each described in Table 3 of Pesce et al., 2021) shows that variables such as the viscosity parameter (α), the ratio of gas pressure to magnetic pressure (β), the power-law index for the mass accretion rate as a function of radius (`s`), the SMBH shadow detection threshold (`rtresh`), the minimum dimensionless radius of the advection region (`rmin`), and the fraction of viscous heating that goes directly to the electrons (δ) can significantly impact the radio flux profile (i.e., change by at least an order of magnitude per parameter). Further testing is required to determine the physical validity and explanation for some of these parameters taking on distinct values, and to ascertain if altering them would effectively make the ADAF SED capable of describing our observations.

Figures 3.2.1 and 3.3.3 show that observed radio luminosities are, in most cases, orders of magnitude above what the ADAF component by itself can produce, as expected from the observed vs predicted flux comparisons. Interestingly, the ADAF luminosity distributions in both the radio/X-ray correlation and FP spaces could appear similar at first hand to that of the data, which should lead to a good agreement with the LLAGN sample if the ADAF radio emission were to be scaled by ~ 1 dex. This exercise was done recently by Ruffa et al. (2024) using the same ADAF model, for a relatively small number of nearby SMBHs at 1 mm, where they offset the model grid of luminosities by 0.5 dex in BH mass, obtaining consistent results with our 230 GHz sample.

However, even if an object sits within the ADAF predicted radio luminosity distribution, its uncertain that this component by itself could accurately reproduce the observed spectra. This is supported by Figures 4.1.2 and 4.1.3, showing that the ADAF-only approach works best for high $M_{\rm BH}$ and low $l_{\rm Edd}$ sources. Additionally, it is important to point that we do not currently have reliable radio spectral indices or shapes for our targets. Thus, while the ADAF model results can be K-corrected, the observed data can not, potentially introducing considerable systematic error at higher redshifts.

In summary, our results indicate that while the ADAF model predicted radio luminosities can match the observations of LLAGN, there are significant discrepancies between the observed and simulated distributions of BH mass and Eddington ratio. These differences lead to substantial inconsistencies between the observed flux values and the predictions from thermal electron emission within an ADAF.

This suggests that the ADAF is likely not the only component in these systems, as evidenced by comparisons with theoretical FP correlation coefficients. Therefore, one should be cautious when assuming flux predictions from this model as the total emission, with the current set of default parameter values, specially when probing the viability of VLBI observations for sources in ETHER, and should only be considered as a lower limit.

4.1.2 ADAF+jet SED modelling

Considering that the ADAF SED model from P21 fails to accurately predict the measured radio fluxes for sources in our sample, it becomes necessary to include additional components, such as a compact jet, to achieve a faithful reproduction of the complete SED for a significant number of objects in ETHER.

In this context, Spada et al. (2001) derived a highly detailed theoretical jet SED model for AGN, under an internal shock scenario (i.e., shocks due to material at different velocities within the jet). This jet model, together with a numerical ADAF model, was used by B19 to describe the thermal and non-thermal parts of a jet spectrum, compare the results with multi-frequency measurements, and predict whether the accretion inflow of five sources (CenA, M84, M87, NGC4594, NGC3998) could be resolved using the EHT or GMVA. They showed that the combined spectrum from thermal electrons within an ADAF and a jet resulted in very good agreement with the data. More recently, Ruffa et al. (2024) tested whether the variations seen in the radio/X-ray correlation at 1 mm could be explained by a compact jet model viewed at different inclination angles, finding good agreement between the model and the radio/X-ray ratios for nearby LLAGN.

Given this, we decided to combine P21's semianalytic thermal ADAF SED model with the phenomenological jet model of Spada et al. (2001), so as to fit the observed SED with a superposition of both components. Since, for the large number of ETHER sources, we are unable to directly measure many of the system properties required as input model parameters, we initially tested how the inclusion of an M87-like jet together with an ADAF, fitted to an X-ray measurement, would be able to fit the radio photometry for the 5 sources modelled in B19's. The results of this can be seen in Figure 4.1.6 and 4.1.7, where we normalized the M87 jet model to each target's 5 GHz luminosity, showing decent agreement with the measurements, except in the case of the radio galaxy CenA.

Nonetheless, the assumption that all jets are similar to that of M87 is quite big given the number of adjustable parameters within the jet model, and the wide variety of jets observed in nature (See section 1.2.3). Therefore, we conducted a study to investigate the impact of parameter variations in the jet SED model. Specifically, we systematically fixed one of the 14 parameters while varying the others across a range of values. This approach aims to identify the most influential parameters and potentially

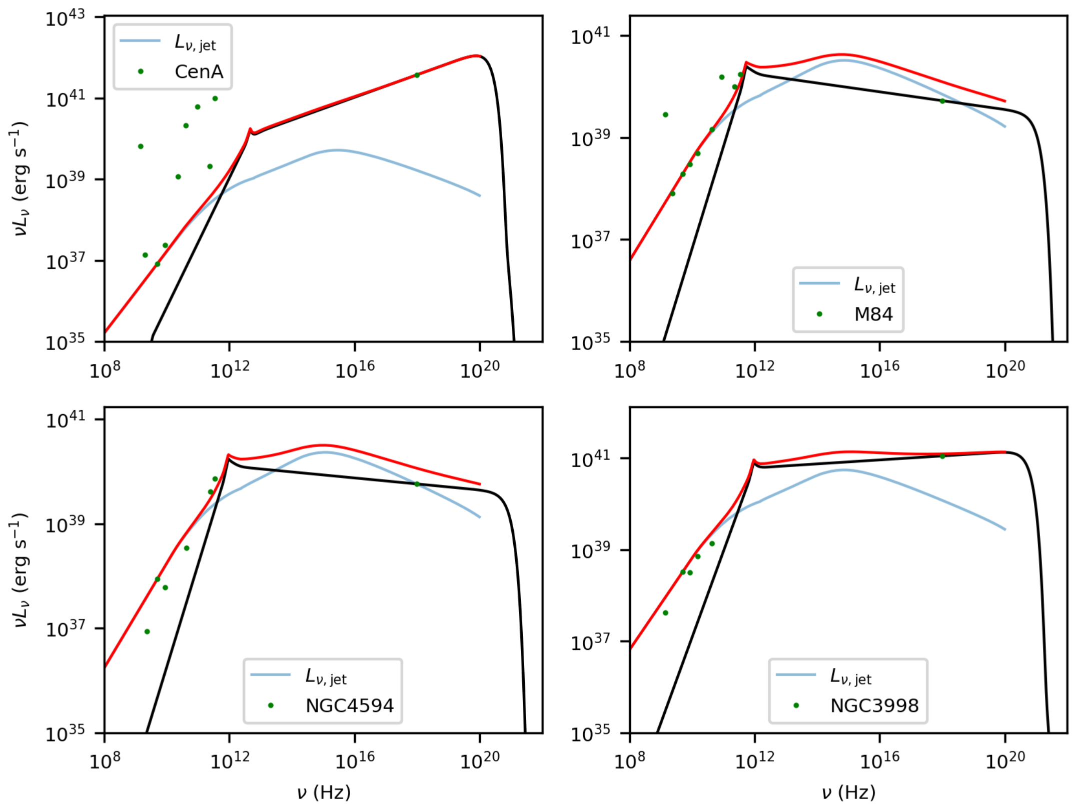

Figure 4.1.6: Total SED (red curve) model fits to science objects in B19, as a superposition of a standard M87-like compact jet (blue curve) scaled to a 5 GHz flux data point, and an ADAF emission profile (black curve). Green circles denote direct measurements at multiple frequencies. *Top left panel*: CenA; *Top right panel*: M84; *Bottom left panel*: NGC 4594; *Bottom right panel*: NGC 3998.

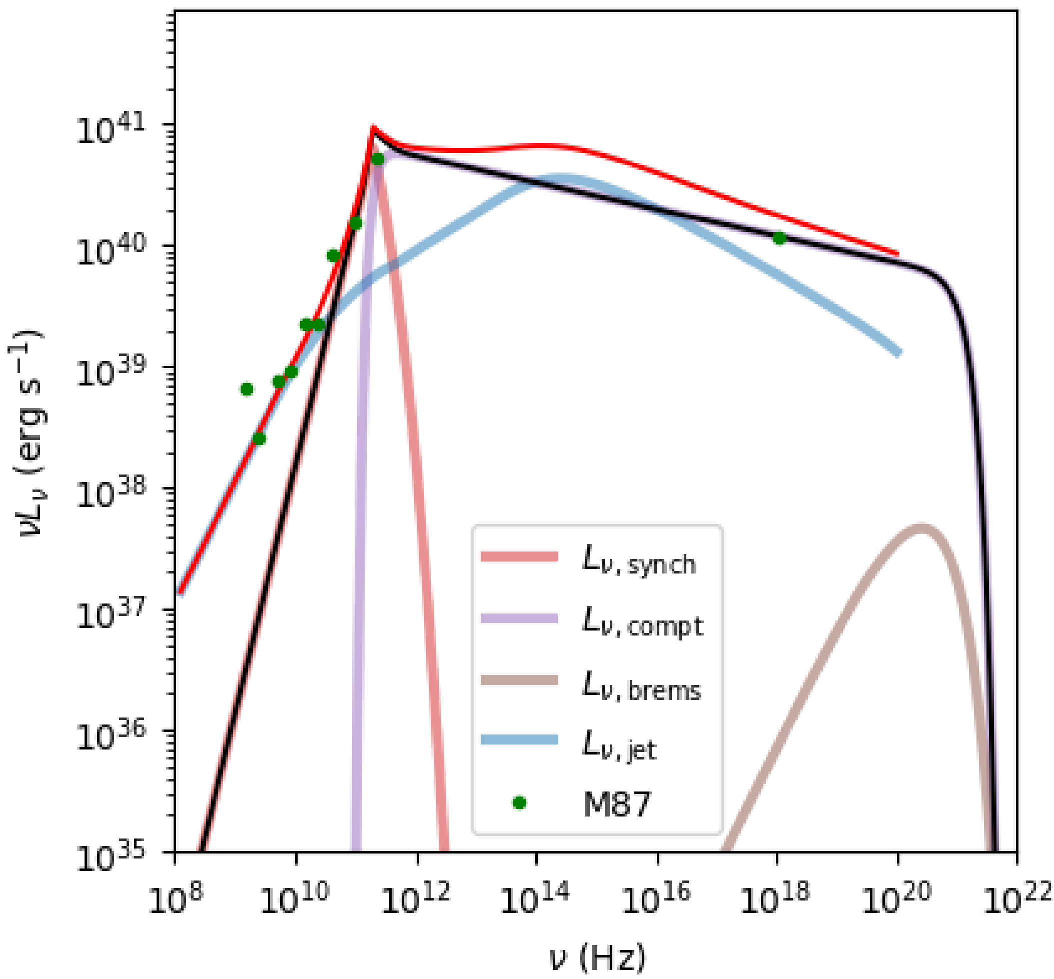

Figure 4.1.7: M87 ADAF (black curve) plus jet (blue curve) total SED (red curve) model from the superposition of a scaled (to 5 GHz flux detection) jet and ADAF component. Green dots represent multi-wavelength measurements. Orange, purple and brown curves denote ADAF synchrotron, inverse Compton, and Bremsstrahlung radiation, respectively.

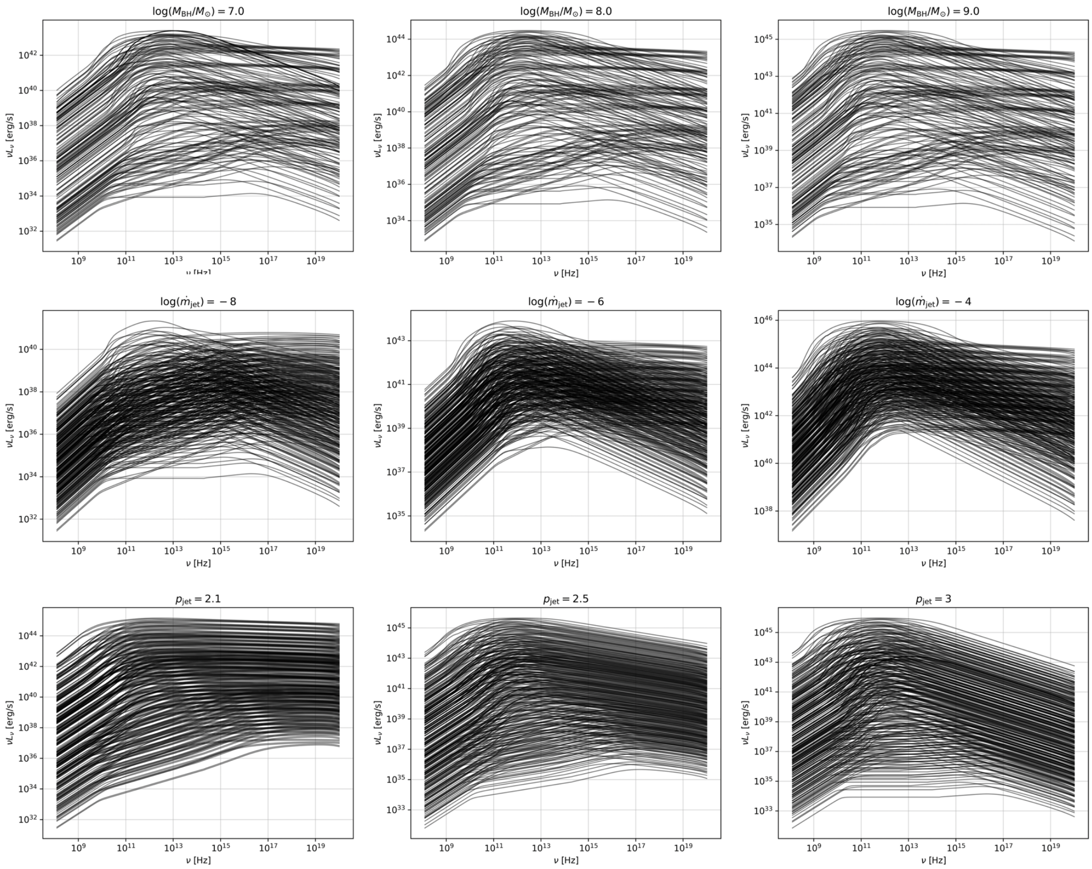

Figure 4.1.8: Jet SED model parameter study for three of the main variables that affected the SED significantly. BH mass (*top*), jet outflow rate (*middle*), and jet power-law index (*bottom*), are shown for three distinct values in increasing order from left to right. The variations within fixed values correspond to changes in the remaining model parameters.

reduce their number in the model. In Figure 4.1.8 we illustrate the effects of varying three of the four parameters which most significantly changed the predicted SED of the model. Both the mass of the central compact object and the jet outflow rate not only act as scaling factors but also influence a decrease in peak frequency with increasing $M_{\rm BH}$ and a steepening of the radio spectral index at higher $\dot{m}_{\rm jet}$. On the other hand, we note that the power-law index heavily influences radio-loudness. Moreover, the jet view angle can significantly increase both radio and X-ray luminosities by several orders of magnitude, peaking at the highest values near the LOS, while also having an influence on the radio spectral slope. Effectively, this means that we can limit ourselves to only iterating over these four parameters to obtain reasonable valid fits to data.

To this end, we generate several templates of the jet SED model from all the possible combinations between the relevant parameters over a broad space of values, aiming to efficiently calculate the total ADAF+jet SED for all objects in ETHER. Similarly to what we did with the ADAF model, we first select a subset of potential best-fit templates based on the closest BH mass to that of the selected object.

Each potential jet is then individually scaled to a 5 GHz VLBI measurement (i.e., we assume that the emission at this range is predominantly from the jet), if available, or else to the closest detected radio flux. If the predicted hard X-ray luminosity of the current template is larger than the measured value, it is automatically discarded, otherwise we account for the difference between the total and jet luminosities by fitting an ADAF component using our bisection algorithm (implementing the ADAF template fitting into this pipeline would significantly improve execution speed, but is left for the future). The total SED is then calculated as the superposition of the predicted spectra from the jet and accretion inflow. We repeat this process for all the jet templates in the initial subset, and calculate a RMSE value to each of them as a measure of goodness of fit. The model with the lowest RMSE is then determined as the final prediction, with expected ADAF, jet, and total fluxes at ETHER radio frequencies being properly converted from their rest-frame luminosities.

The improvements in the SED fitting process thanks to the inclusion of the jet component are illustrated in Figure 4.1.9, for four different ETHER sources. While preliminary results from simulations performed to objects in the ETHER "Gold sample" (Ramakrishnan et al., 2023) suggest that the observed agreement between measurements and predictions from the ADAF+jet SEDs is better as opposed to using an ADAF model only, we note that in the current state of our implementation, the contribution from individual components and their dominance over distinct frequency ranges is heavily dependent on the adopted jet template, so additional constrains when performing the simulations should be considered to account for this uncertainty. In this case, for instance, we suggest evaluating the position of an object within the FP beforehand to know what mechanisms are likely to dominate the emission at distinct frequencies, and then apply proper restrictions before running the composite model fits. We note that the accuracy of the fit is also affected by the non-simultaneity and varying resolution of the measurements, as well as the number of flux measurements at multiple radio frequencies. Simultaneous multi-wavelength high resolution flux measurements are highly desirable to increase the reliability and scope of the results.

Overall, considering both the improvements in SED fitting thanks to the inclusion of radiation from the outflow, and the observed correlation coefficient distributions from the FP derivations, it appears highly likely that jets in combination with ADAFs, are frequently present in LLAGN, and that their contributions to the continuum spectrum are significant. The extent in which the radio emission is driven by the coupling between accretion inflow and jets could be evaluated by extensively comparing the expected vs predicted fluxes from an ADAF+jet model for a large sample, and assessing its distribution within the radio/X-ray correlation or the FP, i.e., an exercise similar to that we have performed with the ADAF only model, although this exercise is out of the scope of this study. For now, it is best to assume an ADAF+jet model to test whether current, or future, VLBI instruments could detect and resolve the jets and accretion inflow of nearby LLAGN.

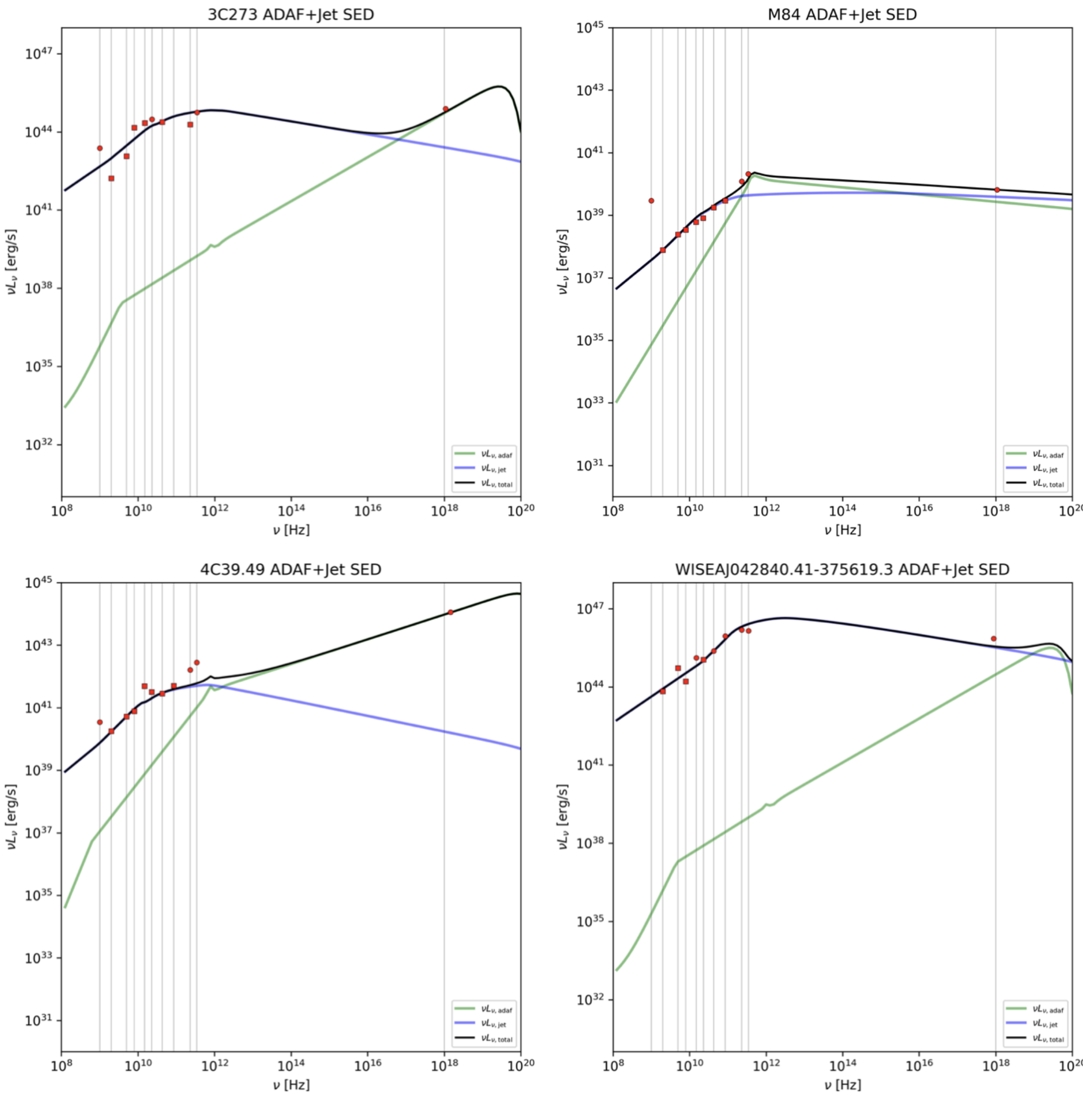

Figure 4.1.9: ADAF+jet SED model fitting results for four different ETHER sources. Green curve represents the thermal ADAF component from P21's model. Blue curve denotes the best-fit jet SED template from Spada et al. (2001) phenomenological model. Black line corresponds to the total luminosity profile as a superposition of both components. Red squares and circles highlight VLBI and lower resolution measurements, respectively. Grey vertical lines reference the main ETHER-FP cm/sub-mm and 2-10 KeV hard X-ray mid band frequencies.

4.2 Diversity between ETHER-FP subsamples

In conjunction with the global-ETHER FP results listed in Table 3.3.2, we have derived several additional radio luminosity predictors following the merit function minimization routine described in Section 3.3.1, for different subsamples within ETHER-FP. These subsets are selected by AGN type, galaxy morphology, redshift, and combinations of low ($\log l_{\rm Edd} \leq -2$) and high ($\log l_{\rm Edd} > -2$) Eddington ratio sources with inverted ($\log[L_{\rm R}/L_{\rm X}] \leq -2$) or relatively flat ($\log[L_{\rm R}/L_{\rm X}] > -2$) spectra. This categorization enabled us to identify potential discrepancies between best-fit FP coefficients due to sample biases, and analyze the variations of the derived parameters from cm to sub-mm wavelengths. Additionally, we can attain a preliminary idea of the dominant emission mechanism in each subset of objects by comparing our FP results with theoretically expected values for an ADAF, jet, and disk (Merloni et al., 2003).

Comparisons between FP correlation coefficients derived for different AGN types (See Figure 4.2.1) show that each of them follow a distinct plane. As expected, these results are consistent with those derived from objects within specific redshift bins (See Figure 4.1.5), since each interval is dominated by SMBHs with a specific type of activity that differs at each range, as seen in Figure 3.2.2. An evolution with redshift was also discerned within subsamples of the same AGN type, a behaviour we note is consistent with the findings of Bariuan et al. (2022) for a sample of RQ and RL QSOs. Discrepancies between FP parameters are also observed when grouping sources according to their host galaxy morphology (See Figure 4.2.2), Eddington ratio, and/or radio-loudness (See Figure 4.1.4). The diversity of observed parameters is in agreement with previous findings from numerous FP studies that have used different samples, and yielded contrasting results between them (Merloni et al., 2003; Körding et al., 2006; Wang et al., 2006; Gültekin et al., 2009; Plotkin et al., 2012; Gültekin et al., 2014, 2022; Bariuan et al., 2022; Ruffa et al., 2024). This further motivates the requirement to employ FPs tailored to specific samples in order to obtain accurate radio luminosity estimates.

The fact that X-ray luminosity and BH mass relate to radio luminosity differently across radio frequencies within the same type of object can be understood as consequence of a shift in preferred emission mechanism along the radio regime, if we follow the expected distribution of correlation coefficients for accretion inflow and outflow derived from the theoretical models of Merloni et al. (2003). Therefore, FPs regressions at multiple frequencies could provide crucial insights into how to effectively combine SED models for flux predictions.

The absence of theoretical predictions for FP correlation coefficients in combined accretion-jet models, like those considering different radio spectral slopes for ADAF, jet, and disk as derived by Merloni et al. (2003), complicates the identification of the dominant emission mechanism. In this scenario, a

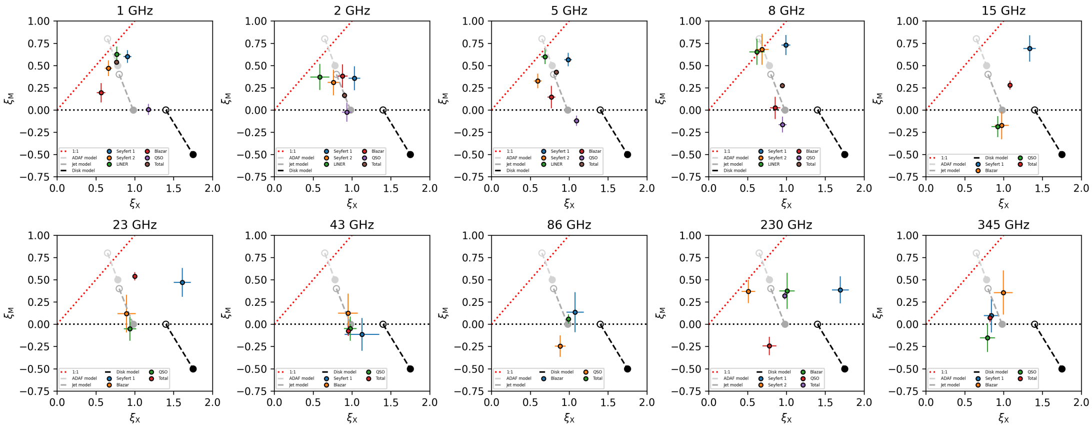

Figure 4.2.1: As in Figure 4.1.4, but separated by AGN type.

comprehensive study of the expected distribution of correlation coefficients derived from several different configurations of combined accretion-jet models could help constrain the contribution of each component to the total radio and X-ray luminosity, and provide information as to how ADAF, jet, and/or disk SED models should be used together when attempting to fit observational data at multiple cm/sub-mm frequencies.

Following this, supported by the differences observed between our data and ADAF-predicted fluxes, we propose that the radio luminosity profile of nearby LLAGN with Seyfert 2 or LINER activity could be reasonably reproduced by a combined ADAF+jet model. In this model, the ADAF component should follow a thermal spectrum that dominates from mm to X-ray wavelengths, while the jet contributes significantly at the cm region. In contrast, at larger redshifts (i.e., $z > 0.05$), and supported by the obtained results for the QSO sample, we expect the jet to dominate the total emission, with a disk potentially contributing to the radiation at X-ray wavelengths.

As a final note, the use of the FP relation as a radio luminosity estimator is encouraged over the direct radio/X-ray correlation, as it provides less intrinsic scatter overall. However, in the absence of accurate mass estimates, the latter remains a useful tool, primarily at larger distances where other methods may be less reliable.

With regard to the mass predictor function, and motivated by the behaviour observed in Figure 3.3.5, we note that by dividing the sample into low ($\log l_{\rm Edd} \leq -2$) and high ($\log l_{\rm Edd} > -2$) Eddington ratio objects, we achieve significant improvements to the tightness of the correlation across all frequencies. In the case of the latter, a mean intrinsic scatter of 0.76 dex is obtained, while the former presents a mean RMSE of 0.85 dex, similar to that of the total sample ($\bar{\sigma}_{\rm int} = 0.87$ dex).

A similar trend of two sequences is evidenced in redshift space as well (see Figure 4.2.3) between nearby

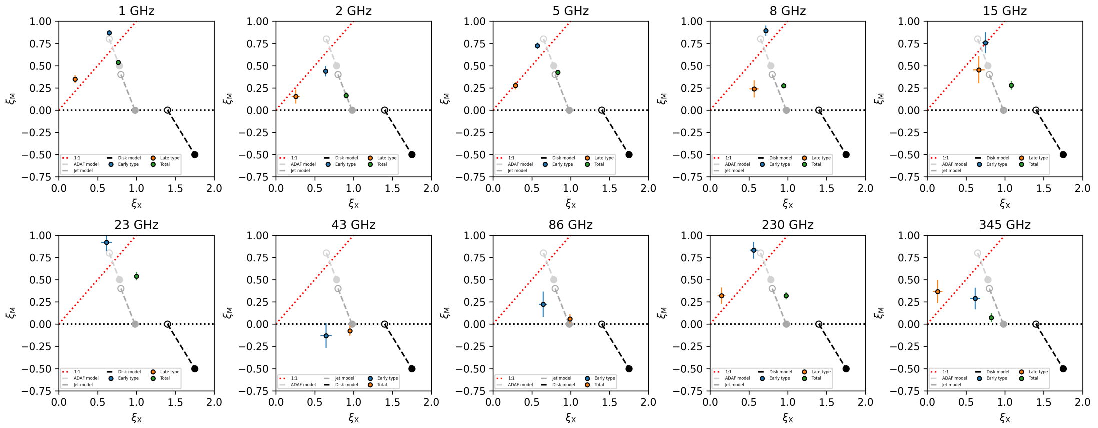

Figure 4.2.2: As in Figure 4.1.4, but separated by galaxy morphology between early-type ($-5 \leq \mathrm{T} \leq -1$) and late-type ($0 \leq \mathrm{T} \leq 8$).

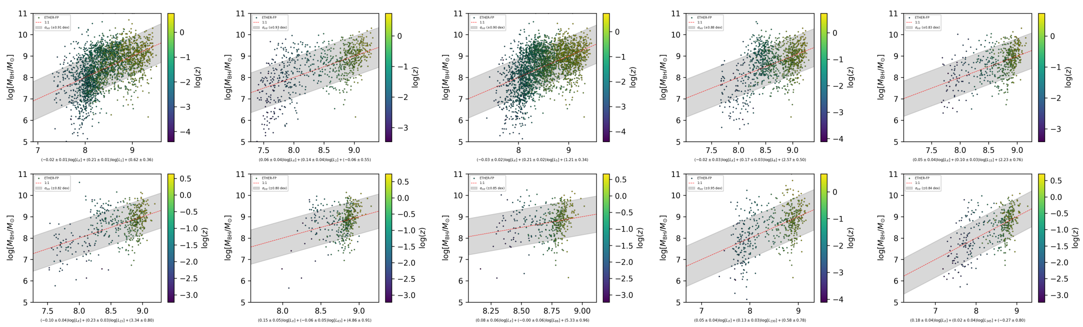

Figure 4.2.3: As in Figure 3.3.5, but this time following a redshift color bar, in log scale.

($z \leq 0.05$) and distant ($z > 0.05$) sources, with a decrease of the mean scatter from 0.94 dex to 0.82 dex with increasing distance, respectively.

These results align with Gültekin et al. (2009), who found that the scatter in the relation decreases notably when focusing on highly massive or unobscured objects, as is the case for our H/S state or high-redshift samples that include more massive sources compared to their counterparts. However, we propose that this reduction could be influenced by the narrower dynamic range of BH masses in these samples.

Since accuracy loss is present in BH mass estimates from standard spectroscopic modelling techniques (i.e., scalings based on reverberation mapping) at higher redshifts (Bariuan et al., 2022), these findings further validate the use of the FP as a reliable estimator at larger distances. Despite that, this scenario contrast with the recent finding of Bariuan et al. (2022) about redshift invariance in the accuracy of mass predictions within their FP mass estimator derived from a sample of 353 quasars.

Nevertheless, while the physical reason behind the apparent tightening of the correlation at higher redshifts remains a topic of discussion, we acknowledge that a proper comparison between the predicted mass estimates from our models and high-quality direct measurements would be highly beneficial for thoroughly assessing the strength of our mass predictor functions. However, such an analysis is beyond the scope of this thesis.

Chapter 5

Conclusion

The unprecedented sensitivities and resolutions achieved in mm VLBI, most specifically with the GMVA and EHT, have enabled the resolution of the innermost 100s of gravitational radii around SMBHs, and thus a new era of BH imaging and research. This motivated the need to build a comprehensive compilation of AGN-hosting galaxies which are bright and compact at mm and sub-mm wavelengths. Selecting the optimal subsamples of these for observations with the EHT and GMVA will significantly enhance our theoretical understanding of SMBHs properties. The ETHER sample, while still under active development, now represents the largest catalogue of known SMBHs to date.

The extensive nature of the ETHER sample presents a unique opportunity to revisit the strong empirical correlation observed between the radio and hard X-ray luminosities of AGN, as well as its unification from stellar to SMBHs in the form of the FP of BH activity. By leveraging the large statistics and variety of objects within ETHER, we could address some of the limitations faced by previous studies in this field. This allowed us to derive new relations across multiple radio frequencies, highlight and quantify the effects of biased samples, evaluate the utility of these relations as predictors of radio luminosity and mass in diverse scenarios, and improve SED model fitting techniques through a better understanding of the physical mechanisms governing AGN radio emission, among other advancements.

As a first step of this thesis, we enriched the ETHER sample by integrating additional photometric data from various radio and X-ray surveys such as the CSC, eRASS1, VLASS, and FIRST catalogues, as well as data from crossmatches via automated queries to large databases (SDSS, SIMBAD, and NED). This effort provided information for a large number of sources including host galaxy morphology, AGN type, distance, redshift, and photometry ranging from cm to sub-mm wavelengths (specifically at 1.4, 2.2, 4.8, 8.6, 15, 23, 43, 86, 230, and 345 GHz), together with fluxes in the hard X-ray band.

With an updated ETHER, we selected a subset of 3 411 objects with direct or indirect BH mass measurements, uncensored multi-frequency radio and hard X-ray flux data, along with redshift and/or distance values. We referred to this as the ETHER-FP sample, for which we calculated specific luminosities following Eq. (3.1.1). In Table 3.1.1 we presented the number of objects with measurements at each radio frequency within ETHER-FP, along with the minimum and maximum values for relevant parameters such as redshift, BH mass, radio luminosity, X-ray luminosity, radio-loudness, and Eddington ratio, whose distributions were illustrated in Figure 3.1.1 for the sample with 5 GHz flux data.

For each subsample, we applied a least-squares fitting algorithm to investigate the linear relationship between radio and hard X-ray luminosity, following the model presented in Eq (3.2.1). We obtained the slope and intercept of the regression that best fitted each dataset, and calculated relevant statistics such as the intrinsic scatter, adjusted coefficient of determination, Spearman rank order correlation coefficient and its associated p-value. These results were presented in Table 3.2.1, and visualized in Figure 3.2.1 for all the different radio frequencies, suggesting a strong correlation between $L_{\rm R}$ and $L_{\rm X}$.

The correlation proved to be statistically significant thanks to p-values lower than 0.05 (rejecting the null hypothesis), and $R^2_{\rm adj}$ values that indicated the model explained more than 67% of the variability in the $L_{\rm R}$ direction in the worst case scenario (1 GHz). Also, while the estimated parameters were different for each subsample, no clear trends were evident with increasing radio frequency.

We aimed to reduce the observed scatter in the radio/X-ray correlation by incorporating a SMBH mass component into the linear model, as described in Eq. (1.3.1). Determination of the best-fit linear correlation coefficients between $M_{\rm BH}$, $L_{\rm R}$, and $L_{\rm X}$, was achieved through two independent methods: an OLS multivariate linear regression with MC sampling, and a modified chi-square statistic numerical minimization approach. With these, we proved the existence of the FP at all ten radio frequencies considered, ranging from cm to sub-mm wavelengths, some of which have never been used before in similar studies.

While discrepancies between the correlation coefficients derived along the $M_{\rm BH}$ direction were observed in the FPs, both methods mostly agreed within a 1σ level of confidence. By rearranging the original FP relation into the expression shown in Eq. (3.3.5), we derived the best-fit parameters for a BH mass predictor function utilizing the OLS method. The best-fit parameters and model statistics for the radio luminosity FP can be found in Tables 3.3.1 to 3.3.2, and for the BH mass predictor function in Table 3.3.3. Visualizations of these correlations are shown in Figure 3.3.3 (2D) to 3.3.4 (3D) and Figure 3.3.5, respectively.

With these empirical FP results, we explored the physical interpretation of the FP via the implementation of accretion inflow and outflow SED models to fit the observed radio and X-ray photometry of each target.

The former consisted of a semianalytic thermal ADAF model, for which we first validated its predictions thanks to a good agreement with data from more detailed numerical simulations (Figure 4.1.1).

We aimed to assess the ability of the ADAF model to accurately reproduce observations by initially conducting SED fitting using a recursive bisection algorithm. This method allowed us to determine an optimal value for its previously unknown free parameter (Eddington ratio), that aligned the model with a hard X-ray measurements for a given BH mass. Due to the time consuming nature of this approach, we aimed to increase the speed of the process by the use of a library of 1 000 000 templates with combinations of $M_{\rm BH}$ and $l_{\rm Edd}$ across a wide range of values. Thanks to the vast speed increase, we were able to estimate errors via MC sampling.

We set up an efficient pipeline for predicting radio-wave fluxes from a SMBH mass and a hard X-ray luminosity via the ADAF SED model, which was then applied to each object in ETHER-FP. The comparisons between measured and simulated fluxes were shown in Figure 4.1.2 and 4.1.3, revealing systematic trends. We noted that while the magnitude range of the predicted luminosities was similar (as seen in Figure 3.3.3) to that of observed LLAGN, the distribution of mass and Eddington ratio between the two were not. Specifically, the ADAF SED models systematically underpredicted the observed mm and sub-mm luminosities for relatively low SMBH masses or relatively high Eddington ratios. These discrepancies were further reinforced by the observed disagreement between the observed and the theoretically expected FP correlation coefficients values when an ADAF was considered as the source of radio and X-ray emission. Therefore, flux predictions at radio frequencies from the thermal ADAF SED model are best considered as lower limits.

In light of this, we incorporated an additional component in the form of a phenomenological jet SED model to test if this would enhance the agreement between observations and predictions. This decision was motivated by the alignment of our FP correlation coefficients with expected values for scenarios dominated by jets, as observed across multiple subsamples. These comparisons are shown in Figure 4.2.1, 4.1.5, 4.1.4, and 4.2.2.

To achieve this, we first performed a parameter study of the jet SED model. Among the 14 free parameters of the jet model, the SMBH mass, jet outflow rate, power-law index of electrons, and the jet view angle were identified as having the most significant effect on the resulting spectrum (Figure 4.1.8). By iterating over different expected values of these, we created hundreds of jet SED templates and used these to develop an SED fitting algorithm which uses a combined accretion-jet model. This approach effectively improved the accuracy of the predictions for objects in the “Gold sample” of potentially resolvable SMBHs, as shown in Figure 4.1.9.

While the improved results encourage the use of a combined thermal ADAF+jet SED model, comparisons between results from these model and measured values for all sources in ETHER-FP would help reveal potential scenarios in which this approach fails to accurately reproduce the observations.

Our comprehensive analysis also permitted us to study the diversity in currently preferred radio emission mechanisms among distinct AGN types, galaxy morphologies, Eddington ratios, and radio-loudness values, as well as their evolution across cosmic time. The obtained parameters for the radio luminosity predictor functions revealed selection bias effects, since every subsample followed different FP relations. While this discarded the idea of a single universal relation, the correlation between L_{R}, L_{X}, and M_{BH} within a 3D plane remained.

Comparisons with theoretical FP parameter values, depicted in Figure 4.1.5, revealed that high redshift objects tend to be dominated by pure jet radiation, whereas nearby objects align more closely with the expected radio emission from a combined accretion-jet model. The variability in correlation coefficients across frequencies within individual subsamples suggested shifts in dominant emission mechanisms across the radio spectrum. Additionally, we found evidence for a potential redshift evolution of the dominant component, indicated by changes in best-fit parameters obtained when considering only low ($z \leq 0.05$) or high ($z > 0.05$) redshift sources within the same subsample.

The results encouraged the use of specific FP relations for accurate radio luminosity estimations, which are recommended over the radio/X-ray correlation due to their lower intrinsic scatter. However, the latter remains beneficial in the absence of precise SMBH mass estimates.

The intrinsic scatter of the mass predictor function was considerably reduced when derived separately for low and high redshift, or low and high Eddington ratio sources. Figure 3.3.5 and Figure 4.2.3 depicted how these groups appear to follow separate relations. These findings were consistent with previous studies and further validated the use of the FP as a BH mass estimator, particularly at larger distances.

We note that in the absence of measurements or estimations through more precise methods, the multiwavelength radio/X-ray correlations and FPs derived for the different samples, together with the ADAF and ADAF+jet SED fitting techniques developed for this study, can be used in conjunction with the automated query processing pipelines to significantly improve the completeness of ETHER in terms of radio-wave fluxes and BH mass estimates, which will ultimately help discard or identify potential sources to be considered for the “Gold sample” with current and/or future instruments. These relationships are also highly useful for other wide-ranging studies of SMBH (and AGN) evolution across cosmic time.

Future work should aim to refine the sample by correcting for factors not considered in this thesis, such as absorption, galaxy contamination, and Doppler boosting. This should help reduce the scatter in the radio/X-ray and FP relations, and reveal if some frequencies are more affected than others by these effects. Additionally, deriving best-fit FP parameters from several configurations of individual or combined ADAF, jet, corona, and/or torus SED models could help identify which components are responsible for the energetic output at distinct radio frequencies within the multiple subsamples considered in this study, as well as the proportion of individual contributions in combined origin scenarios.

Bibliography

Abdurro'uf, N., Accetta, K., Aerts, C., Silva Aguirre, V., Ahumada, R., Ajgaonkar, N., Filiz Ak, N., Alam, S., Allende Prieto, C., Almeida, A., et al. (2022). The seventeenth data release of the Sloan Digital Sky Surveys: Complete release of MaNGA, MaStar, and APOGEE-2 data. *The Astrophysical Journal. Supplement Series*, 259(2).

Abramowicz, M., Czerny, B., Lasota, J., and Szuszkiewicz, E. (1988). Slim accretion disks. *Astrophysical Journal, Part 1 (ISSN 0004-637X), vol. 332, Sept. 15, 1988, p. 646-658. Research supported by Observatoire de Paris and NASA.*, 332:646–658.

Aghanim, N., Akrami, Y., Ashdown, M., Aumont, J., Baccigalupi, C., Ballardini, M., Banday, A. J., Barreiro, R., Bartolo, N., Basak, S., et al. (2020). Planck 2018 results-VI. Cosmological parameters. *Astronomy & Astrophysics*, 641:A6.

Almeida, C. R. and Ricci, C. (2017). Nuclear obscuration in active galactic nuclei. *Nature Astronomy*, 1(10):679–689.

Astropy Collaboration, Price-Whelan, A. M., Lim, P. L., Earl, N., Starkman, N., Bradley, L., Shupe, D. L., Patil, A. A., Corrales, L., Brasseur, C. E., N"othe, M., Donath, A., Tollerud, E., Morris, B. M., Ginsburg, A., Vaher, E., Weaver, B. A., Tocknell, J., Jamieson, W., van Kerkwijk, M. H., Robitaille, T. P., Merry, B., Bachetti, M., G"unther, H. M., Aldcroft, T. L., Alvarado-Montes, J. A., Archibald, A. M., B'odi, A., Bapat, S., Barentsen, G., Baz'an, J., Biswas, M., Boquien, M., Burke, D. J., Cara, D., Cara, M., Conroy, K. E., Conseil, S., Craig, M. W., Cross, R. M., Cruz, K. L., D'Eugenio, F., Dencheva, N., Devillepoix, H. A. R., Dietrich, J. P., Eigenbrot, A. D., Erben, T., Ferreira, L., Foreman-Mackey, D., Fox, R., Freij, N., Garg, S., Geda, R., Glattly, L., Gondhalekar, Y., Gordon, K. D., Grant, D., Greenfield, P., Groener, A. M., Guest, S., Gurovich, S., Handberg, R., Hart, A., Hatfield-Dodds, Z., Homeier, D., Hosseinzadeh, G., Jenness, T., Jones, C. K., Joseph, P., Kalmbach, J. B., Karamehmetoglu, E., Kaluszy'nski, M., Kelley, M. S. P., Kern, N., Kerzendorf, W. E., Koch, E. W., Kulumani, S., Lee, A., Ly, C., Ma, Z., MacBride, C., Maljaars, J. M., Muna, D., Murphy, N. A., Norman, H., O'Steen, R., Oman, K. A., Pacifici, C., Pascual, S., Pascual-Granado, J., Patil, R. R., Perren, G. I., Pickering, T. E., Rastogi, T., Roulston, B. R., Ryan, D. F., Rykoff, E. S., Sabater, J., Sakurikar, P., Salgado, J., Sanghi, A., Saunders, N., Savchenko, V., Schwardt, L., Seifert-Eckert, M., Shih, A. Y., Jain, A. S., Shukla, G., Sick, J., Simpson, C., Singanamalla, S., Singer, L. P., Singhal, J., Sinha, M., SipHocz, B. M., Spitler, L. R., Stansby, D., Streicher, O., Sumak, J., Swinbank, J. D., Taranu, D. S., Tewary, N., Tremblay, G. R., Val-Borro, M. d., Van Kooten, S. J., Vasovi'c, Z., Verma, S., de Miranda Cardoso, J. V., Williams, P. K. G., Wilson, T. J., Winkel, B., Wood-Vasey, W. M., Xue, R., Yoachim, P., Zhang, C., Zonca, A., and Astropy Project Contributors (2022). The Astropy Project: Sustaining and Growing a Community-oriented Open-source Project and the Latest Major Release (v5.0) of the Core Package. *The Astrophyisical Journal*, 935(2):167.

Astropy Collaboration, Price-Whelan, A. M., Sipőcz, B. M., Günther, H. M., Lim, P. L., Crawford, S. M., Conseil, S., Shupe, D. L., Craig, M. W., Dencheva, N., Ginsburg, A., Vand erPlas, J. T., Bradley, L. D., Pérez-Suárez, D., de Val-Borro, M., Aldcroft, T. L., Cruz, K. L., Robitaille, T. P., Tollerud, E. J., Ardelean, C., Babej, T., Bach, Y. P., Bachetti, M., Bakanov, A. V., Bamford, S. P., Barentsen, G., Barmby, P., Baumbach, A., Berry, K. L., Biscani, F., Boquien, M., Bostroem, K. A., Bouma, L. G., Brammer, G. B., Bray, E. M., Breytenbach, H., Buddelmeijer, H., Burke, D. J., Calderone, G., Cano Rodríguez, J. L., Cara, M., Cardoso, J. V. M., Cheedella, S., Copin, Y., Corrales, L., Crichton, D., D'Avella, D., Deil, C., Depagne, É., Dietrich, J. P., Donath, A., Droettboom, M., Earl, N., Erben, T., Fabbro, S., Ferreira, L. A., Finethy, T., Fox, R. T., Garrison, L. H., Gibbons, S. L. J., Goldstein, D. A., Gommers, R., Greco, J. P., Greenfield, P., Groener, A. M., Grollier, F., Hagen, A., Hirst, P., Homeier, D., Horton, A. J., Hosseinzadeh, G., Hu, L., Hunkeler, J. S., Ivezić, Ž., Jain, A., Jenness, T., Kanarek, G., Kendrew, S., Kern, N. S., Kerzendorf, W. E., Khvalko, A., King, J., Kirkby, D., Kulkarni, A. M., Kumar, A., Lee, A., Lenz, D., Littlefair, S. P., Ma, Z., Macleod, D. M., Mastropietro, M., McCully, C., Montagnac, S., Morris, B. M., Mueller, M., Mumford, S. J., Muna, D., Murphy, N. A., Nelson, S., Nguyen, G. H., Ninan, J. P., Nöthe, M., Ogaz, S., Oh, S., Parejko, J. K., Parley, N., Pascual, S., Patil, R., Patil, A. A., Plunkett, A. L., Prochaska, J. X., Rastogi, T., Reddy Janga, V., Sabater, J., Sakurikar, P., Seifert, M., Sherbert, L. E., Sherwood-Taylor, H., Shih, A. Y., Sick, J., Silbiger, M. T., Singanamalla, S., Singer, L. P., Sladen, P. H., Sooley, K. A., Sornarajah, S., Streicher, O., Teuben, P., Thomas, S. W., Tremblay, G. R., Turner, J. E. H., Terrón, V., van Kerkwijk, M. H., de la Vega, A., Watkins, L. L., Weaver, B. A., Whitmore, J. B., Woillez, J., Zabalza, V., and Astropy Contributors (2018). The Astropy Project: Building an Open-science Project and Status of the v2.0 Core Package. *The Astrophyisical Journal*, 156(3):123.

Astropy Collaboration, Robitaille, T. P., Tollerud, E. J., Greenfield, P., Droettboom, M., Bray, E., Aldcroft, T., Davis, M., Ginsburg, A., Price-Whelan, A. M., Kerzendorf, W. E., Conley, A., Crighton, N., Barbary, K., Muna, D., Ferguson, H., Grollier, F., Parikh, M. M., Nair, P. H., Unther, H. M., Deil, C., Woillez, J., Conseil, S., Kramer, R., Turner, J. E. H., Singer, L., Fox, R., Weaver, B. A., Zabalza, V., Edwards, Z. I., Azalee Bostroem, K., Burke, D. J., Casey, A. R., Crawford, S. M., Dencheva, N., Ely, J., Jenness, T., Labrie, K., Lim, P. L., Pierfederici, F., Pontzen, A., Ptak, A., Refsdal, B., Servillat, M., and Streicher, O. (2013). Astropy: A community Python package for astronomy. *Astronomy & Astrophysics*, 558:A33.

Bandyopadhyay, B., Xie, F.-G., Nagar, N. M., Schleicher, D. R., Ramakrishnan, V., Arévalo, P., López, E., and Diaz, Y. (2019). Resolving accretion flows in nearby active galactic nuclei with the Event Horizon Telescope. *Monthly Notices of the Royal Astronomical Society*, 490(4):4606–4621.

Bariuan, L. G. C., Snios, B., Sobolewska, M., Siemiginowska, A., and Schwartz, D. A. (2022). The Fundamental Planes of black hole activity for radio-loud and radio-quiet quasars. *Monthly Notices of the Royal Astronomical Society*, 513(4):4673–4681.

Begelman, M. C. (1979). Can a spherically accreting black hole radiate very near the Eddington limit. *Monthly Notices of the Royal Astronomical Society*, 187(2):237–251.

Blackburn, L., Doeleman, S., Dexter, J., Gómez, J. L., Johnson, M. D., Palumbo, D. C., Weintroub, J., Bouman, K. L., Chael, A. A., Farah, J. R., et al. (2019). Studying black holes on horizon scales with VLBI ground arrays. *arXiv preprint arXiv:1909.01411*.

Blandford, R., Meier, D., and Readhead, A. (2019). Relativistic jets from active galactic nuclei. *Annual Review of Astronomy and Astrophysics*, 57:467–509.

Blandford, R. and Rees, M. (1974). A 'twin-exhaust'model for double radio sources. *Monthly Notices of the Royal Astronomical Society*, 169(3):395–415.

Blandford, R. D. and Payne, D. (1982). Hydromagnetic flows from accretion discs and the production of radio jets. *Monthly Notices of the Royal Astronomical Society*, 199(4):883–903.

Blanton, M. R., Bershady, M. A., Abolfathi, B., Albareti, F. D., Prieto, C. A., Almeida, A., Alonso-García, J., Anders, F., Anderson, S. F., Andrews, B., et al. (2017). Sloan digital sky survey IV: Mapping the Milky Way, nearby galaxies, and the distant universe. *The Astronomical Journal*, 154(1):28.

Blumenthal, G. R. and Gould, R. J. (1970). Bremsstrahlung, synchrotron radiation, and compton scattering of high-energy electrons traversing dilute gases. *Reviews of modern Physics*, 42(2):237.

Boccardi, B., Perucho, M., Casadio, C., Grandi, P., Macconi, D., Torresi, E., Pellegrini, S., Krichbaum, T., Kadler, M., Giovannini, G., et al. (2021). Jet collimation in NGC 315 and other nearby AGN. *Astronomy & Astrophysics*, 647:A67.

Bordovitsyn, V. A. et al. (1999). *Synchrotron radiation theory and its development: in memory of IM Ternov*, volume 5. World Scientific.

Burbidge, G. (1967). The quasi-stellar objects. *American Scientist*, 55(3):282–295.

Caswell, J. and Haynes, R. (1987). Southern H II regions-an extensive study of radio recombination line emission. *Astronomy and Astrophysics (ISSN 0004-6361), vol. 171, no. 1-2, Jan. 1987, p. 261-276.*, 171:261–276.

Celotti, A., Miller, J. C., and Sciama, D. W. (1999). Astrophysical evidence for the existence of black holes. *Classical and Quantum Gravity*, 16(12A):A3.

Collaboration, E. H. T. et al. (2019). First m87 event horizon telescope results. ii. array and instrumentation. *arXiv preprint arXiv:1906.11239*.

Conselice, C. J. (2006). The fundamental properties of galaxies and a new galaxy classification system. *Monthly Notices of the Royal Astronomical Society*, 373(4):1389–1408.

Corbel, S., Nowak, M., Fender, R. P., Tzioumis, A., and Markoff, S. (2003). Radio/X-ray correlation in the low/hard state of GX 339–4. *Astronomy & Astrophysics*, 400(3):1007–1012.

Davé, R., Oppenheimer, B. D., and Finlator, K. (2011). Galaxy evolution in cosmological simulations with outflows–I. Stellar masses and star formation rates. *Monthly Notices of the Royal Astronomical Society*, 415(1):11–31.

Dubner, G. and Giacani, E. (2015). Radio emission from supernova remnants. *The Astronomy and Astrophysics Review*, 23(1):3.

Evans, I. N., Primini, F. A., Glotfelty, K. J., Anderson, C. S., Bonaventura, N. R., Chen, J. C., Davis, J. E., Doe, S. M., Evans, J. D., Fabbiano, G., et al. (2010). The Chandra source catalog. *The Astrophysical Journal Supplement Series*, 189(1):37.

Event Horizon Telescope Collaboration et al. (2019). First M87 event horizon telescope results. I. The shadow of the supermassive black hole. *The Astrophysical Journal*, 875(1):L1.

Event Horizon Telescope Collaboration et al. (2022). First Sagittarius A* Event Horizon Telescope results. I. The shadow of the supermassive black hole in the center of the Milky Way. *The Astrophysical Journal Letters*, 930(2):L12.

Falcke, H., Körding, E., and Markoff, S. (2004). A scheme to unify low-power accreting black holes-Jet-dominated accretion flows and the radio/X-ray correlation. *Astronomy & Astrophysics*, 414(3):895–903.

Fanaroff, B. L. and Riley, J. M. (1974). The morphology of extragalactic radio sources of high and low luminosity. *Monthly Notices of the Royal Astronomical Society*, 167(1):31P–36P.

Fasano, G. and Vio, R. (1988). Fitting a straight line with errors on both coordinates. *Bulletin d'Information du Centre de Donnees Stellaires, No. 35, P. 191, 1988*, 35:191.

Finkelstein, D. (1958). Past-future asymmetry of the gravitational field of a point particle. *Physical Review*, 110(4):965.

Fischer, T. C., Secrest, N. J., Johnson, M. C., Dorland, B. N., Cigan, P. J., Fernandez, L. C., Hunt, L. R., Koss, M., Schmitt, H. R., and Zacharias, N. (2021). Fundamental Reference AGN Monitoring Experiment (FRAMEx). I. Jumping Out of the Plane with the VLBA. *The Astrophysical Journal*, 906(2):88.

Gallo, E., Fender, R. P., and Pooley, G. (2003). A universal radio–X-ray correlation in low/hard state black hole binaries. *Monthly Notices of the Royal Astronomical Society*, 344(1):60–72.

Ginsburg, A., Sipőcz, B. M., Brasseur, C., Cowperthwaite, P. S., Craig, M. W., Deil, C., Groener, A. M., Guillochon, J., Guzman, G., Liedtke, S., et al. (2019). Astroquery: an astronomical web-querying package in Python. *The Astronomical Journal*, 157(3):98.

Gu, W.-M., Xue, L., Liu, T., and Lu, J.-F. (2009). Advection-Dominated Accretion Disks: Geometrically Slim or Thick? *Publications of the Astronomical Society of Japan*, 61(6):1313–1318.

Gültekin, K., Cackett, E. M., King, A. L., Miller, J. M., and Pinkney, J. (2014). Low-mass AGNs and their relation to the fundamental plane of black hole accretion. *The Astrophysical Journal Letters*, 788(2):L22.

Gültekin, K., Cackett, E. M., Miller, J. M., Di Matteo, T., Markoff, S., and Richstone, D. O. (2009). The fundamental plane of accretion onto black holes with dynamical masses. *The Astrophysical Journal*, 706(1):404.

Gültekin, K., King, A. L., Cackett, E. M., Nyland, K., Miller, J. M., Di Matteo, T., Markoff, S., and Rupen, M. P. (2019). The fundamental plane of black hole accretion and its use as a black hole-mass estimator. *The Astrophysical Journal*, 871(1):80.

Gültekin, K., Nyland, K., Gray, N., Fehmer, G., Huang, T., Sparkman, M., Reines, A. E., Greene, J. E., Cackett, E. M., and Baldassare, V. (2022). Intermediate-mass black holes and the Fundamental Plane of black hole accretion. *Monthly Notices of the Royal Astronomical Society*, 516(4):6123–6131.

Hannikainen, D., Hunstead, R., Campbell-Wilson, D., and Sood, R. (1998). MOST radio monitoring of GX 339-4. *arXiv preprint astro-ph/9805332*.

Heckman, T. (1980). An optical and radio survey of the nuclei of bright galaxies-Activity in normal galactic nuclei. *Astronomy and Astrophysics, vol. 87, no. 1-2, July 1980, p. 152-164. Research supported by the University of Washington.*, 87:152–164.

Heinz, S. and Sunyaev, R. (2003). The non-linear dependence of flux on black hole mass and accretion rate in core-dominated jets. *Monthly Notices of the Royal Astronomical Society*, 343(3):L59–L64.

Hernández-Yévenes, J., Nagar, N., Arratia, V., and Jarrett, T. H. (2024). WISE2MBH: A scaling-based algorithm for probing supermassive black hole masses through WISE catalogs. *arXiv preprint arXiv:2405.18336*.

Hernández-Yévenes, J., Nagar, N., Arratia, V., and Jarrett, T. H. (2024). Wise2mbh: A scaling-based algorithm for probing supermassive black hole masses through wise catalogs.

Hickox, R. C. and Alexander, D. M. (2018). Obscured active galactic nuclei. *Annual Review of Astronomy and Astrophysics*, 56:625–671.

Ho, L. C. (2008). Nuclear activity in nearby galaxies. *Annu. Rev. Astron. Astrophys.*, 46:475–539.

Ho, L. C., Filippenko, A. V., and Sargent, W. L. (1997). A Search for "Dwarf"Seyfert Nuclei. III. Spectroscopic Parameters and Properties of the Host Galaxies. *The Astrophysical Journal Supplement Series*, 112(2):315.

Hughes, S. A. (2005). Trust but verify: The case for astrophysical black holes. *arXiv preprint hep-ph/0511217*.

Ichimaru, S. (1977). Bimodal behavior of accretion disks-Theory and application to Cygnus X-1 transitions. *Astrophysical Journal, Part 1, vol. 214, June 15, 1977, p. 840-855. Research supported by the Japan Society for the Promotion of Science*, 214:840–855.

Johnson, M. D., Akiyama, K., Blackburn, L., Bouman, K. L., Broderick, A. E., Cardoso, V., Fender, R. P., Fromm, C. M., Galison, P., Gómez, J. L., et al. (2023). Key Science Goals for the Next-Generation Event Horizon Telescope. *Galaxies*, 11(3):61.

Kawamuro, T., Ricci, C., Imanishi, M., Mushotzky, R. F., Izumi, T., Ricci, F., Bauer, F. E., Koss, M. J., Trakhtenbrot, B., Ichikawa, K., et al. (2022). BASS XXXII: Studying the Nuclear Millimeter-wave Continuum Emission of AGNs with ALMA at Scales < 100–200 pc. *The Astrophysical Journal*, 938(1):87.

Körding, E., Falcke, H., and Corbel, S. (2006). Refining the fundamental plane of accreting black holes. *Astronomy & Astrophysics*, 456(2):439–450.

Liu, F. and Zhang, Y. (2002). A new list of extra-galactic radio jets. *Astronomy & Astrophysics*, 381(3):757–760.

Loeb, A. and Rasio, F. A. (1994). Collapse of primordial gas clouds and the formation of quasar black holes. *arXiv preprint astro-ph/9401026*.

Lusso, E., Comastri, A., Vignali, C., Zamorani, G., Treister, E., Sanders, D., Bolzonella, M., Bongiorno, A., Brusa, M., Civano, F., et al. (2011). The bolometric output and host-galaxy properties of obscured AGN in the XMM-COSMOS survey. *Astronomy & Astrophysics*, 534:A110.

Mahadevan, R. (1997). Scaling laws for advection-dominated flows: applications to low-luminosity galactic nuclei. *The Astrophysical Journal*, 477(2):585.

Maiolino, R. and Rieke, G. (1995). Low-luminosity and obscured seyfert nuclei in nearby galaxies. *Astrophysical Journal v. 454, p. 95*, 454:95.

Maoz, D. (2007). Low-luminosity active galactic nuclei: are they UV faint and radio loud? *Monthly Notices of the Royal Astronomical Society*, 377(4):1696–1710.

Mayer, L. and Bonoli, S. (2018). The route to massive black hole formation via merger-driven direct collapse: a review. *Reports on Progress in Physics*, 82(1):016901.

Meier, D. L. (2003). The theory and simulation of relativistic jet formation: towards a unified model for micro-and macroquasars. *New Astronomy Reviews*, 47(6-7):667–672.

Merloni, A., Heinz, S., and Di Matteo, T. (2003). A Fundamental Plane of black hole activity. *Monthly Notices of the Royal Astronomical Society*, 345(4):1057–1076.

Merloni, A., Lamer, G., Liu, T., Ramos-Ceja, M., Brunner, H., Bulbul, E., Dennerl, K., Doroshenko, V., Freyberg, M., Friedrich, S., et al. (2024). The SRG/eROSITA all-sky survey-First X-ray catalogues and data release of the western Galactic hemisphere. *Astronomy & Astrophysics*, 682:A34.

Nagar, N. M., Falcke, H., and Wilson, A. S. (2005). Radio sources in low-luminosity active galactic nuclei-IV. Radio luminosity function, importance of jet power, and radio properties of the complete Palomar sample. *Astronomy & Astrophysics*, 435(2):521–543.

Narayan, R. (1996). Advection-dominated models of luminous accreting black holes. *arXiv preprint astro-ph/9510028*.

Narayan, R. and Yi, I. (1994). Advection-dominated accretion: A self-similar solution. *arXiv preprint astro-ph/9403052*.

Narayan, R. and Yi, I. (1995). Advection-dominated accretion: Underfed black holes and neutron stars. *arXiv preprint astro-ph/9411059*.

Nemmen, R. S., Storchi-Bergmann, T., and Eracleous, M. (2014). Spectral models for low-luminosity active galactic nuclei in LINERs: the role of advection-dominated accretion and jets. *Monthly Notices of the Royal Astronomical Society*, 438(4):2804–2827.

Netzer, H. (2015). Revisiting the unified model of active galactic nuclei. *Annual Review of Astronomy and Astrophysics*, 53:365–408.

Noble, S. C., Krolik, J. H., Schnittman, J. D., and Hawley, J. F. (2011). Radiative efficiency and thermal spectrum of accretion onto Schwarzschild black holes. *The Astrophysical Journal*, 743(2):115.

Padovani, P., Alexander, D., Assef, R., De Marco, B., Giommi, P., Hickox, R., Richards, G., Smolčić, V., Hatziminaoglou, E., Mainieri, V., et al. (2017). Active galactic nuclei: what's in a name? *The Astronomy and Astrophysics Review*, 25:1–91.

Page, M., Symeonidis, M., Vieira, J., Altieri, B., Amblard, A., Arumugam, V., Aussel, H., Babbedge, T., Blain, A., Bock, J., et al. (2012). The suppression of star formation by powerful active galactic nuclei. *Nature*, 485(7397):213–216.

Panessa, F., Barcons, X., Bassani, L., Cappi, M., Carrera, F. J., Ho, L., and Pellegrini, S. (2007). The X-ray and radio connection in low-luminosity active nuclei. *Astronomy & Astrophysics*, 467(2):519–527.

Pesce, D. W., Palumbo, D. C., Narayan, R., Blackburn, L., Doeleman, S. S., Johnson, M. D., Ma, C.-P., Nagar, N. M., Natarajan, P., and Ricarte, A. (2021). Toward determining the number of observable supermassive black hole shadows. *The Astrophysical Journal*, 923(2):260.

Plotkin, R. M., Markoff, S., Kelly, B. C., Körding, E., and Anderson, S. F. (2012). Using the Fundamental Plane of black hole activity to distinguish X-ray processes from weakly accreting black holes. *Monthly Notices of the Royal Astronomical Society*, 419(1):267–286.

Predehl, P., Andritschke, R., Arefiev, V., Babyshkin, V., Batanov, O., Becker, W., Böhringer, H., Bogomolov, A., Boller, T., Borm, K., et al. (2021). The eROSITA X-ray telescope on SRG. *Astronomy & Astrophysics*, 647:A1.

Ramakrishnan, V., Nagar, N., Arratia, V., Hernández-Yévenes, J., Pesce, D. W., Nair, D. G., Bandyopadhyay, B., Medina-Porcile, C., Krichbaum, T. P., Doeleman, S., et al. (2023). Event Horizon and Environs (ETHER): A Curated Database for EHT and ngEHT Targets and Science. *Galaxies*, 11(1):15.

Raouf, M., Silk, J., Shabala, S. S., Mamon, G. A., Croton, D. J., Khosroshahi, H. G., and Beckmann, R. S. (2019). Feedback by supermassive black holes in galaxy evolution: impacts of accretion and outflows on the star formation rate. *Monthly Notices of the Royal Astronomical Society*, 486(2):1509–1522.

Raymond, A. W., Palumbo, D., Paine, S. N., Blackburn, L., Rosado, R. C., Doeleman, S. S., Farah, J. R., Johnson, M. D., Roelofs, F., Tilanus, R. P., et al. (2021). Evaluation of new submillimeter vlbi sites for the event horizon telescope. *The Astrophysical Journal Supplement Series*, 253(1):5.

Ricci, C., Chang, C.-S., Kawamuro, T., Privon, G. C., Mushotzky, R., Trakhtenbrot, B., Laor, A., Koss, M. J., Smith, K. L., Gupta, K. K., et al. (2023). A Tight Correlation between Millimeter and X-Ray Emission in Accreting Massive Black Holes from< 100 mas Resolution ALMA Observations. *The Astrophysical Journal Letters*, 952(2):L28.

Rosas-Guevara, Y., Bower, R. G., Schaye, J., McAlpine, S., Dalla Vecchia, C., Frenk, C. S., Schaller, M., and Theuns, T. (2016). Supermassive black holes in the EAGLE Universe. Revealing the observables of their growth. *Monthly Notices of the Royal Astronomical Society*, 462(1):190–205.

Ruffa, I., Davis, T. A., Elford, J. S., Bureau, M., Cappellari, M., Gensior, J., Haggard, D., Iguchi, S., Lelli, F., Liang, F.-H., et al. (2024). A fundamental plane of black hole accretion at millimetre wavelengths. *Monthly Notices of the Royal Astronomical Society: Letters*, 528(1):L76–L82.

Rybicki, G. B. and Lightman, A. P. (1991). *Radiative processes in astrophysics*. John Wiley & Sons.

Saglia, R., Opitsch, M., Erwin, P., Thomas, J., Beifiori, A., Fabricius, M., Mazzalay, X., Nowak, N., Rusli, S., and Bender, R. (2016). The SINFONI black hole survey: the black hole fundamental plane revisited and the paths of (co) evolution of supermassive black holes and bulges. *The Astrophysical Journal*, 818(1):47.

Saikia, P., Körding, E., and Dibi, S. (2018). 1.4 GHz on the Fundamental Plane of black hole activity. *Monthly Notices of the Royal Astronomical Society*, 477(2):2119–2127.

Sauty, C., Tsinganos, K., and Trussoni, E. (2002). Jet formation and collimation. *Relativistic Flows in Astrophysics*, pages 41–70.

Scoville, N. Z. (2012). Evolution of star formation and gas. *arXiv preprint arXiv:1210.6990*.

Shakura, N. I. and Sunyaev, R. A. (1973). Black holes in binary systems. Observational appearance. *Astronomy and Astrophysics, Vol. 24, p. 337-355*, 24:337–355.

Shields, J. C. (1992). Normal O stars in dense media generate LINERs. *Astrophysical Journal, Part 2-Letters (ISSN 0004-637X), vol. 399, no. 1, p. L27-L30.*, 399:L27–L30.

Spada, M., Ghisellini, G., Lazzati, D., and Celotti, A. (2001). Internal shocks in the jets of radio-loud quasars. *Monthly Notices of the Royal Astronomical Society*, 325(4):1559–1570.

Terlevich, R. and Melnick, J. (1985). Warmers: the missing link between Starburst and Seyfert galaxies. *Monthly Notices of the Royal Astronomical Society*, 213(4):841–856.

Ulrich, M.-H., Maraschi, L., and Urry, C. M. (1997). Variability of active galactic nuclei. *Annual Review of Astronomy and Astrophysics*, 35(1):445–502.

Urry, C. M. and Padovani, P. (1995). Unified schemes for radio-loud active galactic nuclei. *Publications of the Astronomical Society of the Pacific*, 107(715):803.

van Velzen, S., Falcke, H., Schellart, P., Nierstenhöfer, N., and Kampert, K.-H. (2012). Radio galaxies of the local universe-all-sky catalog, luminosity functions, and clustering. *Astronomy & Astrophysics*, 544:A18.

Vattakunnel, S., Tozzi, P., Matteucci, F., Padovani, P., Miller, N., Bonzini, M., Mainieri, V., Paolillo, M., Vincoletto, L., Brandt, W., et al. (2012). The radio–X-ray relation as a star formation indicator: results from the Very Large Array–Extended Chandra Deep Field-South. *Monthly Notices of the Royal Astronomical Society*, 420(3):2190–2208.

Virtanen, P., Gommers, R., Oliphant, T. E., Haberland, M., Reddy, T., Cournapeau, D., Burovski, E., Peterson, P., Weckesser, W., Bright, J., van der Walt, S. J., Brett, M., Wilson, J., Millman, K. J., Mayorov, N., Nelson, A. R. J., Jones, E., Kern, R., Larson, E., Carey, C. J., Polat, İ., Feng, Y., Moore, E. W., VanderPlas, J., Laxalde, D., Perktold, J., Cimrman, R., Henriksen, I., Quintero, E. A., Harris, C. R., Archibald, A. M., Ribeiro, A. H., Pedregosa, F., van Mulbregt, P., and SciPy 1.0 Contributors (2020). SciPy 1.0: Fundamental Algorithms for Scientific Computing in Python. *Nature Methods*, 17:261–272.

Volonteri, M. (2010). Formation of supermassive black holes. *The Astronomy and Astrophysics Review*, 18:279–315.

Wang, R., Wu, X.-B., and Kong, M.-Z. (2006). The black hole fundamental plane from a uniform sample of radio and X-ray-emitting broad-line AGNs. *The Astrophysical Journal*, 645(2):890.

Watarai, K.-y., Fukue, J., Takeuchi, M., and Mineshige, S. (2000). Galactic black-hole candidates shining at the Eddington luminosity. *Publications of the Astronomical Society of Japan*, 52(1):133–141.

Wenger, M., Ochsenbein, F., Egret, D., Dubois, P., Bonnarel, F., Borde, S., Genova, F., Jasniewicz, G., Laloë, S., Lesteven, S., et al. (2000). The SIMBAD astronomical database-The CDS reference database for astronomical objects. *Astronomy and Astrophysics Supplement Series*, 143(1):9–22.

White, R. L., Becker, R. H., Helfand, D. J., and Gregg, M. D. (1997). A catalog of 1.4 GHz radio sources from the FIRST survey. *The Astrophysical Journal*, 475(2):479.

Wilson, A. S. and Colbert, E. J. (1994). The difference between radio-loud and radio-quiet active galaxies. *arXiv preprint astro-ph/9408005*.

Wong, O., Koss, M., Schawinski, K., Kapińska, A., Lamperti, I., Oh, K., Ricci, C., and Berney, S. (2016). Determining the radio AGN contribution to the radio-FIR correlation using the black hole fundamental plane relation. *arXiv preprint arXiv:1604.05981*.

Wright, E. L., Eisenhardt, P. R., Mainzer, A. K., Ressler, M. E., Cutri, R. M., Jarrett, T., Kirkpatrick, J. D., Padgett, D., McMillan, R. S., Skrutskie, M., et al. (2010). The Wide-field Infrared Survey Explorer (WISE): mission description and initial on-orbit performance. *The Astronomical Journal*, 140(6):1868.

Yi, I. and Boughn, S. P. (1998). Radio/X-Ray Luminosity Relation for Advection-dominated Accretion: Implications for Emission-Line Galaxies and the X-Ray Background. *The Astrophysical Journal*, 499(1):198.

Yuan, F. and Cui, W. (2005). Radio-X-ray correlation and the “quiescent state” of black hole sources. *The Astrophysical Journal*, 629(1):408.

Yuan, F., Cui, W., and Narayan, R. (2005). An accretion-jet model for black hole binaries: Interpreting the spectral and timing features of XTE J1118+ 480. *The Astrophysical Journal*, 620(2):905.

Yuan, F. and Narayan, R. (2014). Hot accretion flows around black holes. *Annual Review of Astronomy and Astrophysics*, 52:529–588.

Yuan, F., Yu, Z., and Ho, L. C. (2009). Revisiting the “fundamental plane” of black hole activity at extremely low luminosities. *The Astrophysical Journal*, 703(1):1034.

Appendix A

Using SDSS velocity dispersion data to estimate SMBH masses

Making use of the `astroquery.sdss` and `astropy` Python packages we cross matched the coordinates in ETHER to the SDSS-IV DR16 database using a 10 arcsec match radius for sources at $z < 0.05$ and a 3 arcsec radius for farther away AGN. The returned data tables contain information on the classification and sub classification of the objects, positions, redshift and corresponding error, together with a stellar velocity dispersion value (σ) and error ($\sigma_{\rm err}$), we also added an additional column to keep track of the position offset between the input coordinates and the match, useful when deciding which entry to keep during post-processing. Due to the possibility of multiple matches to a single source, we make sure to remove all the sources explicitly classified as stars, and retain the match that has both redshift and velocity dispersion data, or at least one of the two, and from that pick the lowest separation. Using Saglia et al. (2016) $M_{\rm BH} - \sigma$ linear relation:

$$\log M_{\rm BH} = (5.24 \pm 0.27)\log\sigma + (-3.77 \pm 0.63), \tag{A0.1}$$

we were able to estimate $M_{\rm BH}$ in galaxies with SDSS σ value that had reasonable error ($\sigma_{\rm err} < 100$). Figure A0.1 shows that for very low redshift ($z < 0.02$) sources, the $M_{\rm BH} - \sigma$ relation of Saglia et al. (2016) tends to greatly underestimate the mass of the central BH, specially for sources with very low σ values, therefore one should be cautious when employing this relation for sources in the nearby Universe, reason why we do not prioritize the inclusion of SDSS $M_{\rm BH} - \sigma$ derived masses for these particular cases unless there is nothing else available, trying to maintaining just the upper limit estimate to reduce the deviation in this situation.

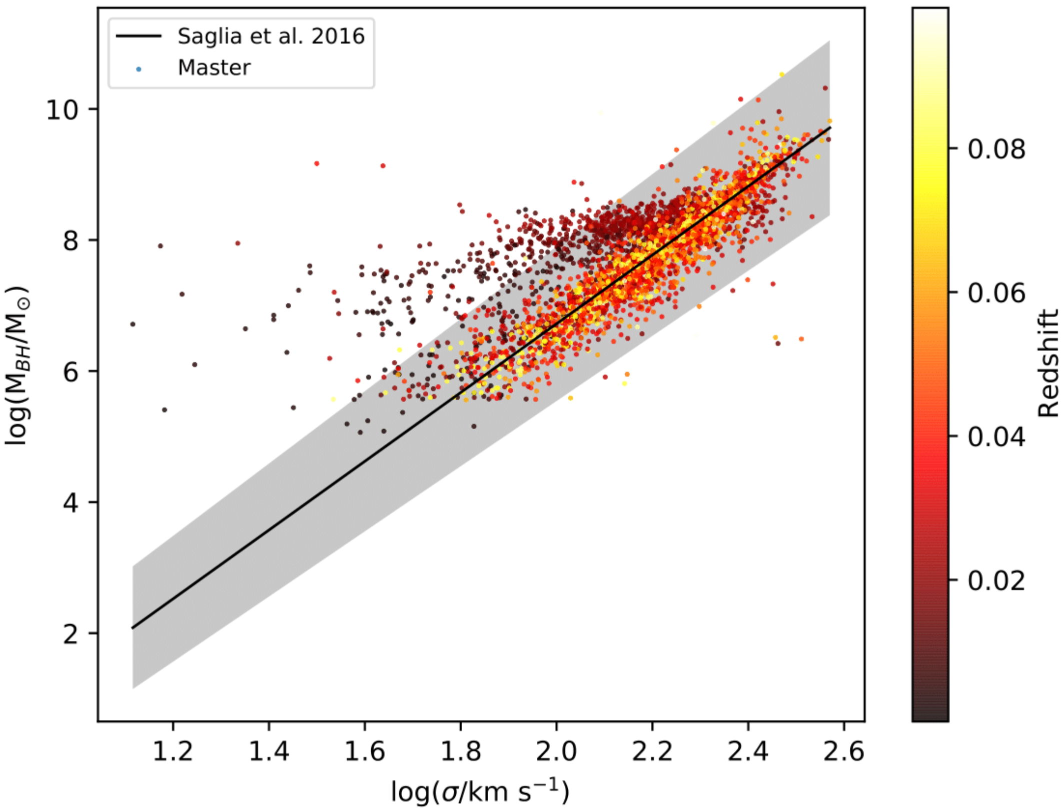

Figure A0.1: BH mass against SDSS velocity dispersion for a sample of $\sim 3\,800$ sources in ETHER. Solid black line and grey area correspond to Saglia et al. (2016) $M_{\rm BH} - \sigma$ relation expected values and error derived from Eq. (A0.1) respectively. ETHER data is visualized as colored circles mapped to a redshift color bar.